Title
MECHANICS OF ORIGAMI-BASED SHEET METAL BENDING

Author
Nuryar, Muhammad-Ali Ablat

Publication Date
2020

UNIVERSITY OF CALIFORNIA, MERCED

MECHANICS OF ORIGAMI-BASED SHEET METAL BENDING

by

Muhammad-Ali Ablat Nuryar

A thesis submitted in partial satisfaction of the
requirements for the degree of
Doctor of Philosophy

in

Mechanical Engineering

Committee in charge:
Professor Jian-Qiao Sun, Chair
Professor Ala Qattawi
Professor Sachin Goyal
Professor Valerie Leppert

The thesis of Muhammad-Ali Ablat Nuryar is approved:

Professor Jian-Qiao Sun, Chair	Date
Professor Ala Qattawi	Date
Professor Sachin Goyal	Date
Professor Valerie Leppert	Date

University of California, Merced

To my parents Ablat Yusup, Aygul Urayim,
siblings Mirsali, Nejibulla, Nesirulla,
and wife Anargul

ACKNOWLEDGEMENTS

First and foremost, I would like to acknowledge the support from my advisors, Professor Ala Qattawi and Professor Jian-Qiao Sun.

I would like to express my deep gratitude to Professor Ala Qattawi for everything she has done to make my Ph.D. journey successful and fruitful. She has been very supportive in funding, and thoughtful in guiding my research. She offered numerous opportunities to present my findings in scientific conferences, explore new ideas, expand my network, initiate collaboration. This dissertation would not have been possible without her unwavering support, mentoring, patience, and motivation.

I am immensely thankful to Professor Jian-Qiao Sun for his instrumental role for me to be able to seamlessly transition in crucial phases of my Ph.D. journey. He has been extremely helpful and supportive to ensure I am receiving the necessary resources to carry out my research successfully.

A special thanks goes to my thesis committee members, Professor Sachin Goyal and Professor Valerie Leppert, for their insightful comments to improve my work.

I would like to thank my research collaborators Prof. Masakazu Soshi and his student Curtis Yau from Advanced Research for Manufacturing Systems (ARMS) lab at the University of California Davis for their willingness to offer me a collaboration opportunity in my experimental work.

I also would like to thank my lab-mates, Ala'aldin Alafaghani and Md Shah Jaman, who have been offering help with insightful discussions, proofreading, testing, best of suggestions and tips.

I am deeply grateful to my parents, Ablat Yusup and Aygul Urayim, siblings Mirsali, Nejibulla, Nesirulla for their unconditional love and trust.

Last but not least, I would like to extend my sincere gratitude to my lovely wife, Anargul, for her understanding, patience, and love. She has been a best friend and supporter for years. This work would not have been possible without her.

CURRICULUM VITAE

Education

Ph. D in Mechanical Engineering, University of California, Merced, 2020

Publications

Muhammad-Ali Ablat Nuryar, Ala Qattawi, and Jian-Qiao Sun, "Investigation of failure by fracture in origami-based sheet metal bending", *International Journal of Mechanical Sciences*, 2020. (manuscript in press).

Muhammad-Ali Ablat Nuryar, Ala Qattawi, Ala'aldin Alafaghani, Jian-Qiao Sun, and Fatemeh K. Zavareh, "Experimental evaluation of tension and shear responses of material discontinuities in origami-based sheet metal bending," *Journal of Manufacturing and Material Processing*, 2020. (manuscript in press).

Muhammad-Ali Ablat Nuryar, Ala Qattawi, Md Shah Jaman, Curtis Yau, Ala'aldin Alafaghani, Masakazu Soshi, and Jian-Qiao Sun, "An experimental and analytical model for force prediction in sheet metal forming process using perforated sheet and origami principles", *Procedia Manufacturing*, 48:407–418,2020.

Ala'aldin Alafaghani, Ala Qattawi, Md Shah Jaman, and **Muhammad-Ali Ablat Nuryar**, "Microstructure and mechanical properties of direct metal lasersintered 15-5ph steel with different solution annealing heat treatments", *The International Journal of Advanced Manufacturing Technology*, 105(7), December 2019.

Muhammad-Ali Ablat Nuryar, and Ala Qattawi, "Investigating the design and process parameters of folded perforated sheet metal", *The International Journal of Advanced Manufacturing Technology*, 102(1), May 2019.

Ala Qattawi, Ala'aldin Alafaghani, **Muhammad-Ali Ablat Nuryar**, and Md Shah Jaman, "A model curriculum for a multidisciplinary engineering capstone design course: a design-based approach", *International Journal of Mechanical Engineering Education*, 2019.

Muhammad-Ali Ablat Nuryar, and Ala Qattawi, “Finite element analysis of origami-based sheet metal folding process”, *Journal of Engineering Materials and Technology*, 140:031008, 3, 2018.

Ala’aldin Alafaghani, Ala Qattawi, and **Muhammad-Ali Ablat Nuryar**, “Design consideration for additive manufacturing: fused deposition modeling”, *Open Journal of Applied Sciences*, 7, 2017.

Muhammad-Ali Ablat Nuryar, Ala Qattawi, “Numerical simulation of sheet metal forming: a review”, *The International Journal of Advanced Manufacturing Technology*, 89(1):1235–1250, March 2017.

Muhammad-Ali Ablat Nuryar, Ala Qattawi, “Finite element analysis of origami-based sheet metal folding process”, *Volume 2: Advanced Manufacturing, Phoenix, USA. ASME 2016 International Mechanical Engineering Congress & Exposition (IMECE)*, November 2016.

TABLE OF CONTENTS

Chapter

LIST OF FIGURES

LIST OF TABLES

ABSTRACT

The increased use of sheet metal products in automotive, construction, and aerospace industries leads to investigate more precise, economic and sustainable sheet metal bending techniques. The conventional sheet metal bending processes often require costly shape-dedicated die/mold set and special high tonnage machinery. Origami-based sheet metal (OSM) bending can overcome the challenge and achieve precision, simplicity, and minimum machinery/equipment requirement by implementing origami principle on sheet metal. To date, there are very limited attempts to understand and explore OSM bending in manufacturing research community. The bottleneck that hinders OSM bending from wide usage is due to lack of understanding of the OSM bending mechanics in metal sheets. The dissertation focus on expanding the knowledge about OSM bending from mechanics point of view.

This work relies on computational, experimental, analytical approaches to present investigations on fundamentals of OSM bending mechanics. The focus is the correlation between manufacturing parameters of OSM bending and the resulting bending process mechanics. Specifically, I introduced OSM into a conventional bending process, wiping die bending, to investigate effect of OSM in terms of required bending force, bending accuracy, and deformation. Then, OSM bending is conceptualized and parameters associated to both OSM bending process and OSM design process are determined. A general guide has been made as to selection of these parameters. In the next step, the required bending force for OSM bending is formulated with experimental and analytical approach. It was discovered that the topology of the material discontinuity has a unique shape factor that impacts magnitude of the OSM bending force. Further, the deformation behavior of OSM under tension and shear loading are investigated. Finally, fracture prediction in OSM bending is explored considering the effect of material discontinuity (MD) scale and sheet thickness. The result indicated that the higher the scale is, the less likely a fracture happens. The higher the thickness of the sheet is, the more likely a fracture occurs. The possibility of fracture is also associated with topology of the MDs.

Chapter 1

INTRODUCTION

Origami – meaning paper folding in Japanese, has been the inspiration for many in science and engineering. Examples for application of origami concept range from kinematics [1], structure [2–4], metamaterials [5,6], mathematics [7–9], energy [10], biomedical devices [11], construction [12,13]. Likewise, the origami-based sheet metal (OSM) bending is an extension of the origami concept onto metal sheets [14]. It brings forward an alternative bending method for sheet metal. Growing research and application of OSM bending in structures [4,15–17], vehicle Body-in-White [18], and potential application in automotive, aerospace, construction industries motivate deeper understanding mechanics of OSM bending process. The core idea of OSM bending is the construction of three-dimensional (3-D) structures out of a flat two-dimensional (2-D) metal sheet by a sequence of folding or bending operations. The bending is achieved with the aid of material discontinuities (MD) located at the predetermined bending line on the metal sheet. Figure 1.1 [19, 20] shows possible MDs.

As a common bending process, sheet metal bending can be achieved by wiping die bending (L bending), air bending (V bending), circular bending, roll bending and U bending. Unlike these conventional bending methods, OSM bending is a dieless bending process, in which bending is achieved with the configuration shown in 1.2. A blank sheet is held between a support and a blank holder. The support is fixed and a force in downward (negative Y) direction is applied on the blank holder to hold the blank sheet firmly. Bending line is offset from the edge of the blank holder a distance, s. Bending takes place with the downward motion of the punch. The motion of the punch is determined by the geometric configuration of the setup, sheet thickness, and bending angle. The advantages of OSM bending with this configuration is that it eliminates heavy machinery, costly shape dedicated die/mold set and its maintenance from bending process, which is significant economic and productivity gain in manufacturing process. However, one of the challenges to widely utilize OSM bending in production scale like other conventional bending techniques is unknown mechanics such as feasibility, deformation, accuracy and failure mechanism. This under-studied area hinders its wide usage due to research in this area being in relatively early stages. As an alternative sheet metal bending technique, mechanics of OSM bending is an open research domain where bending mechanism,

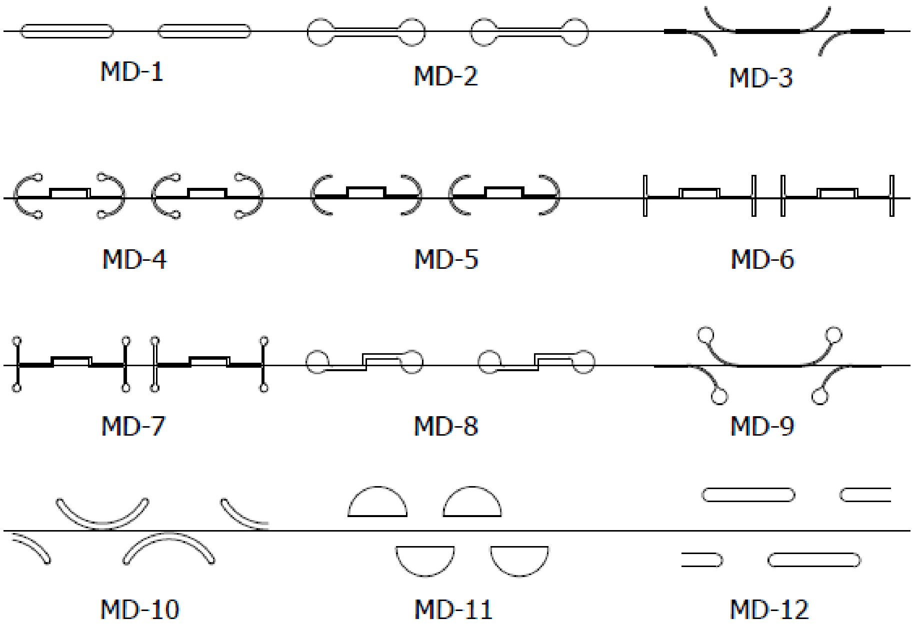

Figure 1.1: Possible material discontinuities (MDs)

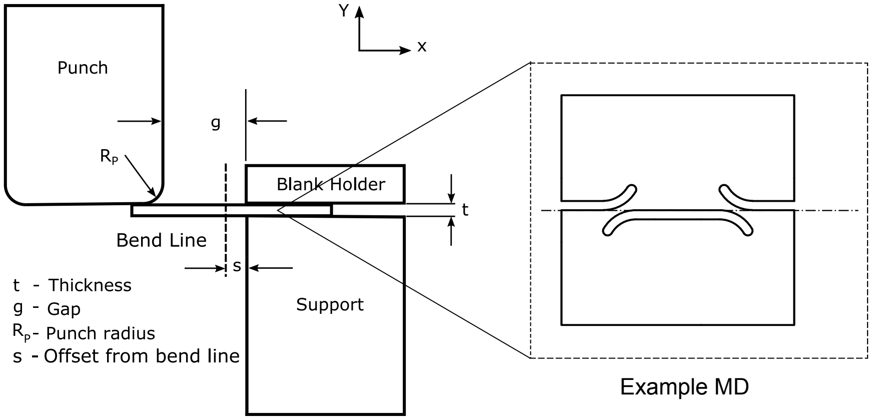

Figure 1.2: OSM bending configuration

feasibility, parameters influencing the bending process, accuracy, deformation have not been investigated. The dissertation, therefore, investigates on mechanics of less explored bending technique - i.e., OSM bending technique. This work involves process (concept) design, finite element analysis (FEA) , experimental testing, and analytical modeling.

The research on OSM bending is at the intersection of bending in sheet metal bending, rigid origami, and perforated sheet metal. Thus, in the following, a review is presented from each of the three field mentioned above.

1.1 Literature review

1.1.1 Sheet metal bending method perspective

Sheet metal forming is a common manufacturing process. A study by the European Aluminum Association [21] shows 55% of weight in Audi A2 vehicle body is made from sheet metal components. Further, sheet metal bending is one of the most common forming processes [22]. Sheet metal bending can be achieved using conventional bending methods including U-die bending [23], wiping die bending (L bending) [24], air bending (V-die bending) [25, 26], roll bending [27] and circular bending [28], some of which are illustrated in Fig. 1.3. A great deal of research has been done on these bending techniques. The past research dealt with the accuracy of bending [29, 30], numerical modeling of the bending process [31–35], bending process and optimization [36, 37]. Despite continuous research have been done on these bending techniques, the main issues remaining challenging are involvement of shape dedicated equipment such as die and mold set along with heavy machinery [38] and accuracy of bending due to springback [31]. For bending of specific component, a dedicated die/mold must be manufactured, which has distinct disadvantages such as expensive equipment investment, high maintenance cost of die/mold due to concerns for part quality, wear of die/mold, life-cycle restriction. In addition, manufacturing die/mold is a very time-consuming process [39].

Springback is believed to be caused by the tendency of sheet metal to return to original shape after forming operation. It is a main quality concern. If it exceeds designated tolerance, it causes severe problems in the following assembly operation. The concern for springback has grown due to trends of replacing steel with high strength steel and aluminum sheet metal components in the automotive industry. This material replacement brings a desirable low weight-to-strength ratio, which can increase fuel efficiency.

In this context, OSM bending can bring forward a new bending technique that is cost effective, accurate and easy to integrate into the current mass production workflow. As can be seen from the OSM bending configuration in Fig. 1.2, the die/mold set has been eliminated from the bending process. The elimination of die/mold from the bending process is achievable due to the introduction to the

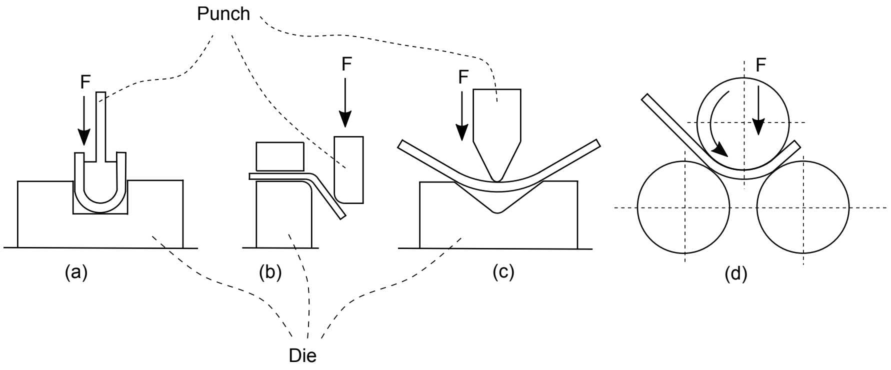

Figure 1.3: Common bending methods, (a) U-die bending; (b) wiping die bending; (c) air bending; (d) rolling bending.

material MD along the bending line. MD has taken the role of die/mold to predetermine bending line on a blank sheet. Current technology in laser cutting, water jet cutting, or progressive die stamping allows MDs to be cut on the blank sheet with ease prior to bending operation. In the cutting process, the material can be completely removed from through-thickness direction or partially removed. The desired angle of bending can be achieved by controlling the movement of punch in X, Y directions. With these features, OSM bending can solve challenges encountered in conventional sheet metal bending techniques.

1.1.2 Rigid origami perspective

OSM bending falls under the category of rigid origami application for sheet metal. Rigid origami is a branch of origami that deals with folding structures using flat rigid sheets joined by hinges. Traditionally, a zero thickness is assumed in origami because paper is the main material used. With the increase of origami inspired research in engineering, non-zero thickness integration into origami structures are demanded. In result, many methods have been purposed to integrate non-zero thickness into origami. Thickness consideration in origami was firstly purposed by Hoberman [40]. His approach is summarized as "degree-4 vertex by thick panels that connects shifted axes of rotation using plates with two levels of thicknesses". Trautz and Kunstler [41] presented a slidable hinges method in which hinges can slide. Tapered panel method by Tachi [14] shifts rotational axis to alternative side with respect to sheet thickness. Tachi's work achieved the foldability of rigid panels with finite thickness by shifting the folding axes, his work also included removing material near the fold line to enable folding. However, the material removal technique presented in Tachi's work assumes a combined pattern for the flat layout of the rigid origami, where the faces of a 3-D structures are made of separated thick panels with stiff material, while the fold lines are created by a flexible material such as cloth or rubber created on a secondary flat pattern and attached to the panels. Hoberman [42] patented another method that arranges hinges on different planes so that the axis of hinges doesn't intersect with each other. In result, hinges are offset to each other and with respect to the basic plane of the sheet as well. Zirbel et al [10] presented the membrane folds method, which utilizes a thin flexible membrane under a thick material. A certain amount of gap is left between two adjacent thick material blocks according to the intended bent angle. e.g., two times of thick material thickness is proper if the bending angle is $180^{\underline{o}}$. Abel et al [43] presented offset crease method. In this method, a hinge axis is shifted to the middle of the material. Gaps are added to each fold on the alternative side of the hinge axis. Chen et al [44] presented spatial linkages method and another method, called offset panel, was presented by Edmondson et al [45]. Ku and Demaine [46] proposed a new algorithm to accommodate thickness in origami structure. In their method, new creases are created by offsetting crease-pattern faces from their flat folded state keeping the order of layer. It includes six steps, those are: determining crease width, polygon construction, refining the newly generated creases and polygons, setting scale factor, final construction and adding thickness to the crease pattern. Erica [47] et al summarized various thickness adaption approaches – shown in Fig. 1.4 [48], by illustrating the advantages and disadvantage of each method in the context of manufacturing. They showcased a square-twist mechanism for the viability of using sheet metal in origami adapted products.

As can be seen from Fig. 1.4, the flat sheets are joint by a hinge, which doesn't deform. In OSM bending, the web – defined as the connection between two neighboring MDs along the bending line, can serve as hinges. Unlike the rigid origami, the web undergoes deformation, which introduces mechanics into the picture. In addition, it appears the thickness accommodation approaches emphasize on creating a complex 3-D structure as it can be done using paper. However, OSM bending focuses on the rigid origami problem from manufacturing and mechanics point of view. From the manufacturing point of view, OSM bending brings forward a new forming technique. From the mechanic's point of view, it deals with deformation, load bearing capability, bending accuracy.

1.1.3 Perforated sheet metal perspective

MDs can be regarded as perforation on a blank sheet. So, OSM bending can be considered as bending of perforated sheet metal. So, it begs a perspective from a perforated sheet metal point of view. Perforated sheet is widely used in mechanical, aerospace and civil engineering structural elements. Examples are heat exchange equipment, shadow masks [49, 50], construction equipment [51], cold-formed thin-walled steel structures [52], beam [53], sandwich panels in building [54]. In many cases perforation has been the means of creating light-weight structures, ease of

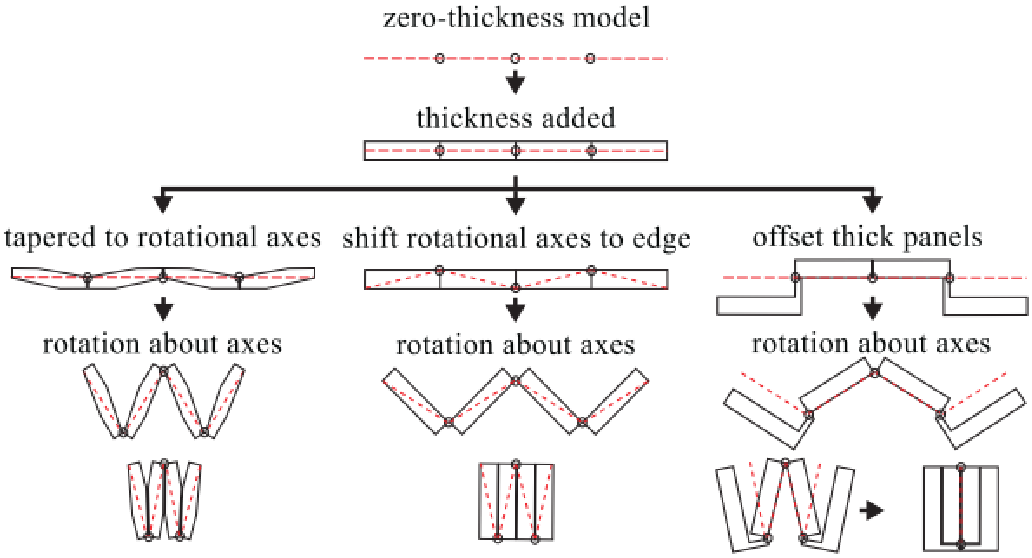

Figure 1.4: Thickness accommodation approaches to rigid thick origami

access point. However, perforation can also the means to create/form 3-D structure from a flat sheet of metal. In this sense, the role of perforation can be similar in function to the MD in OSM bending process. Literature [55–70] show that perforated sheet has been researched under various loading conditions with different hole types and hole orientation to investigate deformation behavior. Studies also investigated stress, stress concentration, and buckling effects. In sheet metal forming field, Ajudia and Dangar [71] presented a review on forming of perforated sheet metal. Nakayama et al [72] studied elastic-plastic deformation behavior of sheet perforated with circular holes evenly distributed all over the sheet. It is found that distribution and arrangement of holes significantly affect deformation behavior of sheet due to stress concentrations generated near the holes. Elangovan et al [73, 74] showcased formability of perforated aluminum sheets using an artificial neural network. It is found that formability of perforated sheet increases marginally as ligament ratio increases or percentage of area decreases. Farsi and Arezoo [75] investigated bending force and springback on low carbon steel sheet with oblong holes on the bending surface in V-shaped die bending setup. The influence of the area of holes, die angles, die width, and punch radius on the value of bending force, and springback angle is studied. It is concluded that increasing the area of hole leads to the reduction in spring back as well as bending force. Nasrollahi and Arezoo [76] presented the effect of hole type, the number of holes and ratio of the hole with sheet width on the springback in wiping die bending setup. They found that springback caused by different hole types increased in the following order – square, oblong and circular holes. Presence of a hole is the reason for less springback. Having more holes in the part decreases springback slightly. Senthilnathan et al [77] reported electromagnetic forming of perforated aluminum sheets using FEA. Kothari and Jhala [78] investigated the impact of material thickness, type of blank, blank shape, shape and pattern of perforation, the pitch of perforation on stress and load-displacement relationship. Venkatachlam et al [79] presented forming limit of stretch forming of perforated aluminum sheet with circular, triangular and slot type of holes. Sheet with circular holes exhibited more major and minor strains than that of triangular and slot type of holes. In these studies, simple perforations such as holes, squares, and other shapes are studied to investigate the effect of perforation on the component or process considered. Perforations are simple if compared to MDs shown in Fig. 1.1. Further, the effect of MD in forming has not been understood. In addition, OSM bending takes advantage of MD to accomplish bending rather than seeing the perforation as a defect in the structure.

1.2 Objective

Considering the literature, the goal of the dissertation is to better understand the mechanics of OSM bending in order to close the gap in fundamental understanding leading to the development of a more precise, economic, and sustainable sheet metal bending technique. Specifically, the current work attempts to answer a series of questions about OSM bending in terms of feasibility, force requirement, deformation, accuracy, and proper scale of MDs and failure possibility; those are:

- What are the impacts of OSM sheet in the conventional sheet metal bending process?
- Is OSM bending conceptually feasible such that 3-D OSM bent structures are formed form a 2-D metal sheet?
- What are the manufacturing parameters that are necessary to achieve successful OSM bending? What is their impact on the OSM bending process.
- How can the OSM bending force be modeled analytically and empirically?
- How does the OSM behave if it is subjected to tension and shear loads?
- How should the optimal MD parameters be selected so that it leads to the desired bending outcome without failure of the blank sheet?

Therefore, the first objective of the dissertation is to perform FEA on the effect of OSM sheet in conventional bending configuration. This is presented in Chapter 3. Then, in Chapter 4, OSM bending process is defined in a similar manner as the conventional sheet metal forming processes. Parameters associated with OSM forming and design of MDs are identified. Comprehensive FEA is carried out to assess feasibility of OSM bending process with the correlation of OSM design and process parameters. In Chapter 5, a bending force model is developed analytically and experimentally. In chapter 6, response of MDs under tension and shear is investigated in light of fracture using experimental and FEA case studies. In chapter 7, a study is conducted to predict possibility of fracture in OSM bending under the impact of different scale, sheet thickness and types of MDs. Finally, Chapter 8 is reserved for conclusion and future extension of the work.

Chapter 2

METHODS

2.1 Overview

In this chapter, finite element analysis (FEA), digital image correlation (DIC) are introduced as these are main numerical and experimental tools used to carry out the study.

Numerical simulation techniques in sheet metal forming [31,35,76,80,81] have been widely used in research to facilitate fundamental understanding. Numerical simulations are recommended to be performed prior to experiments in order to increase productivity and reduce cost. FEA, Artificial Intelligence (AI), particularly artificial neural network (ANN) have been used to predict quantities in the forming process. Early works studied sheet metal forming using FEM date back to pioneer works by Wifi [82], Gotoh and Ishiseé [83], and Wang and Budiansky [84] in late 1970s. Since then, FEA technique has been expanded to a wide range of forming problems. Variety of general and specialized sheet metal forming simulation software has been developed to tackle problems in sheet metal forming. Currently, FEM is capable of providing cost-effective, efficient results to answer questions in sheet metal forming. Reported work [31,35,85–90] discussed different solution methods in simulation of sheet metal forming. Makinouchi et al. [91] classified formulation into three main categories, which are dynamic explicit, static explicit, and static implicit formulation. Further, solution strategies were categorized into three types, which are incremental method, large step method, and one-step method. Thus, in FEM codes, the various FEM formulations are combined with different solution strategies. In summary, one can classify solution methods into five different categories. They are static explicit method, dynamic explicit method, static implicit incremental method, static implicit large step method, and static implicit one-step method. These methods are compared with one another in the work of Oniate et al. [92] and Yang et al. [93], respectively.

These developments enabled numerical simulation, particularly FEM, to effectively and accurately simulate OSM bending problems. There are cases where FEA results alone are not enough to make the final judgment as FEA provides an approximated result to the problem analyzed [94]. The results of FEA are acceptable when it closely represents the phenomenon investigated. Other times, there is a need for experimental validation of FEA results. Therefore, in sheet metal forming, experimental testing and FEA are often used together [30]. Validating analytical analysis with experiments or FEA is also common due to the same reason mentioned above [27,95].

DIC is a non-contact, optical, deformation measurement technique by tracking the motion of the component. DIC was first introduced by researchers in 1980s [96]. DIC offers non-contact, full field, 3-D measurements for dimensions, deformations, shapes, structures in different environments and conditions. Over the years, it is continuously improved and now it is used in various fields [97,98]. DIC is also widely used in sheet metal forming [95,99,100]. DIC brings many advantages such as easiness to set up, flexibility, robustness against ambient disturbance, and spacial resolutions. In the following sections, the main procedures and principles of FEA and DIC is briefly presented.

2.2 FEA

2.2.1 FEA background

In essence, FEA is a tool to provide approximated solution to differential equations that describe a physical problem. The physical domain of interest is represented by an assembly of finite elements that are the result of discretization of the physical domain. Approximation functions of the finite element are constructed using physical value at the nodal points within the element. The physical values at the nodal points are the unknowns. With the discretization approach, the continuous physical problem is transformed into a system of algebraic equations that can be solved for the unknown nodal values.

The main steps of FEA procedure is summarized below.

- Discretization of the physical domain: the first step is to dissect the entire physical domain into finite elements or mesh elements.
- Selecting interpolation function: mesh elements discretized in the first step are represented using an approximated interpolation functions that is dependent on physical nodal values in the element.
- Establishing elemental properties: a set of algebraic equation are established to connect the physical nodal values to other parameters. Often, the Galerkin method or variational approach is used for this purpose.
- Global assembly of elements: elemental level algebraic equations are assembled into global equation system to find solution for entire physical domain. In this process, the boundaries and interfaces between the neighboring elements and nodes must satisfy the connectivity requirements and the boundary conditions.

- Solving global equation system: the assembled global equation system is solved using direct or iterative methods to obtain solution for the unknown physical nodal values.

- Post-processing: additional values of physical fields such as stress, strain are calculated based on the solution of nodal values such as displacement.

2.2.2 FEA formulation

Galerkin method is most popular method to transform partial differential equation of the physicals domain into finite element discrete system of equations. When the physical problem can be formulated as a minimization of a functional, variational approach can be used.

The formulation of FEA is illustrated using a one-dimensional (1-D) example below.

Suppose the physics of the domain of interest can be expressed by the following differential equation,

$$a\frac{d^2u}{dx^2} + b = 0, \qquad 0 \le x \le 2L \tag{2.1}$$

with boundary condition

$$\begin{aligned} &u|_{x=0} = 0 \\ &a\frac{du}{dx}|_{x=2L} = R \end{aligned} \tag{2.2}$$

where u is an unknown.

The discretization of the physical domain is presented in Fig. 2.1, in which the entire physical domain is discretized into two elements. Every element consists of two nodes. One the right panel of Fig. 2.1, the element is approximated with the function $u(x)$ as in Eq. (2.3), where N_i is shape function defined as in Eq. (2.4).

$$\begin{aligned} &u = N_1u_1 + N_2u_2 = [N]\{u\} \\ &[N] = [N_1 \qquad N_2] \\ &[u] = [u_1 \qquad u_2] \end{aligned} \tag{2.3}$$

$$\begin{aligned} &N_1 = 1 - \frac{x - x_1}{x_2 - x_1} \\ &N_2 = \frac{x - x_1}{x_2 - x_1} \end{aligned} \tag{2.4}$$

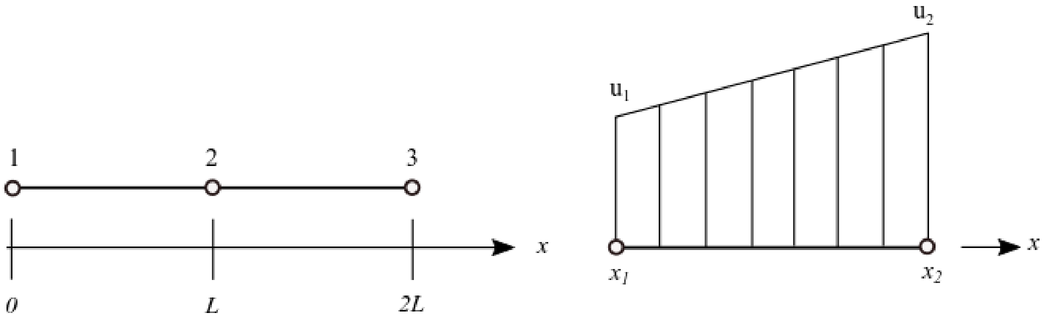

Figure 2.1: One dimensional linear elements and function interpolation on an element

The nodal values u_1 and u_2 are unknowns that can be solved from the global equation system.

Substituting u expressed through its nodal values and shape function, the differential equation takes the form as in Eq. (2.5),

$$a\frac{d^2}{dx^2}\left[N\right]\left[u\right]+b=\psi \tag{2.5}$$

where ψ is a nonzero residual caused by the approximate representation of a function inside a finite element. The Galarkein method minimizes the residual by multiplying the terms in Eq. (2.5) by shape functions and integrating over the element,

$$\int_{x_1}^{x_2}\left[N\right]^T a\frac{d^2}{dx^2}\left[N\right]\left\{u\right\}dx+\int_{x_1}^{x_2}\left[N\right]^T bdx=0. \tag{2.6}$$

Using integration by part, Eq. (2.6) leads to

$$\int_{x_1}^{x_2}\left[\frac{dN}{dx}\right]^T a\left[\frac{dN}{dx}\right]dx\left\{u\right\}-\int_{x_1}^{x_2}\left[N\right]^T bdx-\begin{Bmatrix}0\\1\end{Bmatrix}a\frac{du}{dx}|_{x=x_2}+\begin{Bmatrix}1\\0\end{Bmatrix}a\frac{du}{dx}|_{x=x_1}=0 \tag{2.7}$$

The Eq. (2.7) can be written as

$$\begin{aligned}
&\left[k\right]\left\{u\right\}=\left\{f\right\}\\
&\left[k\right]=\int_{x_1}^{x_2}\left[\frac{dN}{dx}\right]^T a\left[\frac{dN}{dx}\right]dx\\
&\left[f\right]=\int_{x_1}^{x_2}\left[N\right]^T bdx+\begin{Bmatrix}0\\1\end{Bmatrix}a\frac{du}{dx}|_{x=x_2}-\begin{Bmatrix}1\\0\end{Bmatrix}a\frac{du}{dx}|_{x=x_1}
\end{aligned} \tag{2.8}$$

where k is called stiffness matrix and f is the load vector. For the simple case considered here, the stiffness matrix and load vector are respectively equal to,

$$\begin{aligned}
[k_1] = [k_2] &= \frac{a}{L}\begin{bmatrix} 1, -1 \\ -1, 1 \end{bmatrix} \\
f_1 &= \frac{bL}{2}\begin{Bmatrix} 1 \\ 1 \end{Bmatrix} \\
f_2 &= \frac{bL}{2}\begin{Bmatrix} 1 \\ 1 \end{Bmatrix} + \begin{Bmatrix} 0 \\ R \end{Bmatrix}
\end{aligned} \tag{2.9}$$

These are equations for each element separately. The global system of equation is constructed as

$$\frac{a}{L}\begin{bmatrix} 1, -1, 0 \\ -1, 2, -1 \\ 0, -1, 1 \end{bmatrix}\begin{Bmatrix} u_1 \\ u_2 \\ u_3 \end{Bmatrix} = \frac{bL}{2}\begin{Bmatrix} 1 \\ 2 \\ 1 \end{Bmatrix} + \begin{Bmatrix} 0 \\ 0 \\ R \end{Bmatrix}. \tag{2.10}$$

Now the boundary condition $u(x = 0) = 0$ can be applied and it can be solved for u_i for a given values of a, b, L, and R.

2.3 Digital image correlation

The experimental testing in this dissertation uses DIC technique to measure deformation on the sheet.

There are three steps to follow in order to utilize DIC technique, namely, (1) specimen preparation with speckle pattern; (2) recording images of the surface component on the part/specimen before, during, and after loading; (3) analyzing the acquired images to compute displacement/strain field on the surface component.

In the specimen preparation step, the surface of interest on the part/component is painted with a random distributed white and blank speckle pattern. During the image recording step, the imaging system shouldn't be disturbed by geometric distortion or external disturbances. Once the images are recorded, the motion of each point on the surface of interest is computed by the DIC based on the captured image of the surface at different stages of the deformation. The DIC divides the surface into evenly spaced virtual grids. The displacement is computed at each point of the virtual grid tracing or matching the same points between the images recorded before and after loading. Each grid is assigned to a gray level value based on the random speckle patter applied. The gray level assists in distinguishing every grid uniquely. To assess the motion between the reference grid and the deformed grid, a cross-correlation criterion or sum-squared difference correlation criterion is executed.

As per deformation continuity in solids, a subset of neighboring points in reference frame stay as neighboring points in target deformed frame. Through a displacement mapping function, the displacement of the reference subset can be mapped to the deformed subset. If applied to all subsets, this mapping yields the result in entire surface.

Chapter 3

OSM IN WIPING DIE BENDING CONFIGURATION

3.1 Background

In OSM bending, the MD is hypothesized to increase the accuracy of bending, process efficiency, and by extension, reduce the cost and energy. However, the current state of the art for the technique lacks the information to quantify the advantage of the OSM over the traditional manufacturing process of sheet metal, especially for mass production. For example, study [101] shows that to stamp 1 kg of steel, the energy spent in manufacturing process only can range from 5.1 to 9.69 MJ/kg due to the high tonnage presses involved and the energy lost in pressing machines.

The wiping die bending is one of the common sheet metal bending methods. The basic operation is to deform sheet under downward movement of a punch into 90°. The sheet is clamped between a die and a blank-holder. Schematic of wiping die bending is shown in Fig. 3.1.

Normally no MD is applied to the sheet in wiping die bending process. Hence, impact of OSM in a wiping die bending setup has not yet been investigated. This chapter attempts to gain insight into OSM mechanics by incorporating the MD in a wiping die bending setup as an initial exploring step. More precisely, the goal of this chapter is to investigate the effect of several MDs on the wiping die bending process. It ranks and evaluates qualitatively how the MDs affect the bending force (BF), stress concentration and resulted springback in wiping die bending process.

3.2 Selection of MDs

Among the MDs that researchers suggested in Fig. 1.1 [19, 20], some MDs have been already commercialized. In most cases, if not all, the MDs are arranged symmetrically along the bend line. Alternatively, the MD appears in symmetric pairs on the two sides of a bending line.

In this work, four different types of MDs are chosen for investigation, which are MD-1, MD-2, MD-3, and MD-10. As can be seen in Fig. 1.1, two rules govern the arrangement of the selected MDs along the bending line. One is that only one pair of MDs is arranged with respect to bend line. MD-1 and MD-2 are examples that MDs lie along the bend line. While, MD-3 and MD-10 are examples of positioning

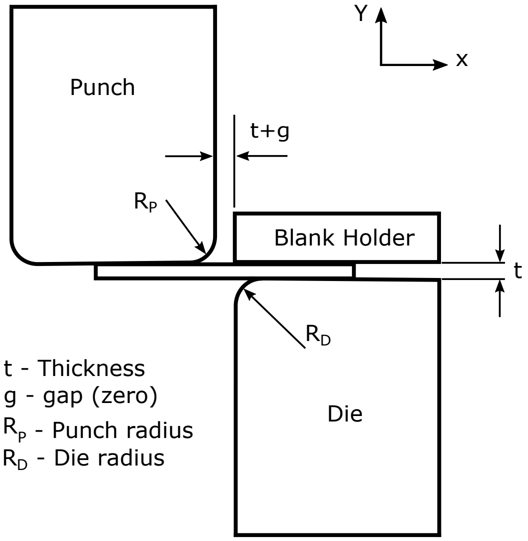

Figure 3.1: Wiping die bending Schematic

the MDs at the two sides of bend line. The second rule is regarding the percentage of removed material. In order to be able to make comparison between cases, the dimensions of MD are designed such that there are identical lengths of material left along the bending line after MDs are applied along the bending line of the sheet. In case these two rules conflict, rule one prevails.

3.3 FEA setup

The sheet is rectangular in shape having 50 mm in length, 50 mm in width, and 3 mm in thickness. The radius of die, (R_D), and the radius of punch, (R_P), are both set to 3 mm. Punch dimensions are 50 mm (width), 50 mm (height), 30 mm (length). Die dimensions are 50 mm (width) , 50 mm (height), 40 mm (length). Blank holder has dimensions of 50 mm (width), 10 mm (height), 40 mm (length). The aluminum sheet 2036-T4 is the sheet material. It has an ultimate tensile strength of 338 MPa, a yield strength value of 193 MPa, a strength coefficient of 598 MPa, and a strain hardening exponent of 0.216.

In the simulation process, the sheet is set to elastic–plastic with isotropic hardening since it experiences large deformation during the bending process. The boundary conditions are applied based on the schematic shown in Fig. 3.1. The die is fixed throughout the simulation. The blank holder is set to be free only in the Y degree-of-freedom. Displacement of the sheet in Z-axis is restricted due to symmetry condition, where Z-axis is the outgoing direction from the XY plane in Fig.

3.1. There are four steps in simulation. First, a ramped load with maximum value of $2\times10^5 N$ is applied on top of the blank holder to hold sheet firmly during bending. In the second step, 25mm of displacement in the negative Y direction is imposed on punch. By the end of the second step, bending will be completed. Third and fourth steps are to unload the sheet by separating punch from sheet and unloading blank holder so that springback can be evaluated. In order to achieve accurate results, five layers of 20-node hexa elements are generated along the thickness direction of sheet [102]. This would result in ten integration point along the thickness of sheet. The Punch, blank holder, and die are simulated as rigid bodies and linear four-node quadrilateral elements are used for them. The number of elements is kept constant for each of the die, punch, and blank holder in all cases. Mesh of the sheet is dominantly made of 20-node hexahedron elements, but prism elements are also generated around the MD. A refinement is made along with the bending line. A typical meshing of sheet is illustrated in Fig. 3.2.

Friction coefficient of 0.12 is considered in these simulations. There are three frictional surface-to-surface contact pairs between the sheet and rigid parts (punch, die, and blank holder). Augmented Lagrangian formulation is used for contact simulation.

A wiping die bending case with regular sheet is also simulated. The reason is to compare the regular sheet that has no MD and the sheets having MDs in terms of bending force required to bend the sheet, maximum stress caused during the bending, and springback angle. The regular sheet will serve as a benchmark. In addition, the comparison between the different shapes of MD can assist in designing OSM parts with optimized bending force requirements and stresses generated along the bend line. Hence, there are four cases where sheets with the chosen MD are simulated while the last one is a regular sheet without any MD.

3.4 Simulation results

Overall, simulation process went well except convergence problem. Obtaining full convergence of simulation especially in the bending process (which is second step in simulation) became problematic. The reason is diagnosed to be applying punch displacement boundary condition too fast and elements become highly distorted. It is overcome by increasing number of time steps, i.e., slower application of loads. Number of time steps required for convergence at the bending process varies over different MDs. The regular sheet and MD-10 required 200 time steps while MD-1, MD-2, and MD-3, needs 250 time steps. These time steps are uniformly applied during the bending process.

3.4.1 Mesh convergence study

In order to achieve accurate results from the simulation, mesh convergence studies have been conducted. Each MD case is simulated with finer mesh size along

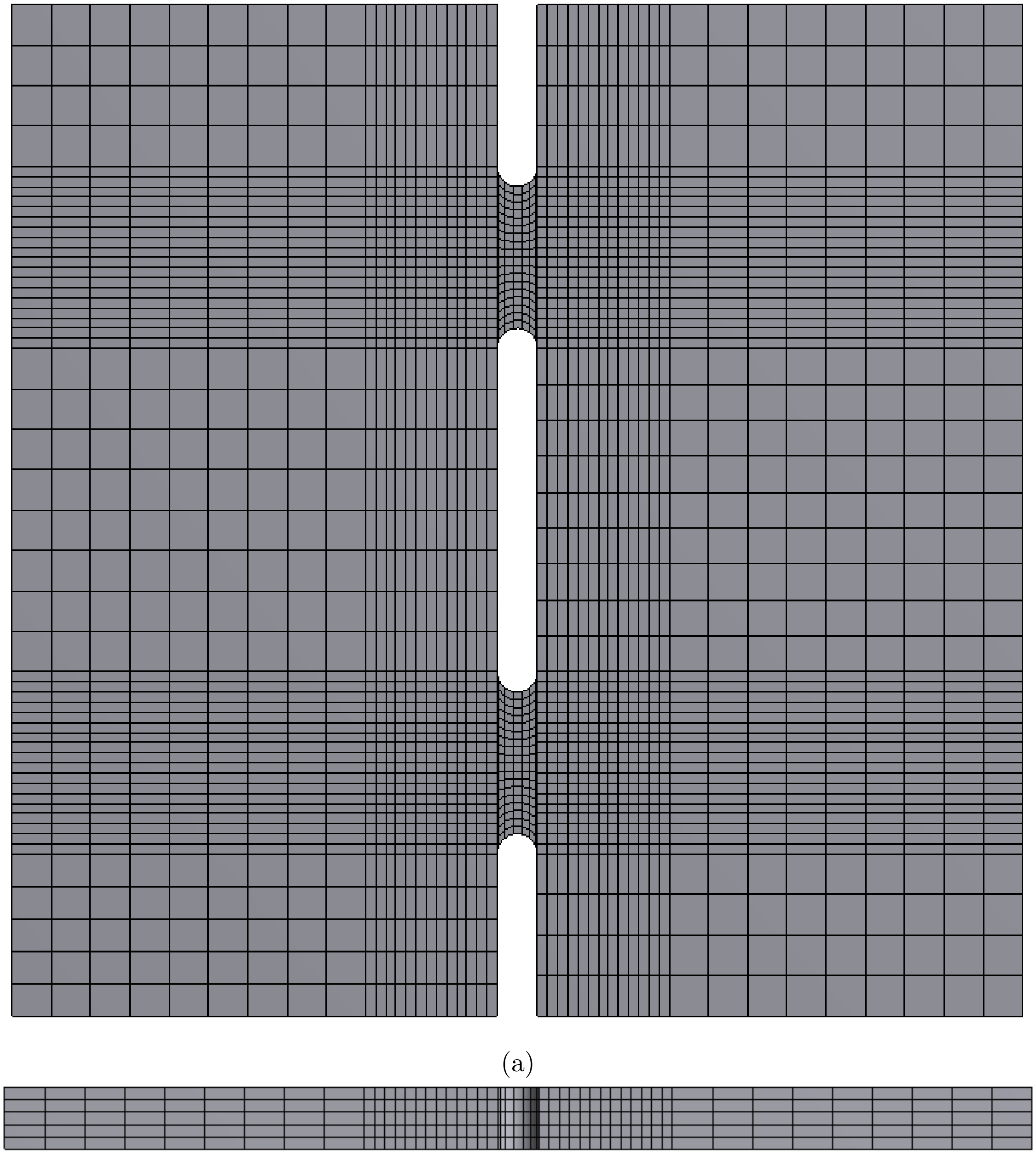
(a)

(b)

Figure 3.2: Meshing illustration, (a) meshing of MD-1, top view; (b) MD-1 five mesh layers in thickness direction

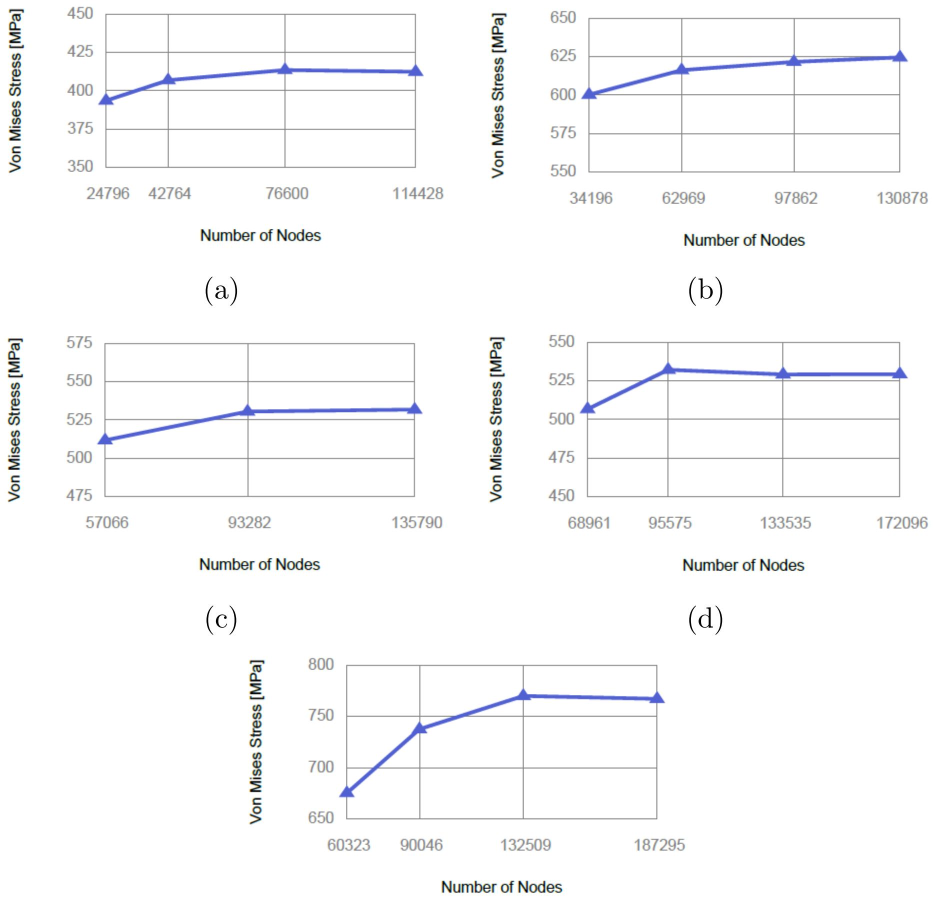

(a) (b) (c) (d) (e)

Figure 3.3: Mesh convergence studies results, (a) without MD; (b) MD-1; (c) MD-2; (d) MD-3; (e) MD-10.

the bending line of sheet until mesh convergence is obtained. Then variation of maximum Von Mises stress is evaluated over mesh sizes. Fig. 3.3 shows the result of mesh convergence studies.

3.4.2 Required bending force

Bending force is evaluated for all cases over the punch displacement. Figure 3.4 shows that in all studied cases, the bending force over the punch displacement has a similar pattern. It increases to a maximum value and then decreases followed by a rather steady value to the end of punch displacement. As expected, bending force required for sheets with MD is reduced substantially compared to the sheet that has no MD. The reduction of the magnitude of the required bending force varies depending on the type of MD, see Table 3.1. The reduction reaches as high as 59%

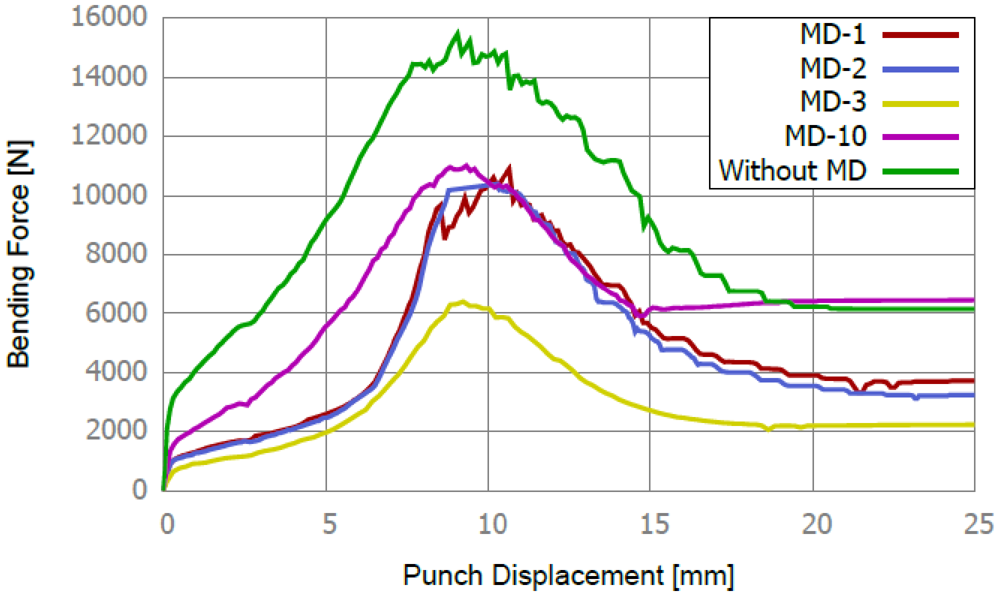

Figure 3.4: Bending force versus punch displacement plot for each of the studied MD cases and the traditional sheet metal case with no MD along the bend line

in the case of MD-3, which is the maximum reduction, and it is 29% in the case of MD-10, which is the least reduction among the four cases. The reduction implies the possibility of performing bending operation with light tools even by hand for some sheet metal thicknesses. Physically, the reduction in the required bending force is a result of the removing materials along the bend line that resist to punch movement and thus there are less resisting force to bending.

In the case without MD, the bending force-punch displacement curve displayed a series of fluctuation after reaching the maximum bending force value. This phenomenon is caused by the deformed material flow that has been accumulated within the gap between punch and die. As the punch goes down, the sheet experiences more deformation and as a result deformed material flows to the gap between the punch and die. As more material accumulates in the gap, it increases the resistance to the punch movement and the resistance caused fluctuation of bending force.

3.4.3 Empirical evaluation of bending force

The simulation result is validated through empirical formula that predicts the maximum bending force for a wiping die bending. The maximum bending force for a wiping die is given in Eq. (3.1) [76],

Table 3.1: Bending force (BF) evaluation

Cases	Simulated BF (N)	Emperical BF(N)	Reduction in BF compared to no MD (%)
MD-3	6398	—	59
MD-2	10362	—	33
MD-1	10900	—	29.5
MD-10	11012	—	29
Without MD	15459	15210	—

$$F = \frac{M}{l}(1 + sin\phi), \tag{3.1}$$

where F is the bending force, l is the die opening, $l = R_D + R_P + t$, R_D is the radius of the die, R_P is the radius of the punch, t is the thickness of the sheet, and ϕ is the bending angle, in this case ϕ is equal to 90°, M is the bending moment, which is found using Eq. (3.2),

$$M = n(UTS)\frac{bt^2}{4}, \tag{3.2}$$

where n is correction coefficient hardening of a material (n = 1.6–1.8), UTS is the ultimate tensile strength of a material, b is width of the beam (length of bending) and t is the material thickness. Using Eq. (3.1), the bending force for the sheet without MD is found to be 15210 N (for $n = 1.8$), which is in good agreement with the bending force obtained from the FEA model, with a difference of 1.6%.

As for the evaluation of empirical bending force for the cases of MDs, Eq. (3.1) cannot be used directly since the bending force is supposed to take into account the amount of material removed along the bending line. Hence, further investigation on the mechanics of MD is needed to develop general mathematical/ empirical model for the calculation of bending force when MD exists on the bend line of a sheet. It is hypothesized that the bending force reduction is related to the percentage of material removal in each MD case. In order to validate this hypotheses, volume of material removal in each MD case is tabulated in Table 3.2. It is noticed that the bending force reduction is not proportional to percentage of material volume removal. Implication of this hypotheses needs more rigorous studies.

3.4.4 Stress evaluation

Von Mises stress is evaluated for all cases when the sheet is bent to 90°, as shown in Fig. 3.5. High stress is distributed along the bending line in all cases while

Table 3.2: Relation between BF and material removal volume

Cases	Sheet volume (mm^3)	Reduction in volume wrt. no MD (%)	Reduction in BF wrt. to no MD (%)
MD-3	7125	5	59
MD-10	7195.2	4.1	29
MD-2	7225	3.7	33
MD-1	7289.2	2.8	29.5
Without MD	7500	0	—

Table 3.3: Maximum equivalent stresses

Cases	Max value (MPa)	Increase due to MD (%)
MD-3	529.3	27.2
MD-2	531.8	28
MD-1	624.6	50.1
MD-10	767.2	77.3
Without MD	426.0	—

the rest of the sheet body is subjected to less stress compared to the area along the bending line. Von Mises stress values are higher when MDs are present on the sheet. The simulation results indicated that, with the effect of MD, the von Mises stress increased by 27.2% at minimum and by 77.3% at maximum. Due to presence of MD, the stress distribution along the bend line is no longer uniform as in the case of the sheet without MD, see Table 3.3 and Fig. 3.5. It is found that Von Mises stress in MD-2 decreased by 22.1% compared to MD-1. This is due to topological differences between MD-1 and MD-2. The enlarged circular openings in MD-2 helped transmit the stress into sheet body and thus it has less stress concentration. This indicates that the topological variation in MD can be utilized to reduce stress concentration depending on the design requirements of the sheet metal product. Based on the results, MD-3 has overall best performance. The underlying reason is due to its profile—particularly, due to the fact that the profile of MD-3 has a larger radius of curvature along the bend line, which translates force easier compared to other MD profiles. The same can be said about MD-2. As for MD-10, the reason for it to be the highest in increase of stress is because of the edge-to-surface contact between edge of MD-10 and surface of punch during bending. That is why maximum stress occurred on the edges of MD-10, as shown in Fig. 3.5.

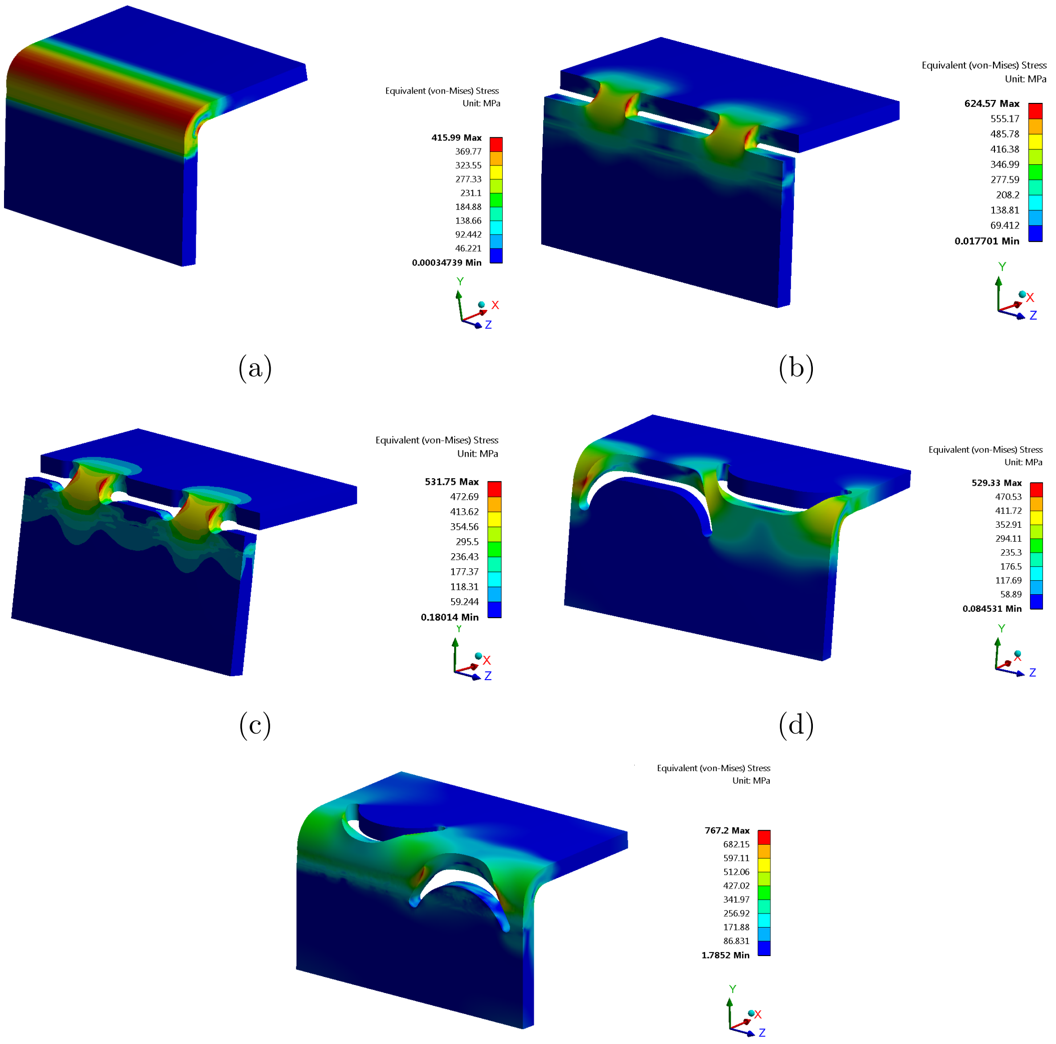

(a) (b) (c) (d) (e)

Figure 3.5: Von Mises stress distribution for each MD case under study, (a) without MD; (b) MD-1; (c) MD-2; (d) MD-3; (e) MD-10

Table 3.4: Springback angle after bending

Cases	Angle (°)	Decrease due to MD (°)
MD-3	92.666	0.375
MD-2	92.524	0.517
MD-1	92.349	0.603
MD-10	92.488	0.553
Without MD	93.041	—

3.4.5 Springback

Springback angle after bending is calculated for all cases. The results are tabulated in Table 3.4. It can be seen that application of MD reduced springback for all four MD cases. This conclusion validates similar results found in perforated sheet [76], where application of perforated feature at the bending area of sheet metal reduced springback. This implies potential of MD in reduction of springback.

3.5 Summary

The key element in this process is creating MD along the bend line that enables folding with reduction in the required bending force compared to the traditional wiping die bending. The shape and geometry of MD affect the required bending force. For the selected MD shapes, the required bending force was substantially reduced for all four cases in the FEA model. This reduction is caused by the material removal along the bend line leading to less material available to resist the bending force. The magnitude of reduction in bending force is associated with the percentage of volume removal. However, this relation between the percentage of material removal and resulting bending force is not proportional. Future chapters will focus on defining the exact relationship between the MD profile and the resulting bending force. Due to the small dimensions of MD, high stress concentration is generated along the bend line. On the other hand, the stress concentration can be effectively reduced with topological variation of the MDs and by introducing changes to the MD profile. In addition, the application of MD leads to decrease in springback effect.

Chapter 4

INVESTIGATING PROCESS AND DESIGN PARAMETERS IN OSM BENDING

4.1 Background

In the current literature, OSM bending has been studied from the perspective of fabricating 3D parts by a sequence of folding or bending from a single 2D blank metal sheet. The topological variations of one 3D geometry in its 2D flat pattern state can result in various feasible 2D flat patterns that all can be successfully folded to the same 3D geometry [103–105]. A specific flat pattern can be selected based on a manufacturing aspect such as nesting efficiency, scrap percentage, and ease of folding and handling [106].

There are several reported applications of OSM bending and MD in loading bearing structures. Venhovens et al. [106] presented an application of OSM bending in vehicle body-inwhite. In their work, they showcased a new concept of vehicle body-in-white that eliminates the use of metal stamping, shape dedicated die, or mold tools associated with the stamping process. Shi et al. [4] developed a new folded assembly that mimics the behavior of simple triangle truss under compression load. In the folded assembly, they took advantage of MDs when the sheet is folded to triangular truss structure. Li et al [107] showcased a triangular and trapezoidal corrugated cardboard structure made of thin Aluminum 1060 sheets using OSM principle. Under out-of plane crushing and quasi-static crushing tests, this approach demonstrated superior performance than corrugated structures fabricated using conventional method. This implied the potential of OSM approach in enhancing energy absorption of corrugated structures. However, it is noticed that these studies are restricted to the application level of MD in sheet metal structures. There has been a need to understand the performance of MD and the OSM bending process itself from a mechanics point of view. This chapter attempts to fill the gap and to present a clear understanding of how OSM bending process is achieved and how associated process and design parameters affect the result of OSM bending. So, this work aims at providing a guideline for selecting OSM bending process parameters as well as MD design parameters. This objective is achieved in two steps. First is to identify parameters of MD and OSM bending process. Second is to investigate how the identified parameter affect the OSM bending process. Parameters studied are looked at from MD design point of view and OSM bending process point of view. When investigating the effects of identified parameters, parametric study approach is utilized coupled with finite element analysis (FEA), and the identified parameters are evaluated in terms of maximum bending force and maximum stress along the bend line and resulted in springback angle during OSM bending.

4.2 Methodology

The approach taken to reach the objective of this chapter is outlined as follows. First, the OSM bending process is introduced, followed by identifying and defining parameters from OSM bending process point of view and MD design point of view. Then, parametric FEA study is presented on the effect of each of the parameters identified on OSM bending. Finally, a generic guideline is offered for selecting parameters pertaining to the OSM bending process as well as MD design.

4.3 Difference between OSM bending and wiping die bending

The OSM bending process appears to be similar to wiping die bending. Figure 1.2 and Fig. 3.1 demonstrate the OSM bending and the wiping die bending configuration, respectively. However, close observation reveals that OSM bending differs from wiping die bending in a few aspect. First, OSM bending requires no die while wiping die bending needs a die to bend the sheet. Secondly, in OSM bending, location of the bending line is predetermined by MDs. In origami, each fold is made based on a bend line pattern that can either be determined or undetermined in a given 3D geometry [108, 109]. In OSM bending, a topological analysis is required to determine the bend line prior to bending the metal sheet [110]. In the OSM bending configuration shown in Fig. 1.2, the bending line is predetermined by the MDs. The position of the punch can be anywhere between the s+t and L/2, where s, t, and L are offset distance, sheet thickness, and the length of the sheet. As a result, the punch is required to complete the motion in both the horizontal and vertical direction. In wiping die bending, the punch moves in a vertical direction only. Thirdly, in OSM bending, the support can have an offset distance, denoted by s, from the bending line.

4.4 Identifying and defining parameters

OSM bending has many parameters that affect the bending process. However, from the bending process point of view and MD design point of view, six different parameters are identified. These parameters are selected because they are common to all MDs and OSM bending processes. These parameters can be categorized into two main categories. The first category is parameters associated with the MD and the blank sheet itself. The second category is pertaining to the bending process such as the placement of sheet, punch, and other physical conditions in the process.

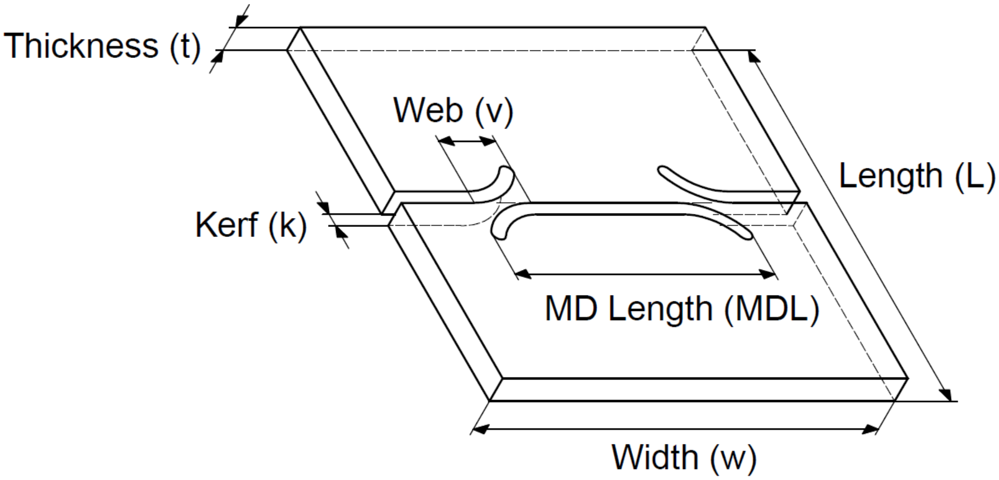

Figure 4.1: Generic design parameters of MD

The design parameters investigated in this chapter, shown in Fig. 1.2 and Fig. 4.1, are the kerf-to-thickness ratio (k/t), the thickness of the sheet (t), and the web-to-width ratio (w/b). Process parameters include punch placement (g), punch radius (R_P), and offset distance from the bending line (s). These terms are explained as follows:

- The thickness of sheet (t): this is the thickness of the sheet. It is assumed that the sheet has a uniform thickness throughout the whole body.
- Kerf-to-thickness ratio (k/t): is the ratio between the kerf (k) and the sheet thickness (t). Kerf is the cutting width that the laser or water jet cuts out of the sheet.
- Web-to-width ratio (w/b): web (w) is defined as the remained distance between two consecutive MDs after removal of material along bend line due to the application of MD. It is the section that connects neighboring MD along the bend line. Length of the web is measured along the bend line. It is denoted by w/b, where w represents web and b is the width of the sheet.
- Punch placement (g): it is the distance between the blank holder and punch.
- Punch radius (R_P): it is the radius of punch that stays in contact with the sheet during the bending process.
- Offset distance (s): it is the distance between imaginary (predetermined) bend line determined by MD and edge of the blank holder (or support).

Table 4.1: Base values and a full list of values for each parameter under study

Parameters	Baseline value	Full list of values
Kerf-to-thickness (k/t) ratio	0.3	0.2, 0.3, 0.4, 0.5
Sheet thickness [mm]	1.628	1.628, 2.304, 3.264
Web-to-width (w/b) ratio	0.28	0.28, 0.40, 0.52
Offset distance (s) [mm]	3	3, 6, 9
Punch placement (g) [mm]	23	13, 18, 23
Punch radius (R_P) [mm]	3	1, 2, 3

Note that these parameters are common to all OSM bending and MDs. Fig. 1.2 and Fig. 4.1 illustrate process parameters and these generic design parameters of MD with the example of MD-3, respectively.

4.5 FEA of OSM bending

4.5.1 FEA setup and case studies

In this chapter, FEA is performed using the OSM bending configuration shown in Fig. 1.2 . MD-1, MD-2, and MD-3 are selected from all possible MDs shown in Fig. 1.1 since these three MDs can be bases for other MD patterns. Baseline value and a full list of values for each parameter assigned for the simulation are listed in Table 4.1. In these case studies, we presented studies on single parameter effect. Therefore, only one parameter is changed at a time while keeping all others at the baseline value and 42 FEA cases are performed in total.

In order to achieve accuracy in simulation, mesh convergence study was performed on one representative case for each MD and critical mesh size is determined. Then, all the other cases used the critical mesh size or even finer mesh. The parameters of a representative case of each MD are identical to baseline values listed in Table 4.1 except kerf-to-thickness ratio is set to 0.2. The reason for selecting 0.2 as representative cases is that the kerf is smallest and mesh convergence on this case would lead to convergence on larger kerf.

In addition, due to symmetrical nature of MD along the bending line, as shown in Fig. 4.2, a quarter of MD-1 and MD-2, half of MD-3 has been used in the simulation.

In FEA, the punch, the support, and the blank holder are modeled as rigid bodies, and all rigid bodies are discretized with the four-node rectangular element. The sheet is assigned as a deformable body. It has dimensions of 50 mm×50 mm × 1.628 (2.304/3.264 mm). Sample dimensions of these MD with baseline values are

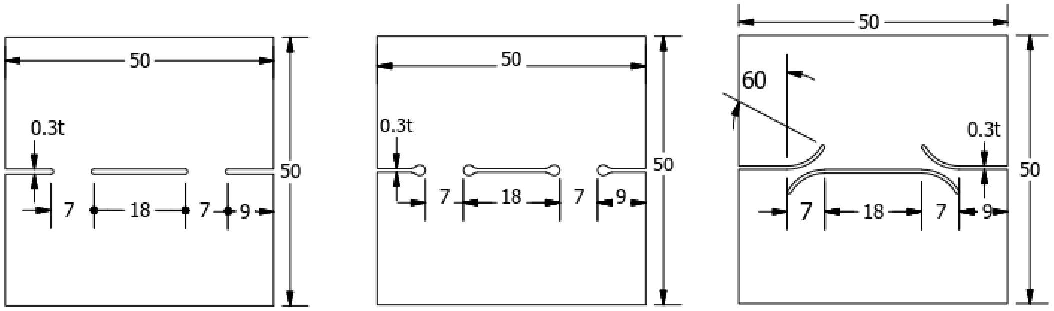

(a) (b) (c)

Figure 4.2: Sample dimension of MD with base values, (a) MD-1; (b) MD-2; (c) MD-3.

shown in Fig. 4.2. The sheet material is set as an elasto-plastic type with 20 node hexa-dominant elements.

It is reported [111–113] that generated mesh can affect obtained results and stress intensity factor. Per their research results, symmetrical and fine mesh around region along bend line has been generated, see Fig .4.3, where the mesh is shown on the portion of geometry that symmetry has been applied in order to show details. Implicit quasi-static finite element method of commercial code Ansys®18 is used for simulation. The material of the sheet is Aluminum Alloy 2036 (AA-2036), which has 193-MPa yield strength and 338 MPa for ultimate tensile strength (UTS) [114–116]. The plastic property of sheet is assumed to be isotropic and described by von Mises yield criteria. Elasto-plastic isotropic bilinear hardening model is used [117]. Strength coefficient (tangent modulus) and strain hardening coefficient of the sheet are 589 MPa and 0.216, respectively. The other material properties are tabulated in Table 4.2.

Simulation is performed with four steps. First, pressure load is applied on the blank holder as a preparation for bending of the sheet for the next step. Then, the punch is displaced with given values to accomplish bending of the sheet. Third and fourth steps are unloading of the sheet, where the punch is moved away from the sheet and the pressure load is removed.

4.6 Results

4.6.1 Mesh convergence study

Figure 4.4 shows the mesh convergence study result. Refinement of the mesh is stopped when the difference between refinements lead to less than 4% of the difference in terms of Von Mises (equivalent) stress.

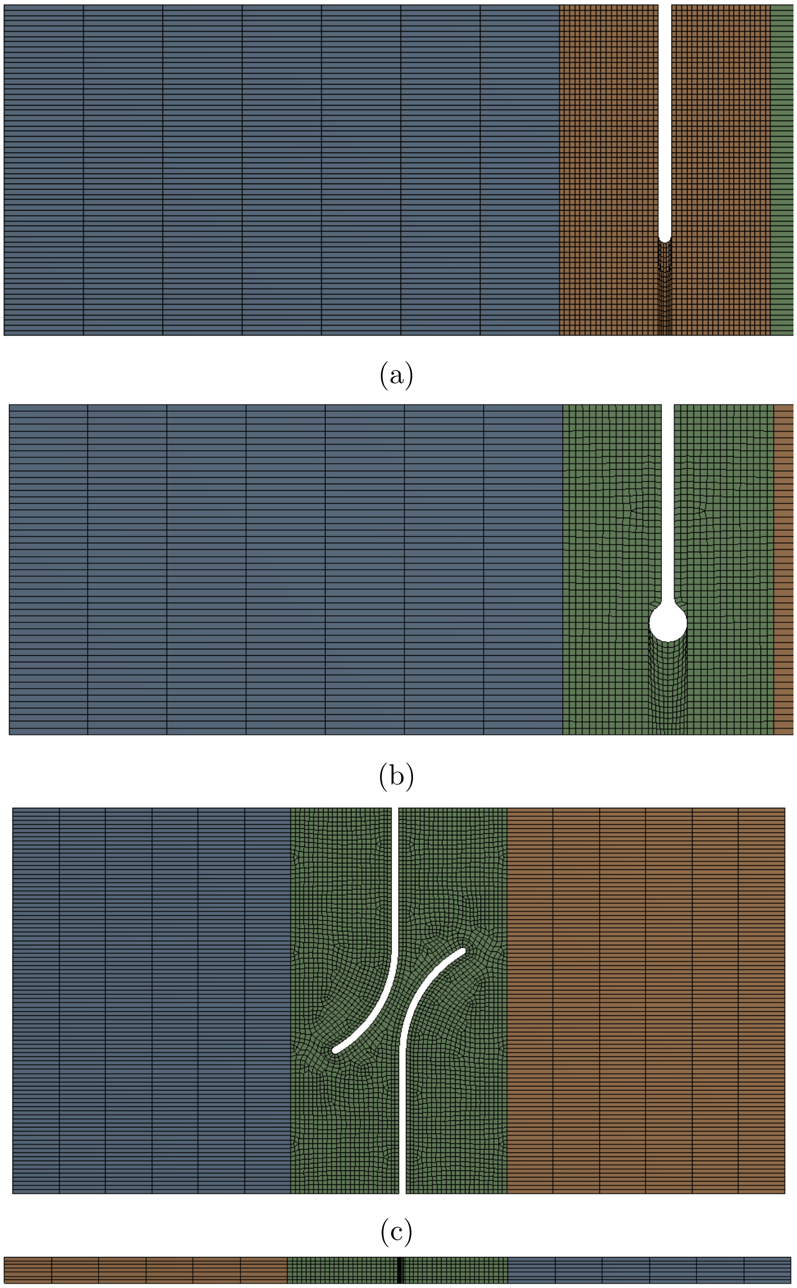

(a)

(b)

(c)

(d)

Figure 4.3: Meshing. A symmetrical mesh is generated for all cases. In (a) and (b), right part of the image is cropped to show details of mesh along MD

Table 4.2: Finite element simulation conditions

Item	Description
Object type	Sheet: elastic-plastic Punch/blank holder/support: rigid
Element type	20-node hexa element for the sheet 4-node rectangular element for rigid bodies
Material property	Al-2036 T4 Ultimate tensile strength, 338 MPa Young's modulus (E), 70 GPa Poisson's ratio (ν), 0.33
Sheet dimension	Length (L), 50 mm; width (w), 50 mm
Sheet thickness (t)	1.628/2.304/3.264 mm (14/11/8 gauge)
Bend angle	90°
Punch radius	(R_p) 3/2/1 mm
Friction coefficient (mu)	0.12
Punch motion	$g - s - t$ (mm) in positive X-axis 20 mm in the negative Y-axis
Bend line offset (s)	3/6/9 mm
Gap (g)	23/18/13 mm

4.6.2 Feasibility of OSM bending without die

OSM bending configuration is analogous to cantilever beam where the clamped portion of the sheet represents a fixed end of a cantilever beam and the motion of the punch can be seen as a load applied at a certain point on the beam. Unlike the bending of the cantilever beam, the blank sheet in OSM bending configuration is in fact clamped at the virtual bend line due to the application of MD and the offset distance, s, as shown in Fig. 1.2. As a result, the bending takes place along the location where MD is applied as the punch starts its motion. With this principle in mind, the punch is initially positioned 20 mm away to the left of the bend line, and the offset distance s is set to 3 mm in the FEA setup. To bend blank sheet into 90° the punch moves $g - s - t$ distance in the positive X-axis and 20 mm in the negative Y-axis direction. The different MDs on a 90° bent sheet are shown in Fig. 4.5. These results confirm the feasibility of bending sheets without using a die in OSM bending process.

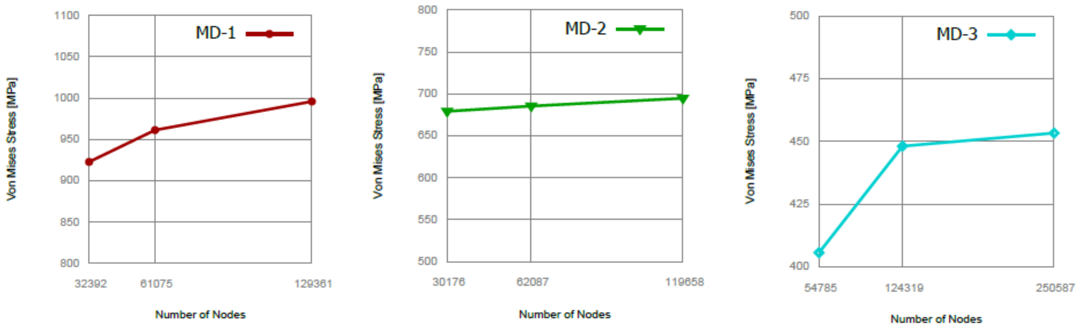

(a) (b) (c)

Figure 4.4: Mesh convergence study results

4.6.3 Effect of kerf-to-thickness (k/t) ratio

A group of 12 FE simulations is performed to investigate the effect of k/t ratio. For each MD type considered, the k/t ratio is changed from 0.2 to 0.5 and all other parameters are kept at the same baseline value tabulated in Table 4.1. Figure 4.6 and Table 4.3 show the results of maximum bending force requirement, maximum Von-Mises stress along the bend line, and final bend angle after springback with respect to different k/t ratios. From Fig. 4.6, it can be seen that the stress has a decreasing trend as the k/t ratio increases. This is because of two reasons. First, an increase in the k/t ratio creates a larger gap between opposite edges (surfaces) of MD. A larger gap leads to a reduced possibility of contact between opposite edges (surfaces) of MD [17]. Secondly, larger curvature radius at the ending of the MD have less drastic curvature change with larger k/t ratio and this allows the applied force to translate to the sheet body more smoothly. The force and stress on MD-3 is the least among the three MD types, since the oblique shape of MD-3 with respect to bending line spans from one half of the blank sheet to the other half with large radius curvature, MD-3 experiences torsion in addition to bending while MD-1 and MD-2 is subjected to only bending. The results show that MD-3 can translate the forces easily to the sheet body rather than concentrating it on the small area around the bend line. The results also showed that the stress on MD-2 is smaller than the one resulted in the MD-1 regardless of k/t ratio. The large opening circle at the end of MD-2 has played the role of relieving stress. The final angle after springback of all MDs is little influenced by k/t ratio.

4.6.4 Effect of sheet thickness (t)

The effect of thickness on OSM bending is investigated by performing nine FEA for three different thicknesses, those are 1.628 mm, 2.304 mm, and 3.264 mm. The results of sheet thickness effect are shown in Fig. 4.7 and Table 4.4. The

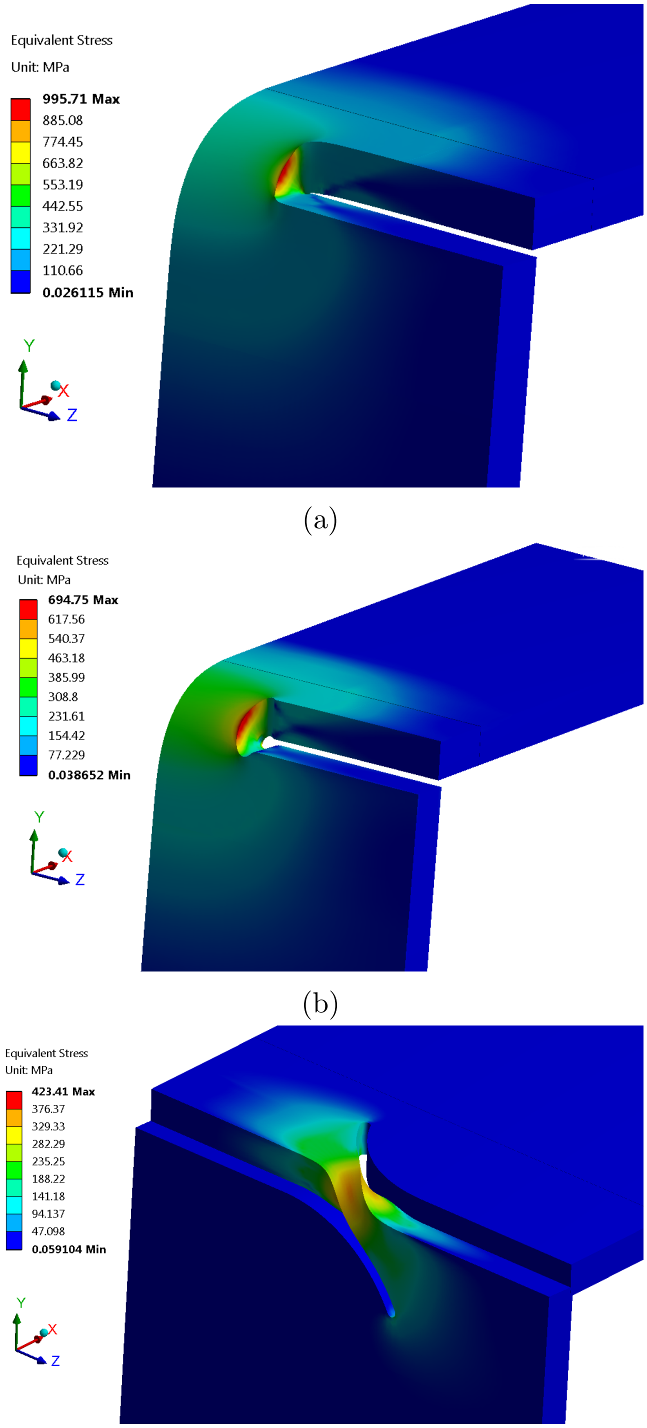

(a)

(b)

(c)

Figure 4.5: The resulted von misses stress along the different MD bend lines, (a) MD-1; (b) MD-2; (c) MD-3.

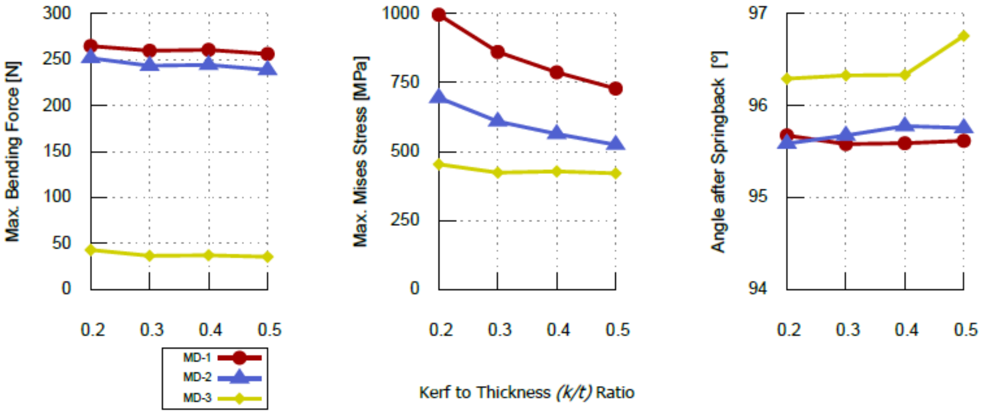

Figure 4.6: Effect of kerf-to-thickness (k/t) ratio

Table 4.3: Effect of kerf-to-thickness (k/t) ratio

Simulation Condition			Results		
MD type	Base values	kerf-to-thickness (k/t) ratio	Bending force (N)	Von Mises stress [MPa]	Angle After springback [°]
MD-1	t=1.628 (mm)	0.2	264.6	995.7	95.67
	w/b=0.28	0.3	259.5	860.7	95.58
	s=3 (mm)	0.4	260.5	786.8	95.59
	g=23 (mm)	0.5	256.0	727.8	95.62
MD-2	R_P=3 (mm)	0.2	251.5	694.8	95.59
		0.3	243.2	608.5	95.67
		0.4	244.2	563.6	95.78
		0.5	238.7	524.3	95.78
MD-3		0.2	42.9	453.3	96.29
		0.3	36.4	423.3	95.33
		0.4	37.1	427.3	96.33
		0.5	35.3	420.9	96.76

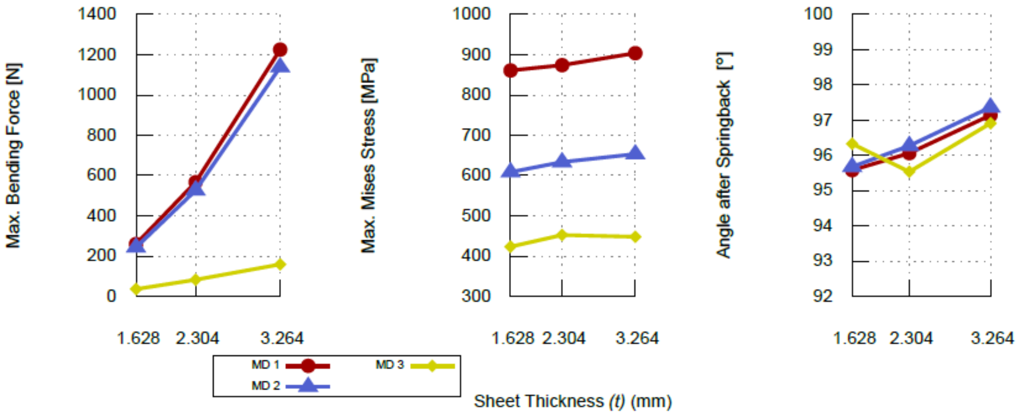

Figure 4.7: Effect of sheet thickness (t)

results show that the thicker sheets require significantly higher bending force as expected. The stress generated along the bend line is slightly increased for thicker sheets for all three MDs. This is apparently associated with patterns each MD has, particularly with the curvature of endings in MD. The springback exhibited a consistently increasing trend in all MD cases, though there is a little fluctuation of springback angle on MD-3. This irregularity might be caused by the rate of change in thickness and shape of MD.

4.6.5 Effect of web-to-width ratio (w/b)

We investigate the web-to-width ratio for three different values for each MD, total of nine cases. The web-to-width ratios are 0.28, 0.4, and 0.52. Figure 4.8 illustrates the results, and Table 4.5 lists the simulation results and conditions. The results show that a larger w/b ratio requires a higher magnitude of bending force. This can be explained by the fact that a larger w/b ratio means a longer web remained after cutting out MD along the sheet width. Hence, a longer web between two neighboring MD obviously generates more resistance to bending. As for the stresses generated, it increased slightly. This implies that a reasonable change in the web dimension does not affect the stress on the bend line. The reasonable change determined by the certain distance between the two ends of MD. This distance should be large enough to prevent interference of stress at one end of MD with stress at another end. Interesting to notice that stresses on MD3 decreases as w/b ratio increases; however, stresses on MD-1 and MD-2 stated constantly. The reason is again related to the shape of MD-3 where larger w/b ratio can allow bending forces to pass through larger web area, which would alleviate the stress concentrations on the web. On the other hand, maximum stresses on MD-1 and MD-2 are located at the end of MDs, thus increasing w/b ratio does not influence stress result. The

Table 4.4: Effect of sheet thickness (t)

Simulation Condition			Results		
MD type	Base values	Changing parameters sheet thickness (t)	Bending force (N)	Von Mises stress [MPa]	Angle After springback [°]
MD-1	k/t=0.3 (mm)	1.628	259.5	860.7	95.58
	w/b=0.28	2.304	566.8	874.1	96.06
	s=3 (mm)	3.264	1225.5	904	97.14
MD-2	g = 23 (mm)	1.628	243.2	608.5	95.67
	R_P=3 (mm)	2.304	526.3	633.5	96.27
		3.264	1138.7	653.3	97.37
MD-3		1.628	36.4	423.4	96.33
		2.304	36.4	452.5	95.54
		3.264	159.1	448.1	96.91

increase in the w/b ratio leads to higher springback angle in the three studied cases of the MD. However, the change in angle magnitude is fairly small with approximately 0.5° increase for MD-1 and MD-2 compared to MD-3. Note that MD-1 and MD-2 behaves similarly. This is because MD-1 and MD-2 have a very similar shape and MD-3 is much different.

4.6.6 Effect of offset distance (s)

To study the effect of the offset distance, this work investigated three offset distances, namely 3 mm, 6 mm, and 9 mm. Fig. 4.9 and Table 4.6 show the effect of different offset distances on OSM bending. The bending force is increased as larger offset distance is used in bending. The increase in bending force is caused by the reduction of the distance between the punch and virtual bending line determined by MD. Hence, a larger force is needed to achieve the same amount of bending moment. No variation in stress is expected for the increase of s. Results show a slight increase of springback angle for all cases, and magnitude of increment is similar for MD-1 and MD-2. This implies again that the shape of the MD plays role in springback.

It is also noted that offset distance (s) increased the tendency of bending with respect to the clamped point (edge of blank holder or support), see Fig. 4.10(a). In order to illustrate the changes in the magnitude of vertical displacement of the sheet with respect to the clamping point, a vertical displacement of the edge is evaluated with different offset distance in Fig. 4.10(b), (c) during the bending step (second

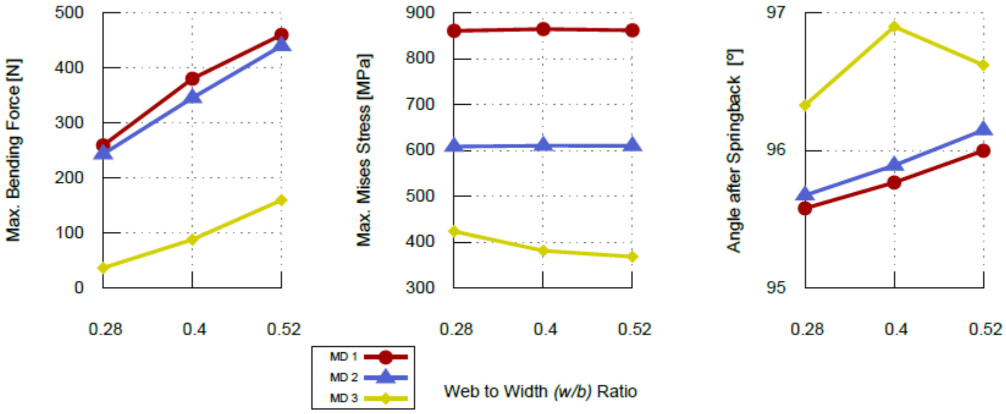

Figure 4.8: Effect of web-to-width ratio (w/b)

Table 4.5: Effect of web-to-width ratio (w/b)

Simulation Condition			Results		
MD type	Base values	Changing parameters web-to-width ratio (w/b)	Bending force (N)	Von Mises stress [MPa]	Angle After springback [°]
MD-1	k/t=0.3 (mm)	0.28	259.5	860.7	95.58
	t=1.628	0.4	380.3	864.5	95.77
	s=3 (mm)	0.52	460.1	862.0	95.99
MD-2	g = 23 (mm)	0.28	243.2	608.5	95.67
	R_P=3 (mm)	0.4	345.5	610.1	95.89
		0.52	440	610.0	96.14
MD-3		0.28	36.4	423.4	96.33
		0.4	87.8	381.2	96.9
		0.52	159.6	368.3	96.62

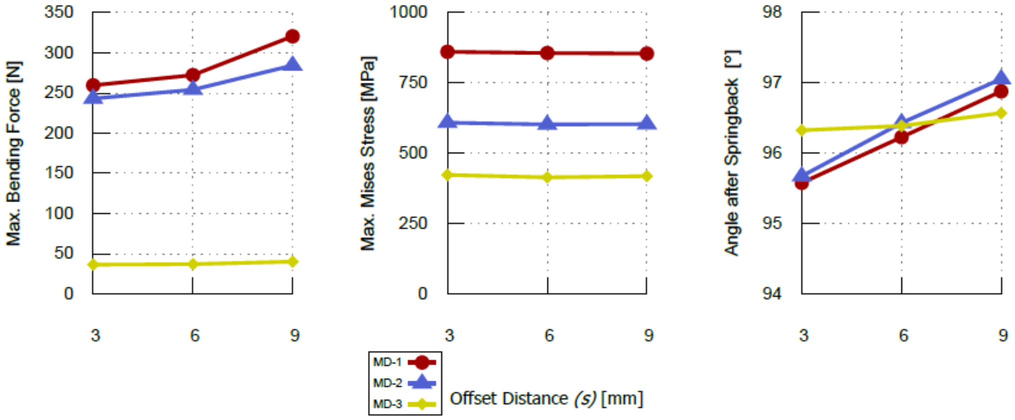

Figure 4.9: Effect of offset distance (s)

load step of simulation). It shows that the displacement magnitude increased as the offset distance is raised to 9 mm. However, it is found that the magnitude of this vertical movement is negligible compared to total displacement happened during bending. Therefore, the tendency to bend with respect to clamping point can be neglected.

4.6.7 Effect of punch placement (g)

This work considers three different scenarios for the effect of placing the punch at various locations, denoted by (g). The distance between the punch and edge of the blank holder (or support) is set to 13 mm, 18 mm, and 23 mm, respectively. All other processing and design parameters are kept at constant baseline values. The results in Fig. 4.11 and Table 4.7 show that required bending force is reduced as the punch placement location (g) increases. This is due to the fact that obtaining the same amount of bending moment requires less amount of bending force when the force arm increases. In addition, the stress level and springback angle in all MD stayed without significant change.

4.6.8 Effect of punch radius (R_P)

This work evaluated three different punch radiuses, denoted by R_P. The values are set to 1 mm, 2 mm, and 3 mm, respectively. The results are shown in Fig. 4.12 and Table 4.8, suggesting that stress stayed at the same level. Bending force and spring back slightly increased with the change in the punch radius. The changes in the bending force magnitude are related to the change in contact area between the punch radius and the sheet during the bending process.

Table 4.6: Effect of offset distance (s)

Simulation Condition			Results		
MD type	Base values	Changing parameters Offset distance (s)	Bending force (N)	Von Mises stress [MPa]	Angle After springback [°]
MD-1	k/t=0.3 (mm)	3	259.5	860.7	95.58
	t=1.628 (mm)	6	272.4	856.4	96.23
	w/b=0.28	9	320.6	854.3	96.88
MD-2	g=23(mm)	3	243.2	608.5	95.67
	R_P=3 (mm)	6	254.0	602.7	96.43
		9	284.3	603.6	97.05
MD-3		3	36.4	423.4	96.33
		6	37.0	414.3	96.39
		9	40.1	418.6	96.57

Table 4.7: Effect of punch placement (g)

Simulation Condition			Results		
MD type	Base values	Changing parameters Offset distance (s)	Bending force (N)	Von Mises stress [MPa]	Angle After springback [°]
MD-1	k/t=0.3 (mm)	23	259.3	861.4	95.56
	t=1.628 (mm)	18	281.3	861.6	95.73
	w/b=0.28	13	342.6	860.7	95.58
MD-2	g=23(mm)	23	243.2	608.5	95.67
	R_P=3 (mm)	18	263.9	607.3	95.72
		13	319.3	609.5	95.86
MD-3		23	36.4	423.4	96.32
		18	40.5	420.0	96.17
		13	52.6	418.7	96.20

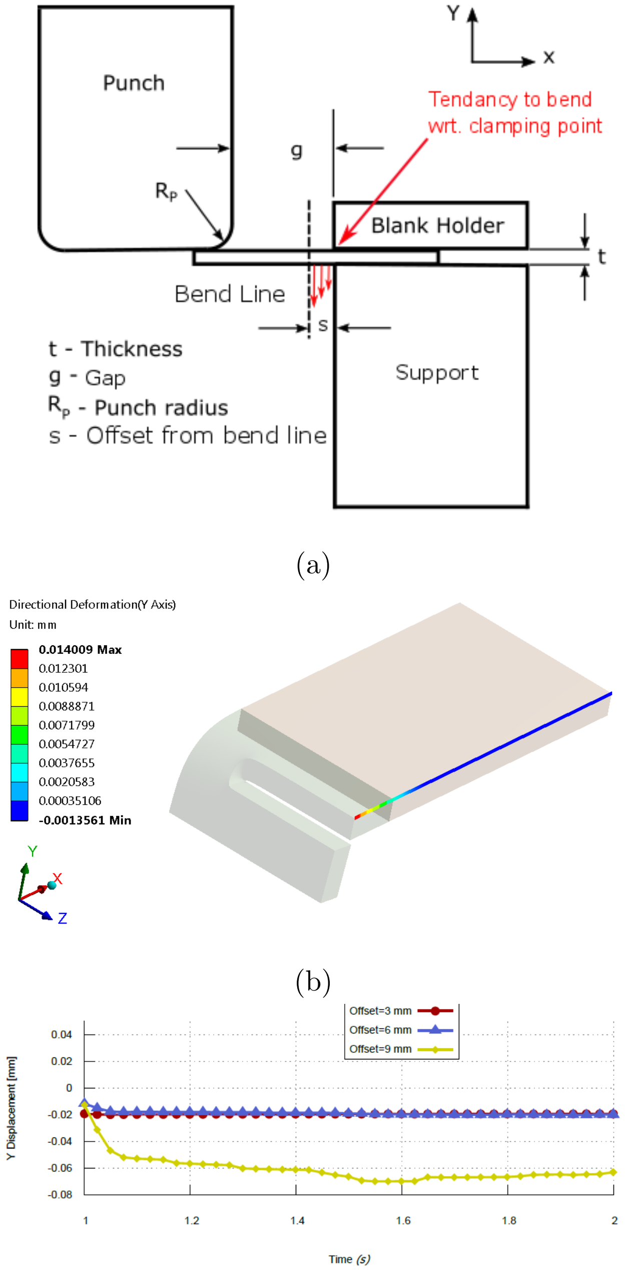

(a)

(b)

(c)

Figure 4.10: Evaluation of tendency to bend with respect to clamping point, (a) the tendency to bend with respect to clamping point of the sheet; (b) Y displacement is evaluated on edge shown. This is the case for MD-1; offset distance is equal to 6 mm; (c) Y displacement of the designated edge in MD-1 is plotted in the bending process (second load step) of the simulation.

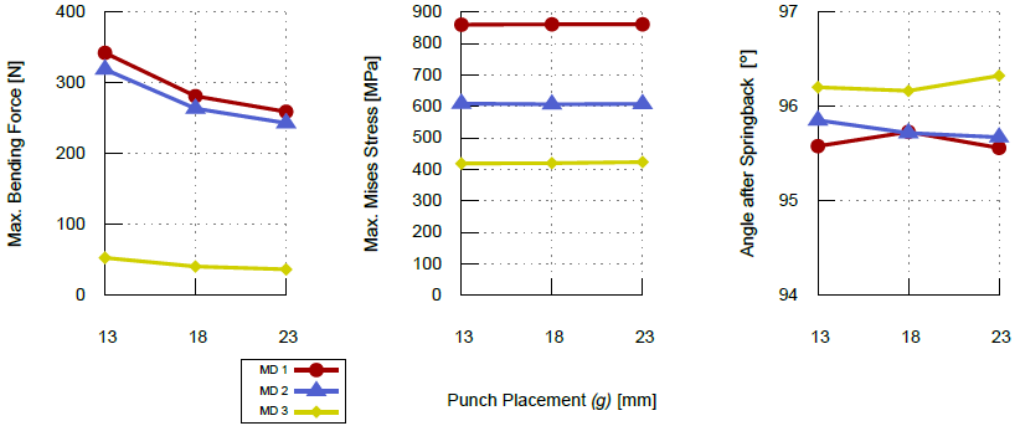

Figure 4.11: Effect of punch placement (g)

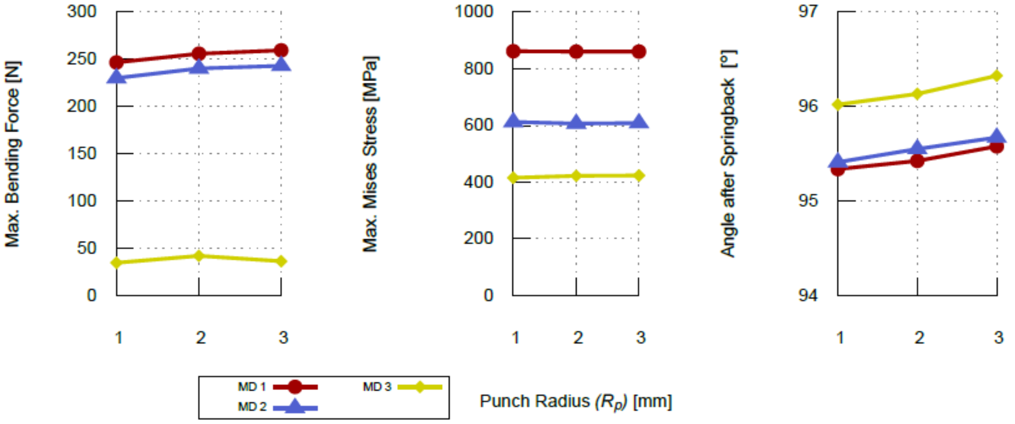

Figure 4.12: Effect of punch radius (R_P)

Table 4.8: Effect of punch radius (R_P)

Simulation Condition			Results		
MD type	Base values	Changing parameters Punch radius (R_P)	Bending force (N)	Von Mises stress [MPa]	Angle After springback [°]
MD-1	k/t=0.3 (mm)	3	259.5	860.7	95.58
	t=1.628 (mm)	2	255.9	860.6	95.42
	w/b=0.28	1	246.7	862.2	95.34
MD-2	s=3(mm)	3	243.2	608.5	95.67
	g=23 (mm)	2	240.4	606.7	95.55
		1	230.1	606.7	95.41
MD-3		3	36.4	423.4	96.33
		2	41.9	422.4	96.13
		1	34.7	415.3	96.02

4.6.9 General recommendation

Based on the discussed results, some general recommendation can be made regarding OSM bending parameters. The stress generated along the bend line is caused by the size of the curvature radius at the end of a specific MD. A lager k/t ratio leads to a greater curvature radius. Hence, a large k/t ratio should be selected in order to have less stress concentration after bending. For achieving reduced bending force, the web-to-width (w/b) ratio and thickness should be kept small as long as the stress level is not affected by it. A smaller offset distance (s) is good for higher accuracy of bending. The punch position (g) in the OSM bending configuration should be as large as possible for decreasing bending force as well as the sliding surface contact between the punch and the blank sheet. However, it should be kept in mind that punch placement (g) should guarantee the contact between the punch radius and the sheet surface. Otherwise, it causes undesired contact between edges of the blank sheet and the punch surface at certain point. As for the punch radius, it has a little effect on OSM bending and proper radius can be selected based on the specific problem.

4.7 Summary

This chapter shows that OSM bending is possible without die. The introduced MD can play the role of a die in a bending process by determining the bending line. Therefore, OSM bending has a significant impact on bending, especially in the mass production settings for sheet metal parts. In order to investigate the effect of OSM parameters, three OSM design parameters and three process parameters are presented in this investigation. The findings indicate each parameter has a different impact on OSM bending. The general recommendation is made on the selection of studied parameters. It is found that shape of MD plays an important role and it is observed that similar MDs exhibit a similar trend, leading to the conclusion that there is a difference in the deformation mode along the bend line caused by the selected shape of the MD.

Chapter 5

FORCE PREDICTION MODEL FOR OSM BENDING PROCESS

5.1 Background

Force prediction during a sheet metal forming process is of crucial importance during the fabrication process. Literature shows various approaches to predict the necessary manufacturing force requirements for sheet metal forming, including bending. The approaches are based on experimental methods, analytical analysis, regression techniques such as response surface method (RSM), or a combination of these techniques.

Wang et al. [118] reported a detailed mathematical force prediction model for the air bending process. The inputs required for the model are the material properties, bending tool dimensions, and bending process parameters. The bending force is one of the four outputs of the model. Zhang et al. [119] presented an analytical model to predict the bending force for plane-strain bending of a metal sheet. The model is very general and can be used for any deformation where both bending and stretching exist.

Marciniak et al. [120] discussed the sheet metal bending process in detail, including load type, springback, and choice of material model. Singh et al. [121] showed an analytic force prediction model for the three-point bending process. The model was refined and exhibited better agreement with an experiment reported in [38]. Boljanovic [22] showcased bending force empirical prediction models for wiping die bending, U-die bending, and air bending. However, the derivation process of these models is not detailed. Narayanasamy et al. [122] reported a method that uses RSM regression to predict the necessary bending force in air bending. The RSM regression model takes five process parameters as inputs. More specifically, the inputs are the punch travel, strain hardening exponent, punch radius, punch velocity, and width of the sheet. Malikov et al. [123] reported a bending force requirement for the air bending process on structured sheet metal. They developed an analytical model to predict the maximum bending force in air bending.

On the other hand, Farsi et al. [75] presented a bending force prediction model for air bending of sheet metal with holes. This model considers the effective width of the sheet, the radius of the hole, and the angle factor as parameters to predict the bending force magnitude. Srinivasan et al. [124] presented a bending force prediction model for air bending by using RSM regression. Inputs to this model include the sheet metal strain-hardening exponent, coating thickness, die opening, die radius, punch radius, punch travel, and punch velocity. The outputs of the model are bending force and bending angle. Chudasama et al. [125–127] developed a mathematical model to predict the maximum bending force in the 3-roller bending process, while Vorko et al. [128–130] presented a bending force prediction model for air bending taking multi-breakage effect during the forming process into account.

The literature reveals that the state-of-the-art still lacks the understanding of the force requirements for sheet metal bending and its correlation to the MD geometry. The ability to correctly predict the required force to bend a sheet with a certain thickness and MD features enables the successful implementation of this manufacturing technique. It can also reveal the operation limits of the OSM bending tool. In addition, estimating the bending force is necessary for design consideration and safety concerns during the fabrication.

In the literature presented above, the bending force is predicted using a traditional punch-die bending configuration in addition to using a sheet with continuous material, i.e., without MDs. However, in OSM bending analysis, the introduction of MDs and the new bending setup without the punch-die configuration can alter the bending force requirements [76, 131]. Therefore, further investigations need to be carried out to estimate the bending force in the OSM bending process. These investigations need to consider the parameters of the MDs and the OSM bending process factors such as the offset distance, sheet thickness, and punch placement.

The objective of this chapter is to present a prediction model for OSM bending force that can assist the evaluation of manufacturing needs for certain sheet metal thickness and a specific MD design. The bending force can be a function of the mechanical properties of the sheet, the geometrical configuration of the bending setup, and features of the MDs.

5.2 Modeling of bending force

This section develops a prediction model to estimate the force requirements for OSM bending by combining information from an analytical analysis and experimental data. The procedure to obtain the prediction model is as following: 1) an analytical force analysis is performed on a sheet assuming no MD is applied. Bending force is derived with moment equilibrium condition on a cross-section of the sheet placed in the OSM bending setup. 2) OSM bending experiment is conducted to measure the bending force under combinations of different bending configuration and parameters. The goal is to collect bending force measurement data for regression analysis, in addition to identifying which parameters influence the bending force significantly. 3) A regression model is purposed to find OSM bending force, which

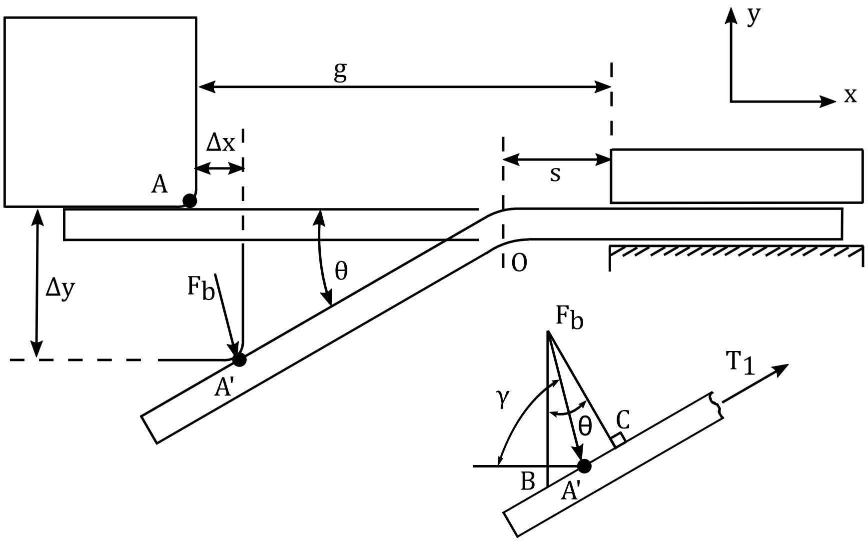

Figure 5.1: Forces on a cross-section parallel to the X-Y plane

considers OSM bending parameters that were identified as significant using the experimental data. The purposed OSM bending force formulation contains variables corresponding to MD parameters, material properties, OSM bending configuration, and regression coefficients. The OSM bending force measurement during the experiment is divided into two sets. One set is used to determine the regression coefficients, and the other set is used to validate the OSM bending force prediction model.

5.2.1 Analytical force analysis

For the analytical force analysis, the OSM bending force is derived using moment equilibrium applied on a sheet with no MDs in an OSM bending configuration. Under these conditions, a cross-section of the sheet parallel to the XY plane is selected, as shown in Fig. 5.1. A general bending state where the sheet is bent to an angle θ is considered and a segment of the sheet cross-section is analyzed. The free-body diagram of the analyzed section of the sheet is illustrated in Fig. 5.1.

Initially, the punch contacts the blank at point A, while the punch is positioned at a distance g from the blank holder (or support). The bending line indicated with a dashed line is crossing point O and has an offset distance s from the blank holder and support. At the final bending stage, when the sheet is bent to an angle of θ, the punch is in contact with the sheet at point A'. Up to this stage, the punch has traveled Δx, Δy along the positive X-axis and negative Y-axis, respectively. The magnitude of the bending force exerted by the punch on the blank at point A' is equal to F_b , at an angle of γ from the X-axis.

The following assumptions are made during the analysis: (a) During bending, the sheet material is assumed to undergo isotropic hardening. Therefore, the yield surface keeps its shape but expands uniformly with increasing stress. The nonlinearity of the sheet material obeys the Von Mises criterion and associated flow rule; (b) The sheet is sufficiently wide in the dimension along the Z-axis, which is perpendicular to the sheet cross-section shown in Fig. 5.1. Hence, the change in the width can be neglected, which implies plane-strain condition; (c) The stress component normal to sheet surface is zero, i.e., the plane stress condition holds; (d) The stress-strain characteristics of the sheet material are the same in tension and compression; (e) The neutral axis is always in the middle of the sheet thickness. The cross-section plain remains plane and normal to the neutral axis during bending; (f) The sheet does not undergo any thinning; hence the thickness remains constant during the bending; (h) Bauschinger effect is not considered.

Under the assumptions above, the OSM bending process occurs under deformation mode with plane strain $[\epsilon_1; \epsilon_2 = \beta\epsilon_1 = 0; \epsilon_3 = -(1+\beta)\epsilon_1]$ and plain strain $[\sigma_1; \sigma = \alpha\sigma_1 = \frac{1}{2}\sigma_1; \sigma_3 = 0]$ where the subscript 1, 2, 3 denote principle directions, α and β are stress ratio and strain ratio, respectively.

The values of stress ratio and strain ratio are $\alpha = \frac{1}{2}$, $\beta = 0$ under plane strain and plane stress condition. Thus, the equivalent strain, $\bar{\epsilon}$, can be written as in Eq. (5.1),

$$\bar{\epsilon} = \sqrt{\frac{4}{3}(1+\beta+\beta^2)\epsilon_1} = \frac{2}{\sqrt{3}}\epsilon_1. \tag{5.1}$$

For the analysis, the Von Mises yield criteria, which relates the flow stress, σ_f, and equivalent stress, $\bar{\sigma}$, takes the form as in Eq. (5.2)

Von Mises yield criteria,

$$\sqrt{\frac{1}{2}[(\sigma_1-\sigma_2)^2 + (\sigma_2-\sigma_1)^2 + (\sigma_3-\sigma_1)^2]} = \sigma_f = \bar{\sigma}, \tag{5.2}$$

Under plane stress condition where the principal stresses are $\sigma_1 \neq 0$, $\sigma_2 = \alpha\sigma_1$, $\sigma_3 = 0$, $\alpha = \frac{1}{2}$, Eq. (5.2) can be simplified to Eq. (5.3),

$$\bar{\sigma} = \sqrt{(1-\alpha+\alpha^2)}\sigma_1 = \frac{\sqrt{3}}{2}\sigma_1, \tag{5.3}$$

which then can be written as

$$\sigma_1 = \frac{2}{\sqrt{3}}\bar{\sigma}. \tag{5.4}$$

The sheet material is assumed to follow the power-law work hardening as in Eq. (5.5), where K is the strength coefficient, and n is strain hardening exponent of a material.

$$\bar{\sigma} = K\bar{\epsilon}^n \tag{5.5}$$

Equivalent stress on the sheet can be obtained by substituting Eq. (5.1) into Eq. (5.5) to yield Eq. (5.6)

$$\bar{\sigma} = K(\frac{2}{\sqrt{3}}\epsilon_1)^n. \tag{5.6}$$

The internal moment generated on the sheet is given in Eq. (7) [120],

$$M_{internal} = \int_{-\frac{t}{2}}^{\frac{t}{2}} \sigma_1 y dy, \tag{5.7}$$

where y is the distance from the neutral axis to a strip of sheet thickness dy, and $\sigma_1 \times dy \times 1$ is the tension force acting on the strip of the sheet with unit width.

By substituting Eq. (5.4), and Eq. (5.6) into Eq. (5.7) and simplifying the equation, the internal moment can be expressed as in Eq. (5.8),

$$M_{internal} = 2K(\frac{2}{\sqrt{3}})^{(n+1)} \int_{0}^{\frac{t}{2}} \epsilon_1^n y dy. \tag{5.8}$$

Assuming principal strain $\epsilon_1 \approx \frac{y}{\rho}$, where ρ is the radius of curvature and $y = \frac{t}{2}$, Eq. (5.8) can be expressed as in Eq. (5.9),

$$M_{internal} = K(\frac{1}{\sqrt{3}})^{(n+1)}(\frac{1}{\rho})^n \frac{t^{(n+2)}}{n+2}. \tag{5.9}$$

To obtain the external moment generated by the punch on the sheet, we analyze the moment of bending force, F_b, about point O as expressed in Eq. (5.10),

$$M_{external} = F_b sin(\gamma)(g - s - \Delta x) + F_b cos(\gamma)\Delta y. \tag{5.10}$$

Based on the trigonometry relationship given in Eq. (5.11), Eq. (5.10) can be expressed as in Eq. (5.12),

$$\Delta y = sin(\theta)\sqrt{(g - s - \Delta x)^2 + (\Delta y)^2}, \tag{5.11}$$

$$M_{external} = F_b sin(\gamma)(g - s - \Delta x) + F_b cos(\gamma) sin(\theta)\sqrt{(g - s - \Delta x)^2 + (\Delta y)^2}. \tag{5.12}$$

Based on moment equilibrium condition, equating the internal moment in Eq. (5.9) to the external moment in Eq. (5.12) will result in Eq. (5.13),

$$\begin{aligned}&K(\tfrac{1}{\sqrt{3}})^{(n+1)}(\tfrac{1}{\rho})^{n}\tfrac{t^{(n+2)}}{n+2} = \\ &F_b sin(\gamma)(g-s-\Delta x) + F_b cos(\gamma) sin(\theta)\sqrt{(g-s-\Delta x)^2+(\Delta y)^2}.\end{aligned} \tag{5.13}$$

Solving Eq. (5.13) for F_b, we obtain the bending force acting on the sheet as in Eq. (5.14).

$$\begin{aligned}&F_b = \\ &K(\tfrac{1}{\sqrt{3}})^{(n+1)}(\tfrac{1}{\rho})^{n}\tfrac{t^{(n+2)}}{n+2}\tfrac{1}{sin(\gamma)(g-s-\Delta x)+cos(\gamma)sin(\theta)\sqrt{(g-s-\Delta x)^2+(\Delta y)^2}}.\end{aligned} \tag{5.14}$$

Assuming the radius of curvature is small in OSM bending and is equal to the sheet thickness, t. Eq. (5.14) can be expressed as in Eq. (5.15)

$$\begin{aligned}&F_b = \\ &K(\tfrac{1}{\sqrt{3}})^{(n+1)}\tfrac{t^{(n+2)}}{n+2}\tfrac{1}{sin(\gamma)(g-s-\Delta x)+cos(\gamma)sin(\theta)\sqrt{(g-s-\Delta x)^2+(\Delta y)^2}}.\end{aligned} \tag{5.15}$$

Eq. (5.15) is the concluded analytical form of bending force required for a sheet without MDs to bend the sheet with an angle of θ using the OSM bending setup.

5.3 OSM bending experiment

5.3.1 Experimental setup

An experiment is designed to measure the OSM bending force magnitude required to bend a sheet with MD. During the experiment, the needed force to bend the sheet from a flat state to 90° was continuously measured. The CNC machining center–DMG Mori NMV1500 shown in Fig. 5.2–is used to achieve OSM bending. The CNC controlled relative motion between the punch and sheet. Two fixtures are designed to hold the sheet and the punch. One fixture is mounted on the CNC spindle to hold the sheet. The other fixture is installed on a Kistler three-component dynamometer to hold the punch. The dynamometer is screwed on the CNC bed. During the bending process, the CNC spindle controls the motion of the sheet. As a result, the sheet moves against the punch, which is the opposite of the schematic shown in Fig. 1.2. The experiment is set up in this way due to the impracticality of installing the dynamometer on the spindle. However, the current experiment setup still provides the same force measurement because the relative motion between the punch and the OSM specimen does not change. To collect data from the Kistler Type 9257B Dynamometer, a Yokogawa SL-1000 data acquisition unit is used to collect three voltage signals – one for each of the orthogonal directions. The voltage readings can then be converted to force (in Newtons).

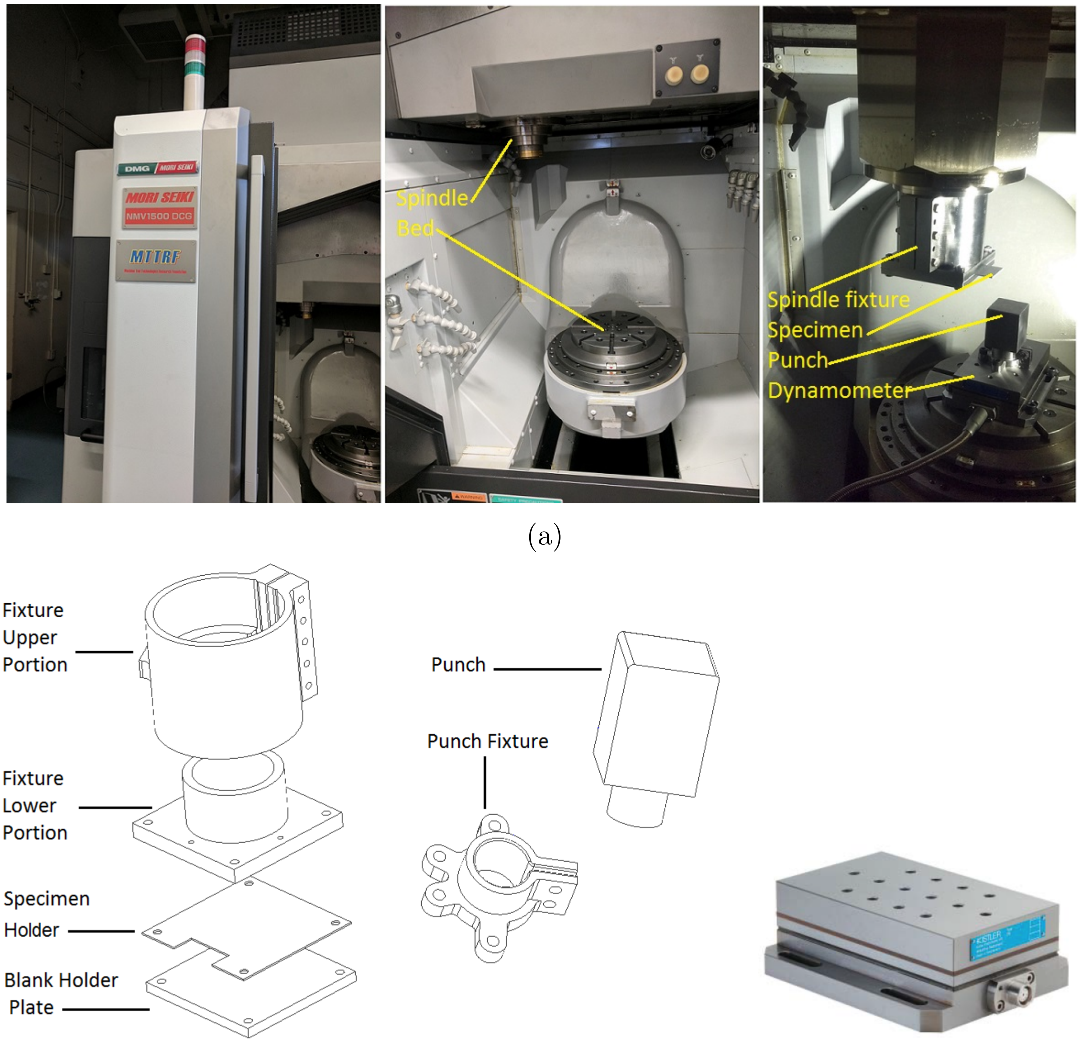

(a)

(b)

(c)

Figure 5.2: OSM bending experiment CNC setup, (a) CNC machining center and realization of OSM bending process; (b) Details of the spindle and punch fixtures; (c) Kistler three-component dynamometer type 9295B used to measure bending force

The experiment is performed on three different configurations of MDs. MD-1, MD-2, and MD-3 are shown in Fig. 4.2. These three MDs are studied since they are the bases for other MDs. The used sheet material for the samples is aluminum alloy 6061-O temper. To fabricate the MDs, a micro waterjet cutting with a tolerance of ±0.025 (mm) was used. The sheet specimen dimensions are 50 (mm) × 50 (mm) in length and width, respectively. MDs were applied in the middle of the sheet, as shown in Fig. 4.2. There are three different thicknesses for the sheet specimens. To achieve precise bending, the thickness of the sheet before the experiment is measured. The measured thicknesses were 1.548 (mm), 2.228 (mm), and 3.192 (mm), respectively.

5.3.2 Experimental plan

In chapter 4, we identified the significant parameters that influence the OSM bending process. It is found that OSM bending force is influenced by an offset distance (s), punch placement (g), web-to-width ratio (w/b), and sheet thickness (t). In this chapter, these parameters are taken into consideration during the OSM bending force formulation.

Table 4.1. lists investigated parameters, baseline value, and a full list of the investigated values for each parameter. In this experiment, only one parameter is changed at a time while keeping all others at the baseline value. Thus, 42 different cases (i.e., samples) were considered. Each case is tested with three repetitions; thus 126 experiment runs are performed. Table 5.1 lists the 42 cases with each associated OSM parameter, while the changed parameters are indicated by bold font.

Table 5.1: The details of each conducted experiment case with the assigned parameters. In total 42 cases were experimented with three repetitions for each case.

Case No.	Name	k/t	s [mm]	g [mm]	R_p [mm]	t [mm]	w/b
1	MD-1-k-t-0.2	**0.2**	3	23	3	1.548	0.28
2	MD-1-k-t-0.3	**0.3**	3	23	3	1.548	0.28
3	MD-1-k-t-0.4	**0.4**	3	23	3	1.548	0.28
4	MD-1-k-t-0.5	**0.5**	3	23	3	1.548	0.28
5	MD-2-k-t-0.2	**0.2**	3	23	3	1.548	0.28
6	MD-2-k-t-0.3	**0.3**	3	23	3	1.548	0.28
7	MD-2-k-t-0.4	**0.4**	3	23	3	1.548	0.28
8	MD-2-k-t-0.5	**0.5**	3	23	3	1.548	0.28
9	MD-3-k-t-0.2	**0.2**	3	23	3	1.548	0.28
10	MD-3-k-t-0.3	**0.3**	3	23	3	1.548	0.28

11	MD-3-*k*-*t*-0.4	**0.4**	3	23	3	1.548	0.28
12	MD-3-*k*-*t*-0.5	**0.5**	3	23	3	1.548	0.28
13	MD-1-offset-6	0.3	**6**	23	3	1.548	0.28
14	MD-1-offset-9	0.3	**9**	23	3	1.548	0.28
15	MD-2-offset-6	0.3	**6**	23	3	1.548	0.28
16	MD-2-offset-9	0.3	**9**	23	3	1.548	0.28
17	MD-3-offset-6	0.3	**6**	23	3	1.548	0.28
18	MD-3-offset-9	0.3	**9**	23	3	1.548	0.28
19	MD-1-punch-place-13	0.3	3	**13**	3	1.548	0.28
20	MD-1-punch-place-18	0.3	3	**18**	3	1.548	0.28
21	MD-2-punch-place-13	0.3	3	**13**	3	1.548	0.28
22	MD-2-punch-place-18	0.3	3	**18**	3	1.548	0.28
23	MD-3-punch-place-13	0.3	3	**13**	3	1.548	0.28
24	MD-3-punch-place-18	0.3	3	**18**	3	1.548	0.28
25	MD-1-punch-radi-1	0.3	3	23	**1**	1.548	0.28
26	MD-1-punch-radi-2	0.3	3	23	**2**	1.548	0.28
27	MD-2-punch-radi-1	0.3	3	23	**1**	1.548	0.28
28	MD-2-punch-radi-2	0.3	3	23	**2**	1.548	0.28
29	MD-3-punch-radi-1	0.3	3	23	**1**	1.548	0.28
30	MD-3-punch-radi-2	0.3	3	23	**2**	1.548	0.28
31	MD-1-thickness-2.288	0.3	3	23	3	**2.288**	0.28
32	MD-1-thickness-3.192	0.3	3	23	3	**3.192**	0.28
33	MD-2-thickness-2.288	0.3	3	23	3	**2.288**	0.28
34	MD-2-thickness-3.192	0.3	3	23	3	**3.192**	0.28
35	MD-3-thickness-2.288	0.3	3	23	3	**2.288**	0.28
36	MD-3-thickness-3.192	0.3	3	23	3	**3.192**	0.28
37	MD-1-*w*-*b*-0.4	0.3	3	23	3	1.548	**0.4**
38	MD-1-*w*-*b*-0.52	0.3	3	23	3	1.548	**0.52**
39	MD-2-*w*-*b*-0.4	0.3	3	23	3	1.548	**0.4**
40	MD-2-*w*-*b*-0.52	0.3	3	23	3	1.548	**0.52**
41	MD-3-*w*-*b*-0.4	0.3	3	23	3	1.548	**0.4**
42	MD-3-*w*-*b*-0.52	0.3	3	23	3	1.548	**0.52**

The parameters considered are the kerf-to-thickness ratio (k/t), the thickness of the sheet (t) and the web-to-width ratio (w/b), punch placement (g), punch radius

(R_p) and offset distance from the bending line (s). These parameters are illustrated in Fig. 1.2 and Fig. 4.1 and further explained below for the convenience:

- The thickness of the sheet (t): it refers to the thickness of the sheet material used.
- Kerf-to-thickness ratio (k/t): it is the ratio between the kerf (k) and the sheet thickness (t). Kerf is the cutting width that the laser or water jet cut out of the sheet.
- Web-to-width ratio (w/b): the ratio between the web (w) and the width of the sheet (b). web (w) is defined as the remaining distance between two consecutive MDs after the removal of the material along the bend line to create MD. It is the section that connects neighboring MD along the bend line. The length of the web is measured along the bend line.
- Punch placement (g): the distance between the blank holder and punch.
- Punch radius (R_p): the radius of punch at the region that stays in contact with the sheet.
- Offset distance (s): it is the distance between the imaginary (predetermined) bend line determined by MD and the edge of the blank holder (or support).

5.3.3 OSM bending experiment results

The measurement data of the OSM bending force is plotted against the bending angle. The results are shown in Fig. 5.3-Fig. 5.8. The force magnitude represents an averaged force from three repetitions of the same experiment case listed in Table 5.1. The individual OSM bending force curves are compared to evaluate the repeatability of the experiment before the average is calculated from the three repetitions. Good repeatability, as shown in Fig. 5.9 has been observed for all cases. In Fig. 5.9, the three repetitions for one case are labeled with the full name of the case in addition to letters A, B, and C. The comparison among the replications A, B, and C indicates the excellent repeatability of the experimental measurement.

The experiment confirms that the magnitude of OSM bending force is affected by the sheet thickness (t), web-to-width (w/b) ratio, offset distance (s), and punch placement (g) as in Chapter 4. The remaining two parameters–punch radius (R_p) and kerf-to-thickness ratio (k/t)–have shown little effect on OSM bending force. Hence, in the final formulation of OSM bending force, kerf-to-thickness ratio (k/t) and punch radius (R_p) are excluded.

Further, Eq. (5.15)—the analytical bending force for a sheet without MD—already includes the impact of these three parameters. These parameters are the punch placement (g), offset distance (s), and the sheet thickness (t). The mechanics of

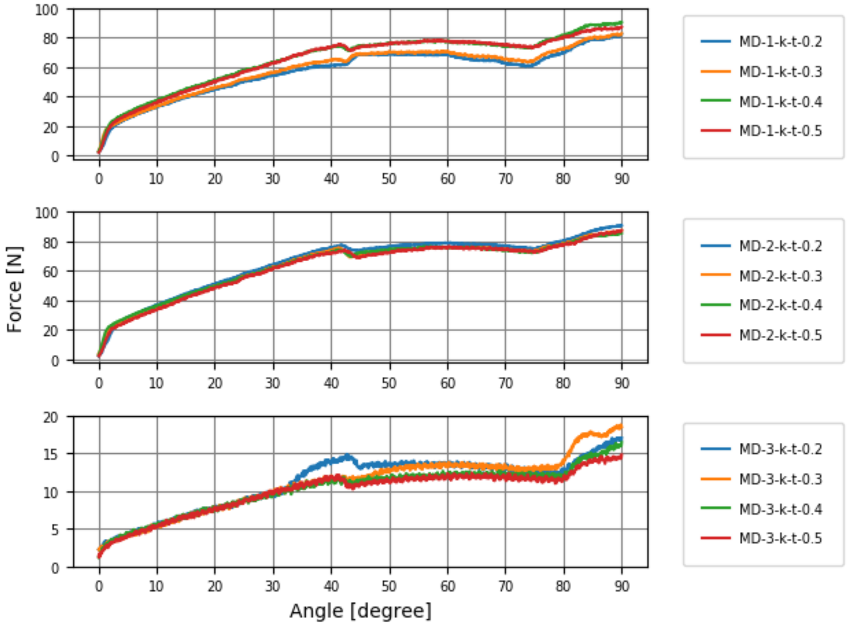

Figure 5.3: Kerf-to-thickness (k/t) ratio impact on OSM bending force per MD type.

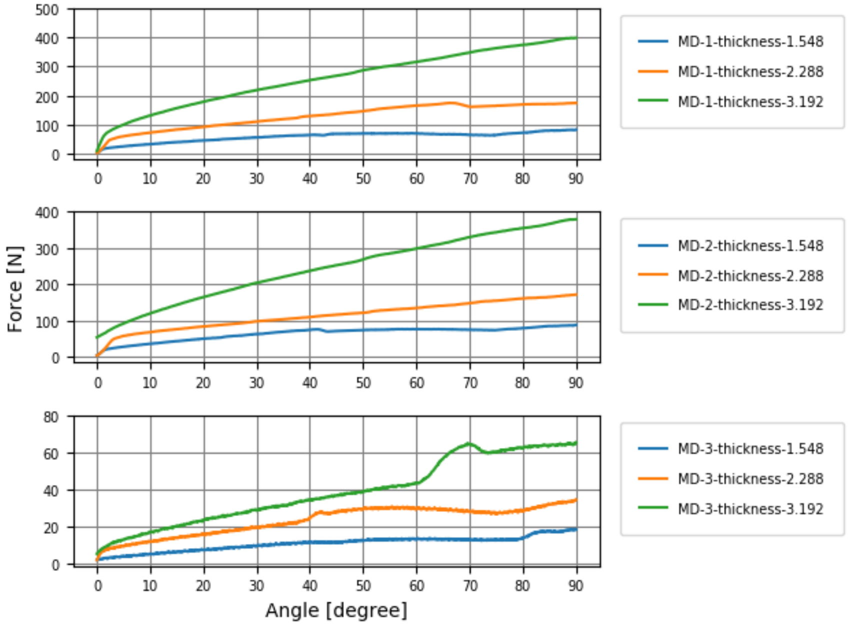

Figure 5.4: The impact of sheet thickness (t) on OSM bending force per MD type

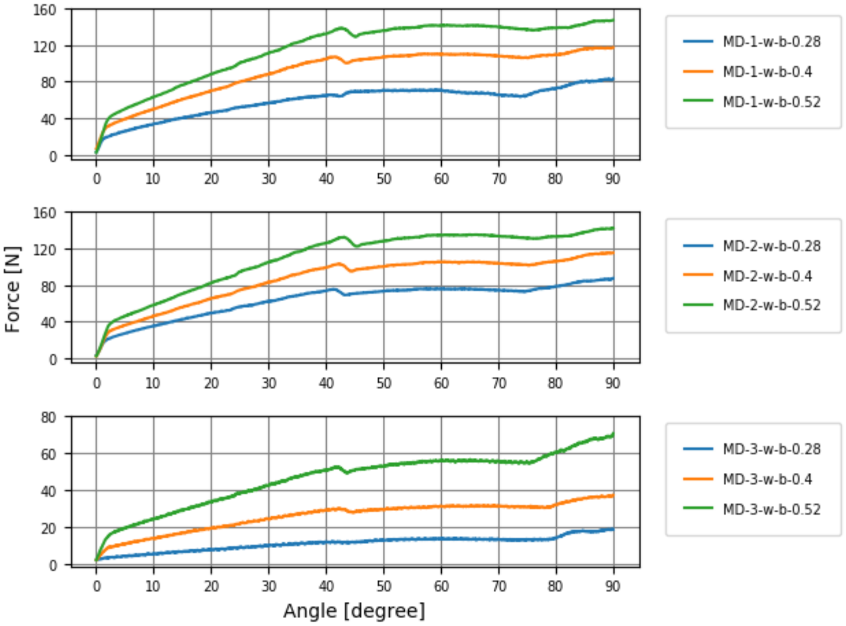

Figure 5.5: Impact of web-to-width (w/b) ratio on OSM bending force per MD type

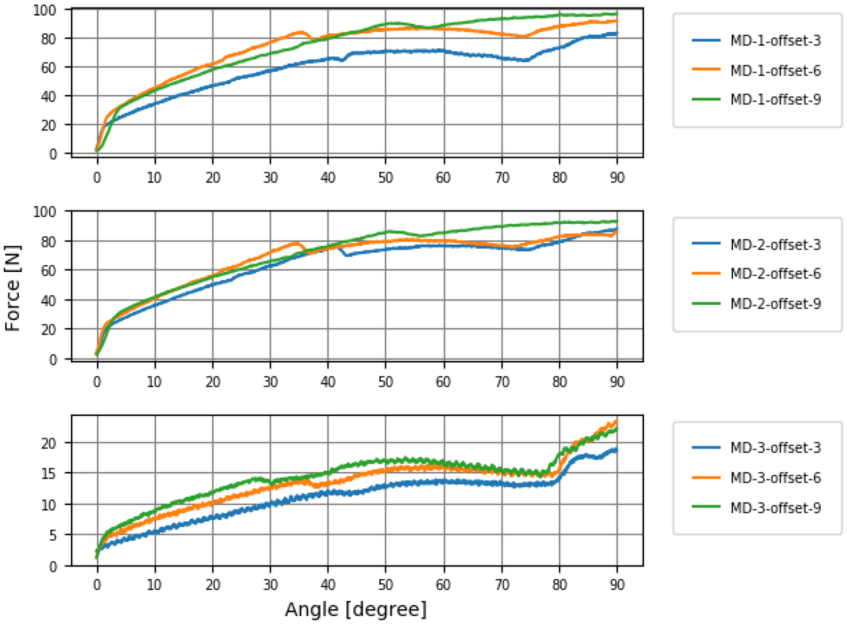

Figure 5.6: The impact of offset distance (s) on OSM bending force per MD type

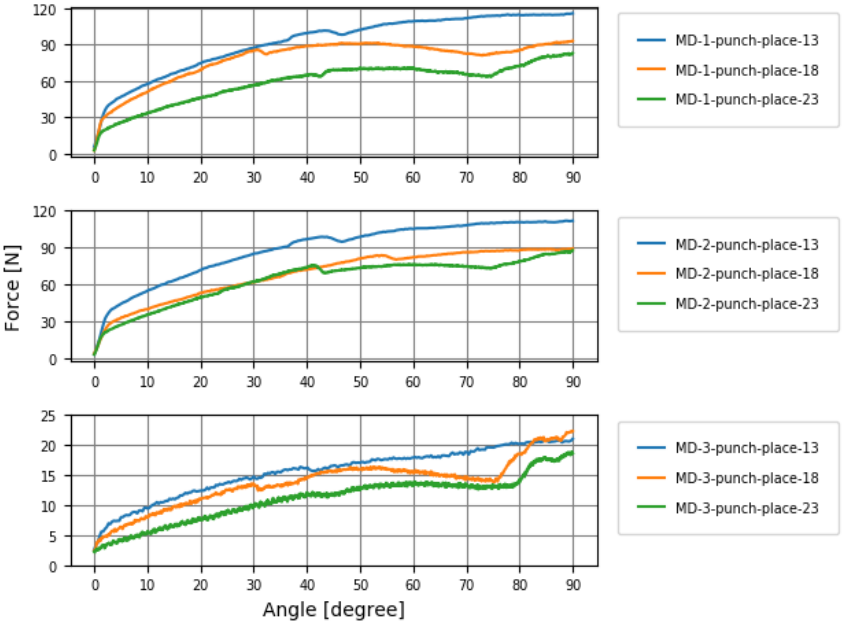

Figure 5.7: The impact of punch placement (g) on OSM bending force per MD type

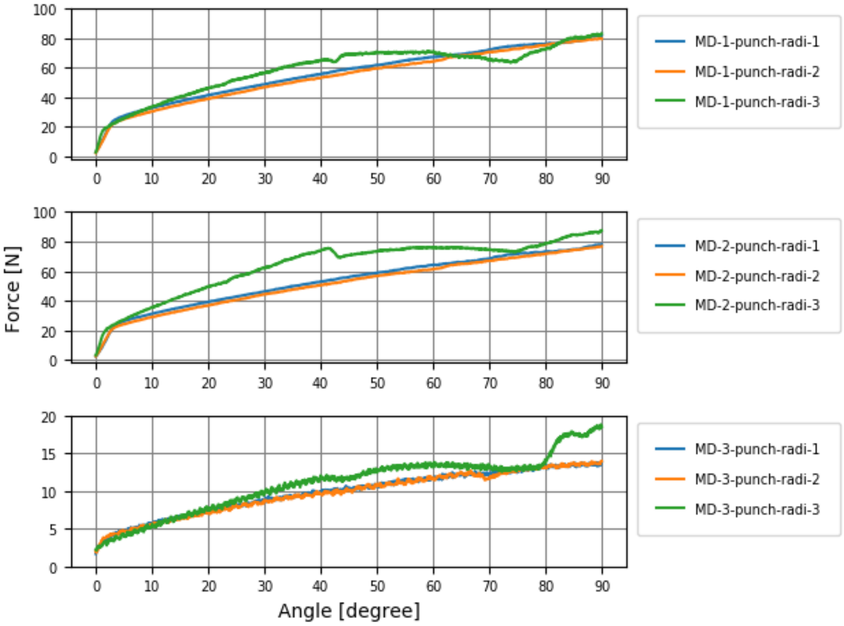

Figure 5.8: The impact of punch radius (R_p) on OSM bending force per MD type

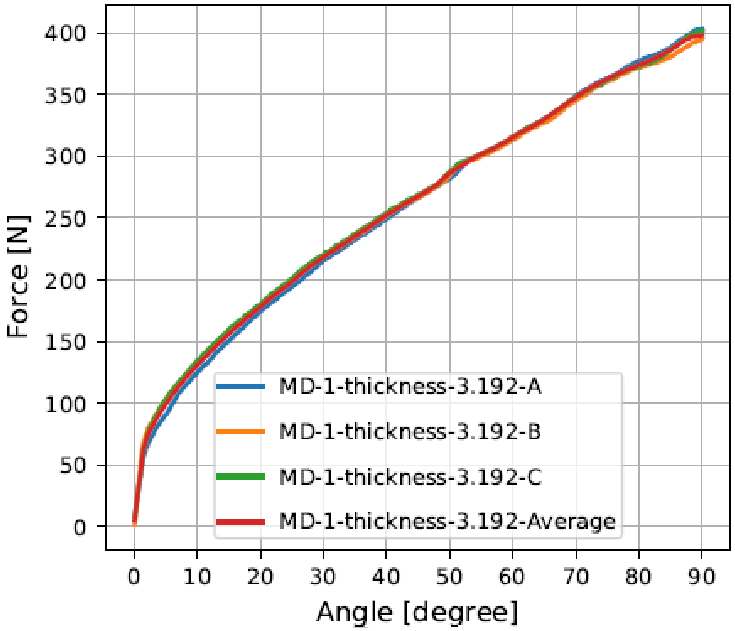

Figure 5.9: Repeatability of experiment

the bending operation suggest that the bending angle theta (θ), the web-to-width ratio (w/b), and the MD type have an influence on the magnitude of OSM bending force. Therefore, these parameters must be incorporated in the final form of the OSM bending force prediction model. Consequently, the final OSM bending force, F, is a function of F_b as listed in Eq. (5.15), bending angle theta (θ), web-to-with ratio (w/b), and MD type as listed in Eq. (5.16),

$$F = f(F_b, \theta, w/b, MD). \tag{5.16}$$

5.3.4 OSM bending force formulation through regression

To find the explicit form of OSM bending force F in Eq. (5.16), the function form is shown in Eq. (5.17) is proposed.

$$F = c_1 F_b^{c_2} sin(\theta)^{c_3} w_e^{c_4}. \tag{5.17}$$

In Eq. (5.17), θ is bending angle, w_e is the effective width of the sheet along the bending line after applying MD. w_e is equal to b, the width of the sheet, multiplying web-to-width-ratio, w/b. Except for MD type, each independent variable in Eq. (5.16) is correlated to OSM bending force, F, through an exponential function. MD type is considered as a categorical variable in the regression process, and it represents the shape factor of each MD. Constants c_1, c_2, c_3, c_4 are the coefficients that need to be determined through regression.

To obtain the constants in Eq. (5.17) and validate Eq. (5.17), the OSM bending force measured data is divided into two sets. One set is made of 34 cases and used to find the constants in Eq. (5.17). The remaining eight cases constitute the validation set. The experiment cases are numbered from 1 to 42, starting from the top of Table 5.1. The validation set includes case No. 4, 8, 12, 14, 21, 29, 32, 40 listed in Table 5.1. These eight-cases in the validation set are selected in such a way that they represent the variance of MD type and all six different parameters considered in the experiment.

In the regression process, 50 equal-distanced data points—consisting of bending angle and force magnitude—are extracted from each experiment case measurement Thus, the extracted data points represent the full range of the OSM bending process from 0° to 90°.

The regression process is carried out in MATLAB using the built-in regression function "fitlm". The nonlinear Eq. (5.17) is linearized by taking the natural logarithm, as shown in Eq. (5.18),

$$lnF = lnc_1 + c_2 lnF_b + c_3 lnsin(\theta) + c_4 ln(w_e). \tag{5.18}$$

In addition, the type of MD is given as a categorical variable in "fitlm" function. The regression yields the following coefficients, c_1=0.6, c_2=0.93817, c_3=0.4392, $c_4 = 1.1368$ for MD-1. The coefficient c_1 is a shape factor that changes as the MD type changes. Thus, the value of c_1 for MD-2 and MD-3 are identified to be 0.591 and 0.107, respectively. Therefore, the regression provided three equations representing each MD, respectively.

The final form of the OSM bending force equation can be written as presented in Eq. (5.19)

$$F = \begin{cases} 0.6F_b^{0.93817} sin(\theta)^{0.4392} w_e^{1.1368}, & for MD-1 \\ 0.591F_b^{0.93817} sin(\theta)^{0.4392} w_e^{1.1368}, & for MD-2 \\ 0.107F_b^{0.93817} sin(\theta)^{0.4392} w_e^{1.1368}, & for MD-3 \end{cases} \tag{5.19}$$

Eq. (5.19) provided a calculation for each MD type. It should be noted that only coefficient c_1 is different when MD type alters, which shows that c_1 is a shape factor that represents the topology of the MD. The underlying reason why the three MD has a different value for c_1 can be explained by the topology of each respective MD pattern and the amount of material removed by the MD. The topology of MD-2 differs from MD-1 only at the end of MD-2 where there is an enlarged opening. Due to this opening, MD-2 has more material removed around the bending line, which leads to slightly less material resisting bending. Hence, the bending force needed for bending MD-2 is marginally less than that of MD-1. As for MD-3, the curved cuts

Table 5.2: Regression statistics

Coefficients	Estimated	Standard Error	tStar	pValue
Intercept (lnc_1)	-0.050945	0.060187	-8.4644	$5.4923e-17$
c_2	0.93817	0.0088213	106.35	0
c_3	0.4392	0.0028305	155.17	0
c_4	1.1368	0.019313	58.863	0

that span away from the bending line towards the two sides of the sheet resulted in more material removal around the bending line compared to both MD-1 and MD-2. In addition, the topology of MD-3 pattern has changed the transmission path of external force from one half of the specimen to the other. Hence, the bending force magnitude is much less compared to MD-1 and MD-2.

Eq. (5.19) indicates that the coefficient c_1 is the only factor that can change the magnitude of OSM bending force, provided that the material type, the effective length, and the bending angle remain the same. This implies that only coefficient c_1 needs to be identified for Eq. (5.19) to be extended to other MDs configurations. The identification of c_1 for other MDs using effective mathematical, statistical, or numerical methods is in our future research plan.

The adequacy of the proposed model is judged based on the regression statistics in Table 5.2 and the analysis of variances (ANOVA) presented in Table 5.3. R-squared and Adjusted R-Squared, which is desired to be close to 1, are both equal to 0.983. This implies the model can explain almost all of the response variable variation. The pValue for each parameter is under the 0-5% significance level standard, which indicates that the response variables selected are statistically significant and it is meaningful to include them in the proposed model. In the next section, the purposed model is validated using the validation set of experimental measurements.

5.4 Validation

The proposed model presented in Eq. (5.19) is validated against the validation set of the force measurement that consists of eight experiment cases. These eight cases are not used in the regression analysis. Similar to the regression process, 50 data points of force-angle pairs are extracted from each of these eight cases for comparison. The regression model in Eq. (5.19) predicts OSM bending force values at the derived 50 angles by substituting the coefficients c_1, c_2, c_3, c_4. The prediction results are plotted and compared to the experimental measurements in Fig. 5.10-Fig 5.17.

Table 5.3: ANOVA statistics

Coefficients	Sum Square	Degree of Freedom	Mean Square	F	pValue
c_2	193.25	1	193.25	11311	0.00
c_3	411.35	1	411.35	24077	0.00
c_4	59.196	1	59.196	3464.8	0.00
MD	1120.9	1	560.44	32803	0.00
$Error$	28.942	1694	0.017085	—	—

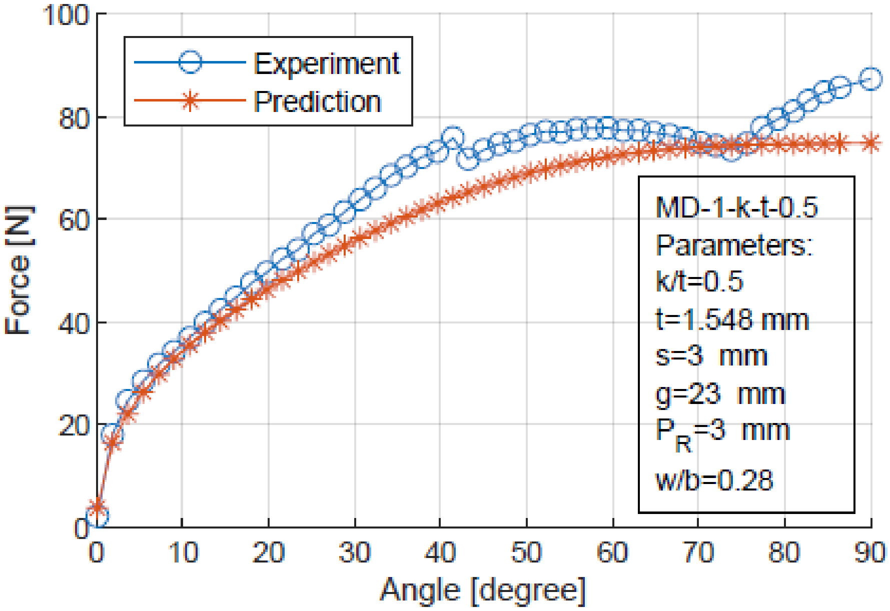

Figure 5.10: Validation of OSM bending force: case MD-1-k-t-0.5

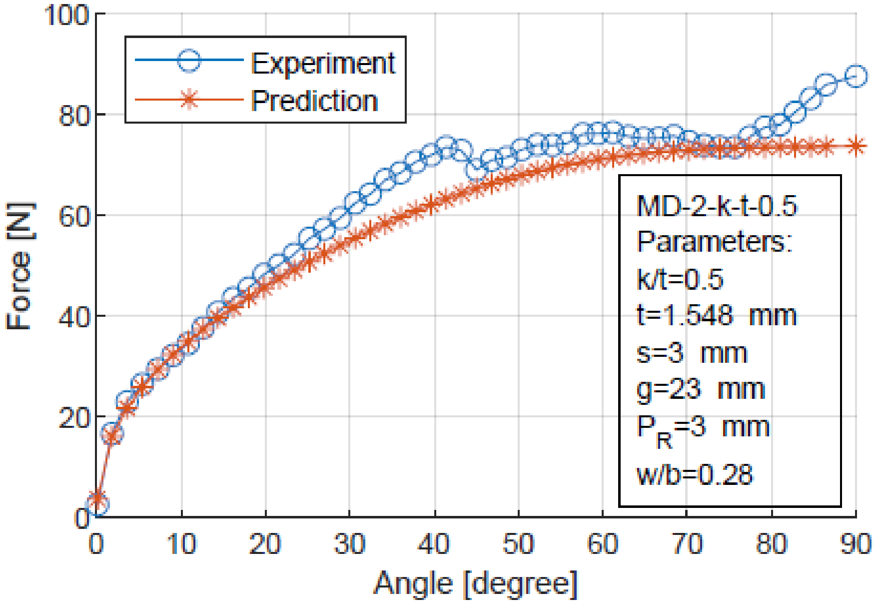

Figure 5.11: Validation of OSM bending force: case MD-2-k-t-0.5

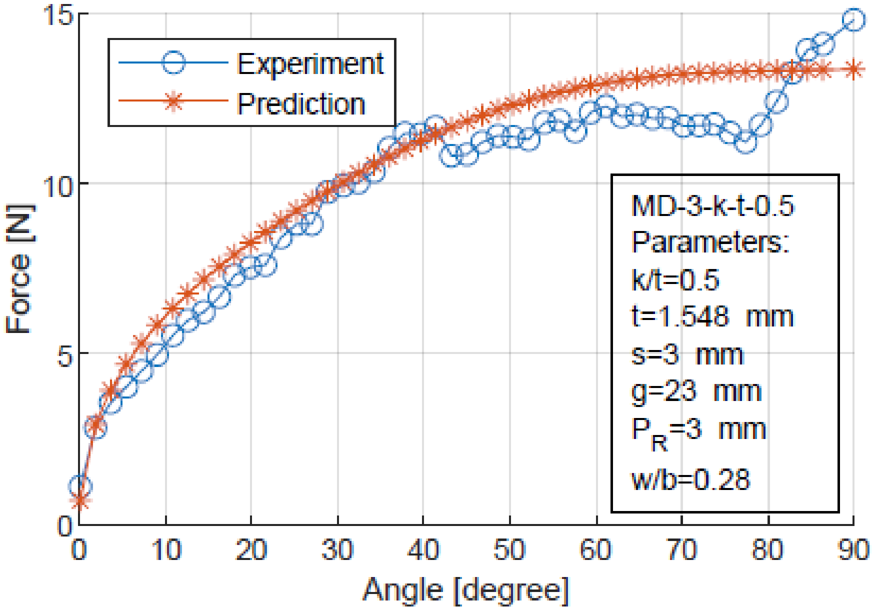

Figure 5.12: Validation of OSM bending force: case MD-3-k-t-0.5

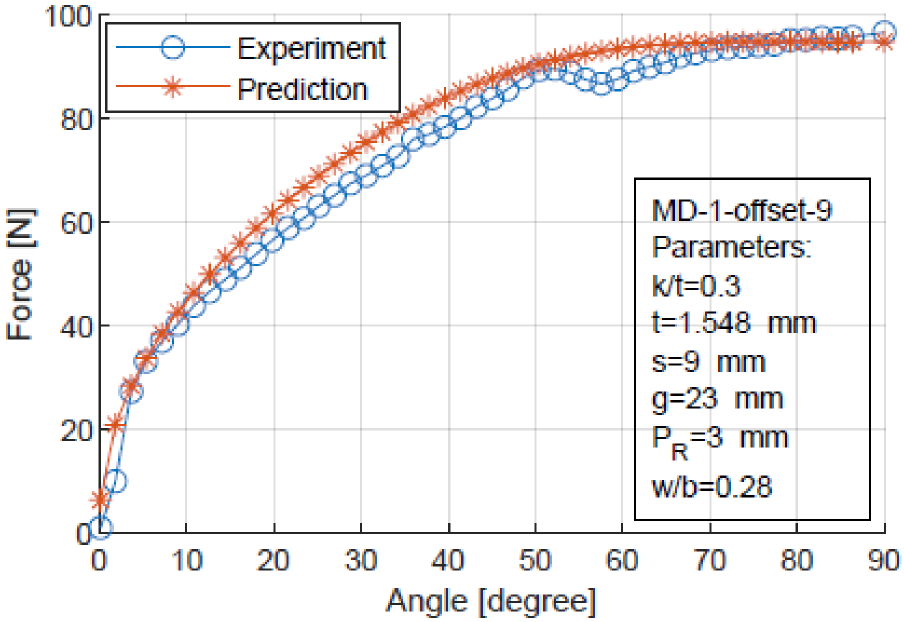

Figure 5.13: Validation of OSM bending force: case MD-1-offset-9

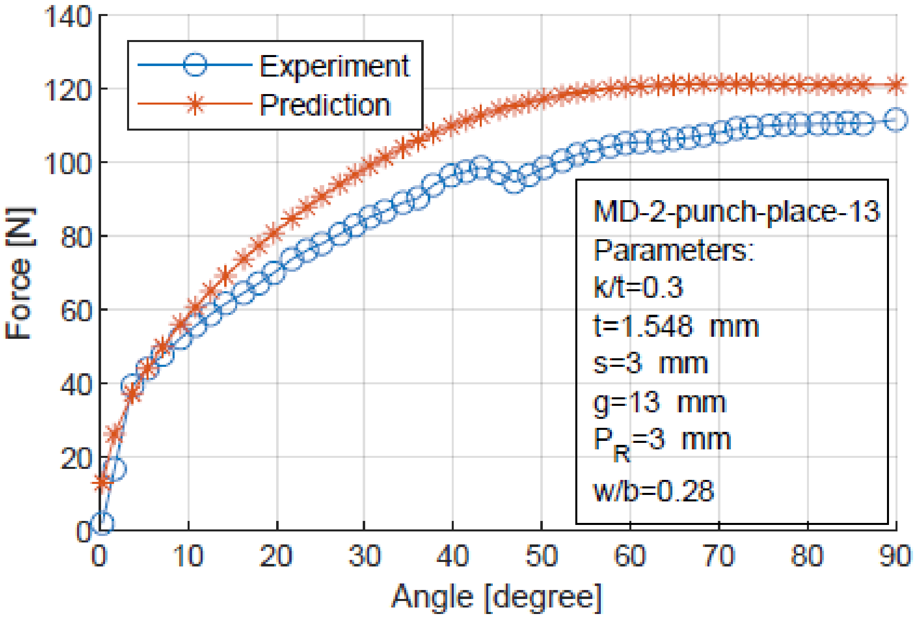

Figure 5.14: Validation of OSM bending force: case MD-2-punch-place-13

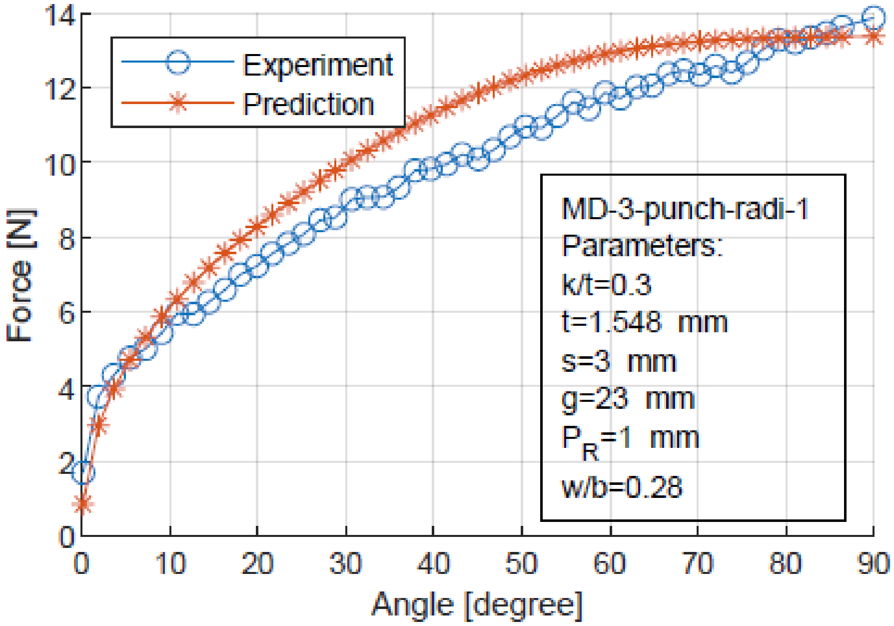

Figure 5.15: Validation of OSM bending force: case MD-3-punch-radius-1

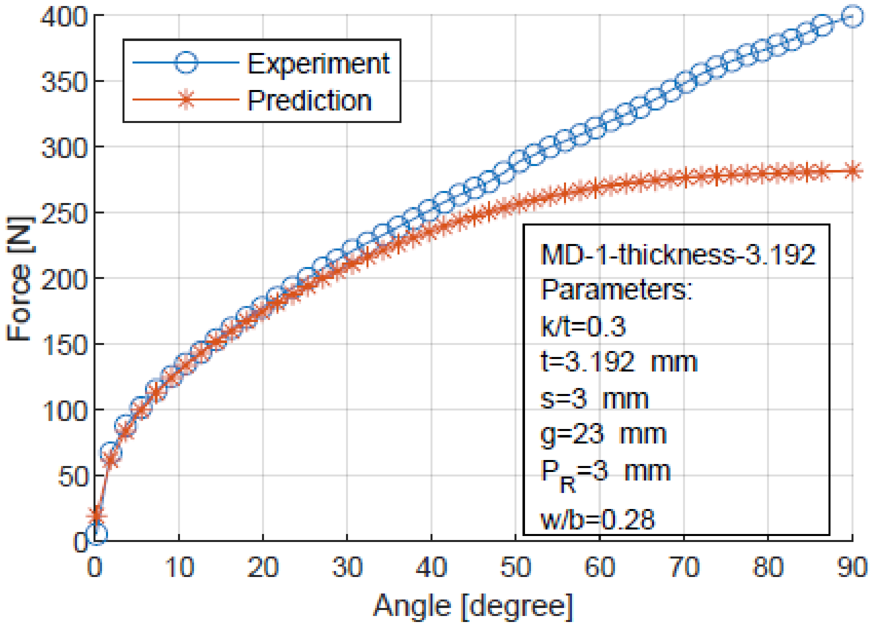

Figure 5.16: Validation of OSM bending force: case MD-1-thickness-3.192

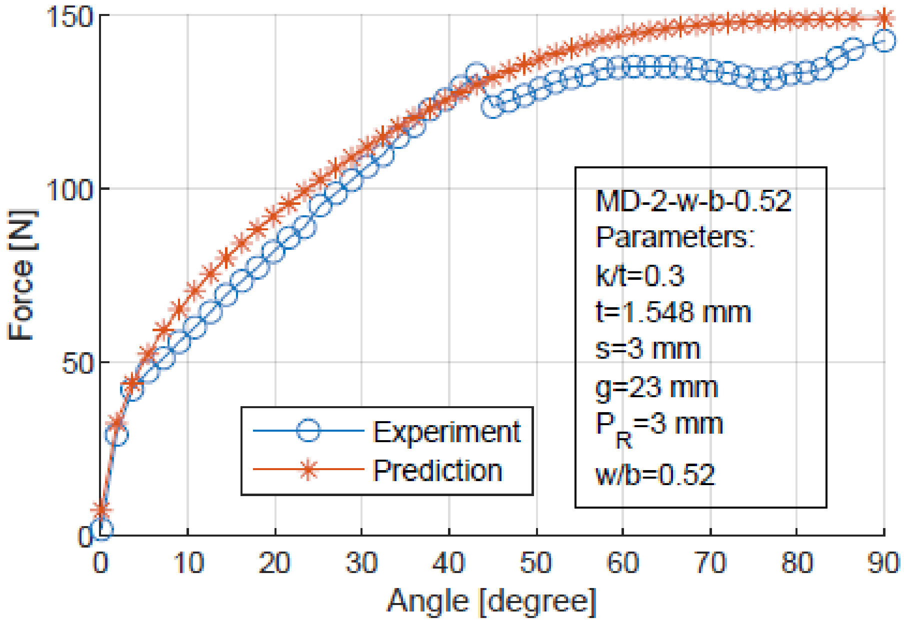

Figure 5.17: Validation of OSM bending force: case MD-2-w-b-0.52

The results show that force prediction is in good agreement with experimental measurements. The prediction model has good accuracy in small-angle bending. As the bending angle increases, the predictions deviated from measurements and failed to follow measurement data closely. However, the deviation is relatively small, except for case No. 32, which is shown in Fig. 5.16.

Usually, the repeatability of an experiment is suspected of causing the inaccuracy. Hence, repeatability of case No. 32 is examined as shown in Fig. 5.9. As mentioned earlier, the three replications shows overlapping results. Hence, repeatability is not a probable cause.

Further analysis showed that the force prediction deviation from experimental measurement can be categorized into two types. The first type is the prediction model cannot track experiment data closely, for example, the range 30-50° in Fig. 5.10. The second type, prediction model deviates when changing a particular parameter, thickness change in Fig. 5.16 for example.

The reason for the first type is that the proposed regression model in Eq. (5.17) has a sine function that takes the bending angle θ as an independent variable. Hence, it appears that the sine function dictated the shape of the prediction model. Consequently, fluctuations in bending force, the range 30-50°in Fig. 5.10, are not captured closely.

The discrepancy for the second type, shown in Fig. 5.16 for example, is suspected to be caused by two factors. (a): the term F_b in Eq. (5.19) is function of square of OSM specimen thickness, refer to Eq. (5.15). Thus, it may have a higher weight in OSM bending force compared to other terms in Eq. (5.19). This might have resulted in a drastic change when changing thickness. (b): the number of values for the parameters in the experimental data set is three for all parameters except the kerf-to-thickness (k/t) ratio as tabulated in Table 5.1. For example, the sheet thickness has only three different values, which are 1.548 mm, 2.288 mm, and 3.192 mm. Only six specimens have thickness values other than 1.548 mm in the whole study. Thus, the prediction model might not have enough variation to describe the effect of this parameter.

As a result, the prediction of the regression model is noticeably different when predicting OSM bending force for a specimen having a different thickness. Hence, it needs further study to find out the cause and improve the prediction accuracy.

5.5 Summary

A force prediction model is presented for OSM bending and validated through comprehensive experiments. In addition to the MD type and bending angle, there are six different parameters considered in this study. These six parameters are associated with bending configuration and MD design. The experiment confirmed the bending force is affected by sheet thickness (t), web-to-width ratio (w/b), punch placement (g), offset distance (s).

It is found that OSM bending force is not affected by kerf-to-thickness (k/t) ratio, and radius of punch, (R_p). Unlike the other parameters, the MD type is considered a categorical variable in regression models. Experiment data were divided into two sets, of which one is used to obtain the regression coefficients in the prediction model; the other is used to validate the model. The prediction model predicts the bending force for most of the cases well. This model can be used as a design tool for OSM bending.

The input for the prediction model includes MD type, the effective length along the bending line, the geometric configuration of the OSM bending setup, sheet thickness, and material properties such as the strength coefficient, and hardening exponent. The prediction model serves as an estimation tool for OSM bending based on the inputs mentioned above, which can be easily obtained.

The prediction model reveals that c_1 is a shape factor representing different MD topologies. This model can be extended to other MDs if the shape factor c_1 is identified. Hence, future improvements of the model will address ways to identify c_1 for different MD types and other perforated patterns by mathematical, statistical, and experimental methods.

Future work can be extended to reducing the gap between prediction and experimental measurement to capture fluctuations in bending force magnitude.

Chapter 6

EXPERIMENTAL EVALUATION OF TENSION AND SHEAR RESPONSES OF MATERIAL DISCONTINUITIES IN ORIGAMI-BASED SHEET METAL BENDING

6.1 Background

Chapter 3 and 4 indicate tension and shear are two main load types that MDs are subjected to during OSM bending. When a sheet with a MD is bent using OSM bending, generally the outer surface is under tension, and the inner surface is under compression in addition to observance of shear deformation. As the bending load concentrates on the MD during the bending process, failure of the sheet mostly likely happens on the MDs due to the tension or shear load. It is thus imperative to investigate the responses of the MDs under tension and shear loading to achieve successful OSM bending operation. Hence, this Chapter aims, firstly, to evaluate the responses of MDs under tension and shear loads. Secondly, based on the responses of MDs under tension and shear loads, we attempt to assess if the OSM sheet will fail during bending using two ductile fracture criteria (DFC). In this process, the critical values for the two DFC are determined experimentally from standard tests, and the OSM bending is simulated using finite element analysis (FEA). Thus, this chapter comparatively studies five different MDs in terms of their tension, shear load responses, deformation developed on the MDs, and the possibility of failure occurring during the OSM bending.

6.2 Experimental procedure

6.2.1 Testing method selection

The MDs can be seen as defects or notches in the sheet. In the past, researchers have investigated the effect of various types of discontinuities (notches) in metal sheets under tension and shear in the context of stress concentration factor [132], constitutive behavior and large strains [133,134], testing method development [135–137], and fracture [138]. The literature shows that the shape of notches investigated is limited to simple shapes like MD-1 shown in Fig. 1.1. Though various testing techniques are employed during these studies, we realize that there is no ready-to-use standard testing method and equipment to measure the load and deformation on the OSM sheet when it comes to the OSM bending shown in Fig. 1.2. Therefore, it seemed necessary to design and fabricate special devices to measure responses of the MDs in terms of loading force and strain. For example, to control the movement of the punch during the OSM bending, it needs a position control system. To hold the sheet sample, the test needs a special fixture design that can be incorporated with force and strain measurement. This would make the testing process costly and complicated. To cope with this obstacle, we proposed achieving the goal by using the simple tension and shear tests. In the proposed tension and shear testing method, the MDs can be easily incorporated into tension and shear test samples. In addition, simple tension and shear test can be performed using readily available universal testing machine. The response of the MDs in simple tension and shear test can reveal the tension and shear behavior of the sheet in OSM bending operation. The applied force and strain can be conveniently measured using universal testing machine and full-filed displacements and surface strain field measurement using a DIC system.

6.2.2 Testing plan

Five different MDs are selected from available topologies shown in Fig. 1.1. In addition, to provide a valid comparable value, the standard tension and shear samples with no MD are prepared for benchmarking purposes. The MDs tested in this study are MD-1, MD-2, MD-3, MD-5, and MD-6. The selected MDs are the basic topologies and other topologies can be built upon these five designs. In order to make a fair comparison between MDs with different topologies, it is ensured that the same length of material is left along the bending line after applying MDs in the middle of the specimen. The sheet material is aluminum alloy 6061 temper O (AA 6061-O) with a thickness of 1.6 mm (14 gauge). Each test sample is repeatedly tested with four specimens to account for repeatability of results. Table 6.1 lists the loading type, material, MD type, and the number of specimens tested for each experiment.

6.2.3 Specimen preparation

For the tension test, a sheet type tension specimen is prepared according to ASTM E8/E8M-9 [139]. Then, the MDs are fabricated in the middle of the specimen. The dimensions of the tension specimen and the selected MDs are illustrated in Fig. 6.1 , where Fig. 6.1 (a) is standard sheet type tension specimen without any MD, Fig 6.1 (b)-(f) are detailed views of each MD pattern investigated in this work. The outline dimensions of the tension specimen, such as length (L), width (W), gauge length (A) etc., are identical to that of sheet type specimen prescribed in the ASTM E8/E8M-9. The dimensions of MDs are obtained with following procedure. In first step, a kerf-to-thickness ratio of 0.3 is selected based on literature [19, 131, 140]. In second step, a proper value for the remaining width of sheet

Table 6.1: The experimental plan for MD pattern loading. STD. tension (shear) refers to the standard sheet metal with no MD applied.

Loading type	MD type	Material	Thickness [mm]	Repetition for each MD
Tension	MD-1 MD-2 MD-3 MD-5 MD-6 STD. tension	AA-6061-O	1.6	4
Shear	MD-1 MD-2 MD-3 MD-5 MD-6 STD. shear	AA-6061-O	1.6	4

after applying MDs (denoted by b in the Fig. 6.1). Tension loading specimen details and MD specification in Fig. 6.1, and Fig. 6.3 are determined considering (a) the width of specimen (W), (b) the fact that the same amount of material should be left in order to compare different MDs in terms of their responses to tension and shear load. Finally, the remaining dimensions are derived from step one and step two.

For the shear test, the shear specimens are adapted from ASTM testing standard B831-14 [141]. In order to test the shear response of MDs, three modifications are made to the standard shear test specimen designed for the DIC in ASTM B831-14. The DIC is an optical method that offers non-contact, optical measurement of 2D and 3D full-field displacement and strains [99, 142–144] More details about DIC is presented in Chapter 2.3.

The first modification is made to the shear zone, where the length of the shear zone is doubled to include MDs. The shear zone in the standard shear specimen is set to 7 mm in length, which is not enough space for applying any of the MDs. The second modification is made to the end of the standard rectangular shear specimen shown in Fig. 6.2 (a). The width is reduced from 38 mm to 25 mm, as in Fig. 6.2 (b), so that the specimen can be gripped on its entire width. In this test, the gripping width of the universal testing machine 3369 turns out to be narrower than the width of the rectangular shear test specimen. This modification would prevent

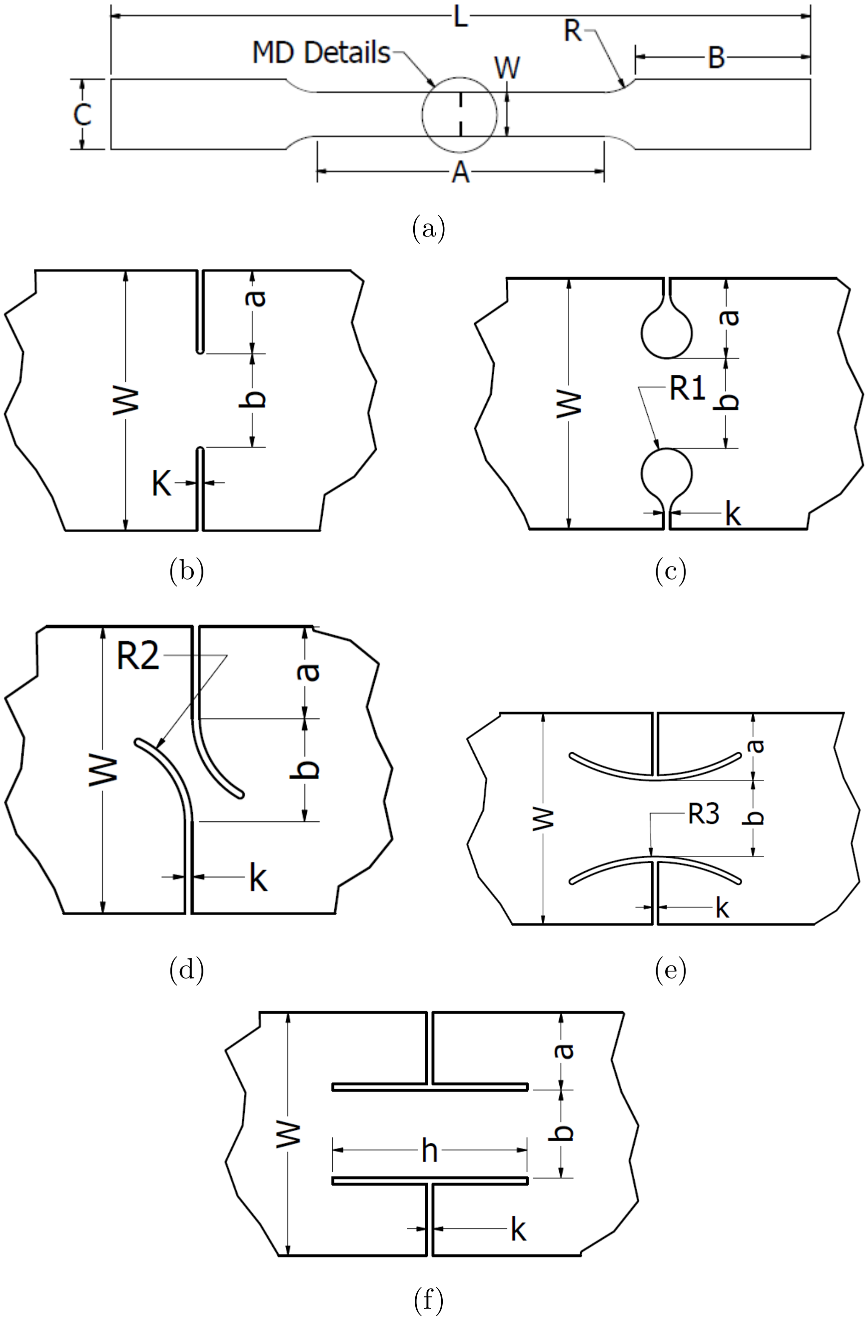

(a)

(b)

(c)

(d)

(e)

(f)

Figure 6.1: Tension specimen and MD specification. The dimensions L=200 mm, B=50 mm, R=12.5 mm, W=12.5 mm, A=82 mm, a=4 mm, b=4.5 mm, k=0.5 mm, R1=2.5 mm, R2=8 mm, R3=20 mm, h=10 mm

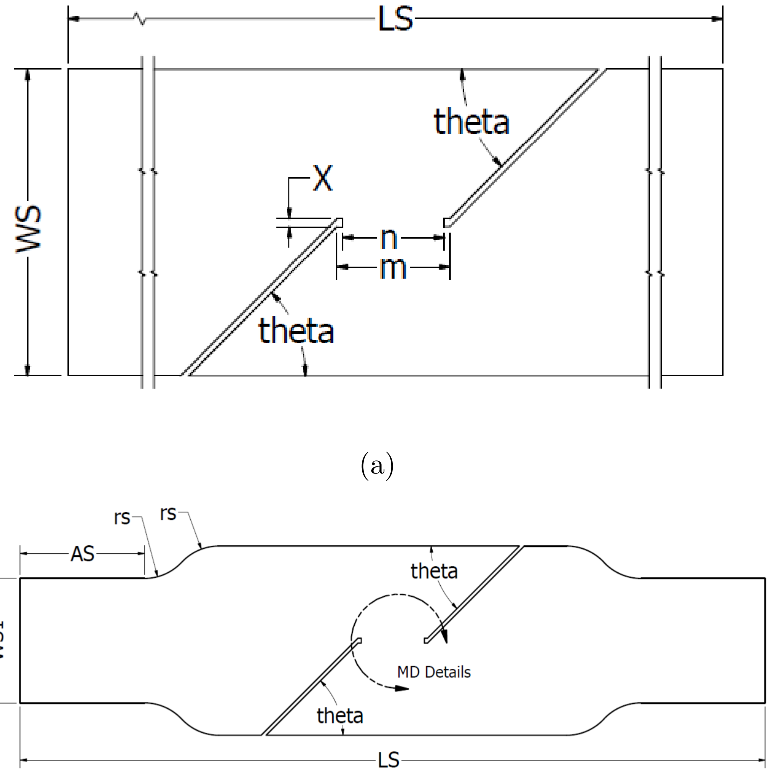

(a)

(b)

Figure 6.2: Shear sample, (a) standard shear sample; (b) reduced end shear standard sample; The dimensions: LS=150 mm, WS=38 mm, Theta=45° , WS1=25 mm, AS=25 mm, rs=10.3 mm

bending and rotation of the shear specimen during the test. The third modification is the application of the MDs at the shear zone. The details are shown in Fig. 6.2 (c)–(g) representing the applied MDs. The dimensional values of MDs in shear test samples are also obtained using the same steps described earlier for the tension test specimens. For all specimens, the MDs are cut by micro waterjet cutting to ensure dimensional accuracy within ±0.025 mm. During the test, the strain measurement is carried out by a DIC system that has a camera resolution of 2752 × 2200 (pixel). The specimens are painted with black and white paint to create a stochastic pattern, which is a necessary procedure for measuring strain using DIC.

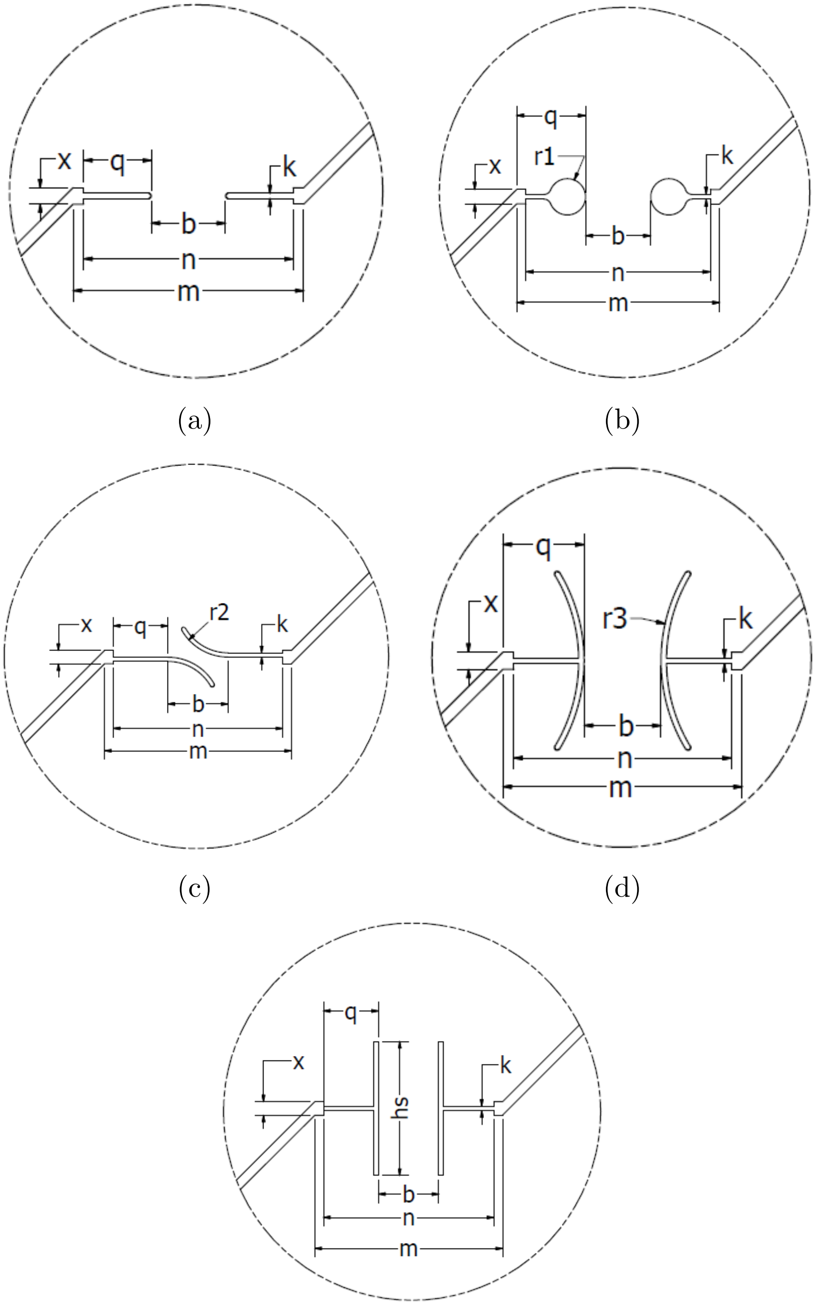

(a) (b)

(c) (d)

(e)

Figure 6.3: MD detailed view on shear sample, (a) MD-1; (b) MD-2; (c) MD-3; (d) MD-5; (e) MD-6; The dimensions b=4.5 mm, k=0.5 mm, q=4 mm, r2=4 mm, r3=10 mm, hs=10 mm, m=14 mm, n=12.7 mm, X=1 mm.

6.2.4 Testing process

Both tension and shear tests are performed on an Instron universal testing machine 3369. The testing standards followed are ASTM testing standard E8/8M-9 for the tension test and ASTM B831-14 for the shear test. The test speed is controlled by the extension rate of the load cell of the universal testing machine. For the STD. tension sample, the extension rate is set to 1.23 mm/min prior to yield and 10 mm/min for post-yield. The extension rate for the tension sample with MDs is 0.1 times of the extension rate set for the STD. tension samples. In the shear test, a 1 mm/min extension rate is used for all shear samples. In both tension and shear tests, the time, load, and extension of the crosshead are recorded by the universal testing machine. Images are captured using a DIC system with an identical frequency as configured in the universal testing machine to analyze strain generated in the samples.

6.3 Results and discussion

The results of the tests are evaluated in terms of maximum force applied on MDs and corresponding extension. The strain and stress analysis is carried out in order to predict failure in OSM bending. Particularly, fracture strain is analyzed for tension tests using the strain measured with DIC. Maximum shear stress is analyzed in the shear tests using the force measurement.

6.3.1 Tension behavior observation

6.3.1.1 Maximum tension force and extension

Figure 6.4 shows the behavior of the MDs under tension until a fracture occurs. The maximum force and corresponding extension averaged from the replicas are tabulated in Table 6.2. These results indicate that introducing a MD into the standard tension sample significantly reduced maximum tension force and corresponding extension, as expected.

The change in sample topology caused by the MDs leads to a concentration of load around the MDs and as a result the localization of strains. If we compare the MDs in terms of maximum tension force that the MDs are subjected to, we observe that MD-1 can withstand the highest magnitude of tension force among all MDs types, followed by MD-5, MD-2, and MD-6. The magnitude of maximum tension force on these three MDs are almost the same, i.e. 647∼673 N. The magnitude of maximum tension force on MD-3 is the lowest because MD-3 topology has the smallest area to resist tension force among all MDs. When taking the standard tension sample as a benchmark, the least amount of reduction, 65.3%, in terms of maximum tension force occurred in MD-1, while the maximum amount of reduction, 91.6%, in terms of maximum tension force took place in MD-3. Interestingly, MD-1, MD-2, MD-5, and MD-6 all are within the 65-69% range in terms of reduction of

Table 6.2: Maximum tension force and extension

Sample type	Max tension [N]	Avg. Extension At Max Tension [mm]	Change in Max tension due to MD [%]	Change in extension due to MD [%]	Initial effective cross section area [mm^2]
MD-1	732	0.59	-65.3	-96.7	7.2
MD-2	656	0.65	-68.9	-96.3	7.2
MD-3	178	2.18	-91.6	-87.6	7.2
MD-5	673	1.06	68.1	-94.0	7.2
MD-6	647	2.26	69.3	-87.2	7.2
STD. tension	2109	17.65	—	—	20

Table 6.3: Fracture strain on MDs under tension load

Cases	MD-1	MD-2	MD-3	MD-5	MD-6
Fracture Strain [mm/mm]	0.672	0.542	0.583	0.525	0.643

maximum tension force. This similarity arises from the fact that as the tension force approaches gradually to its maximum, the change in effective cross-sectional area of these four MD doesn't differ significantly from each other. On the other hand, MD-3 has the least amount of tension load-bearing capability because it has the smallest effective cross-section area that will resist the tension force. It is also noticeable that the extension of crosshead at maximum tension force significantly dropped on all samples with MD. The decline in extension is most obvious in MD-1 with 96.7% while it is 87.6% in MD-6. Comparing the magnitude of extension at maximum tension force among the MDs shows that MD-6 outperforms all other MDs. MD-6 extends more than twice as much as MD-5. Also, MD-6 extends more than three times as much as MD-1 and MD-2. This behavior is caused by the topology of MD-6 that has a straight slot in the direction of tension.

6.3.1.2 Strain analysis under tension

The strain at fracture is determined from the tension test using DIC. According to the tension test method prescribed in ASTM E8/8M-9, fracture occurs when the maximum force on the specimen drops by 10%.

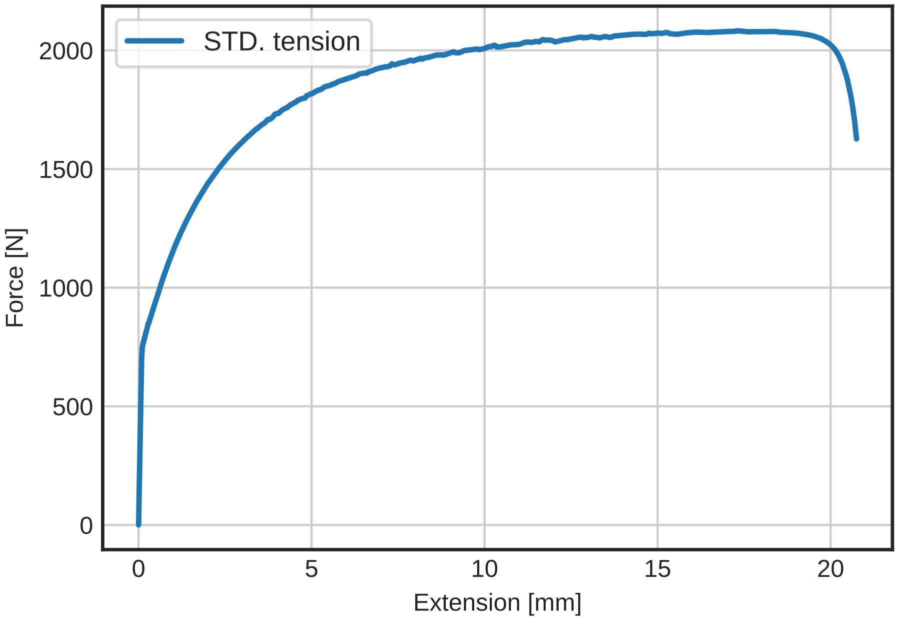

(a)

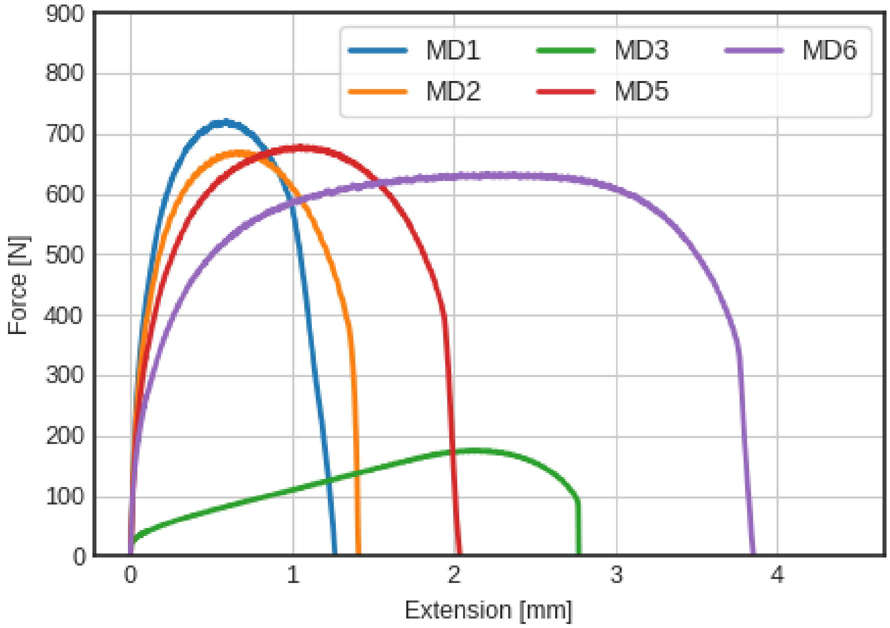

(b)

Figure 6.4: Tension force and extension, (a) Standard (STD.) tension sample; (b) MD tension sample.

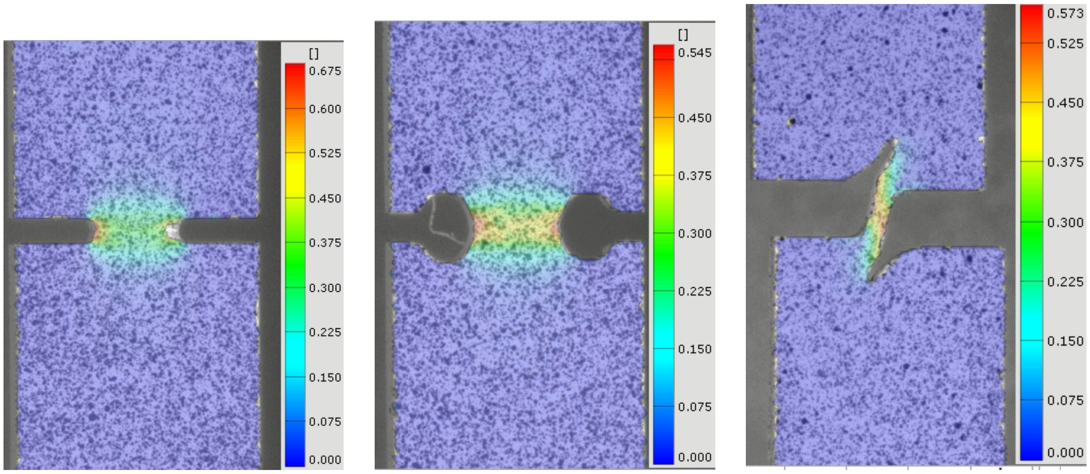

(a) MD-1 (b) MD-2 (c) MD-3

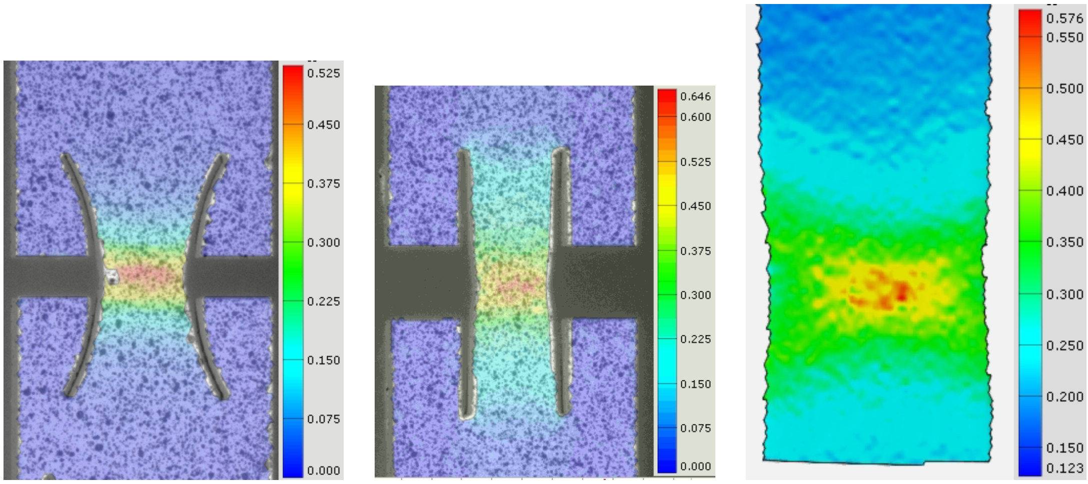

(d) MD-5 (e) MD-6 (f) STD. tension

Figure 6.5: True equivalent strain distribution at fracture in tension test

Table 6.4: Maximum shear force, and extension

Sample type	Max shear [N]	Avg. Extension At Max shear [mm]	Change in Max shear due to MD [%]	Change in extension due to MD [%]	Initial effective cross section area [mm^2]
MD-1	669	1.42	-49.2	-58.6	7.2
MD-2	656	3.23	-50.2	-5.83	7.2
MD-3	217	0.75	-83.5	-78.1	7.2
MD-5	577	4.43	-56.1	+29	7.2
MD-6	509	3.40	-61.4	-0.8	7.2
STD. shear	1317	3.43	—	—	20.32

Hence, a stage in which the tension force drops to 90% of the maximum tension force is identified in DIC. The true equivalent strain on this stage is taken as fracture strain. The true equivalent strain distribution is shown in Fig. 6.5. The values of true equivalent strain at fracture are tabulated in Table 6.3. These values are used as the basis for predicting whether a failure occurs in OSM bending if the same MDs are bent. The equivalent true strain distribution reveals the strain localization on the MDs while the magnitude of the strain is far less in other parts of the specimen.

6.3.2 Shear test observation

6.3.2.1 Maximum shear force and extension

Analysis of maximum shear force and the corresponding extension in the shear test is shown in Fig. 6.6 and Table 6.4. These results indicate that applying the MDs in the shear zone has decreased the maximum shear force and corresponding extension drastically. The maximum shear force on MDs exhibits a similar trend as the maximum tension force does. Ranking the MDs in terms of maximum shear force, MD-1 reached the highest magnitude while MD-3 has the lowest magnitude.

Application of MD-1, MD-2, MD-5, MD-6 at the shear zone leads to a reduction in maximum shear force within a range of 49%-61%. The reason is that the change in effective cross-section areas of these four MDs is not much different as the shear force approaches to the maximum value. The shear load on MD-3 also creates tension effect due to the narrower web of MD-3 topology, which leads to the least amount of extension among all the MDs tested. Because of the tension effect, MD-3

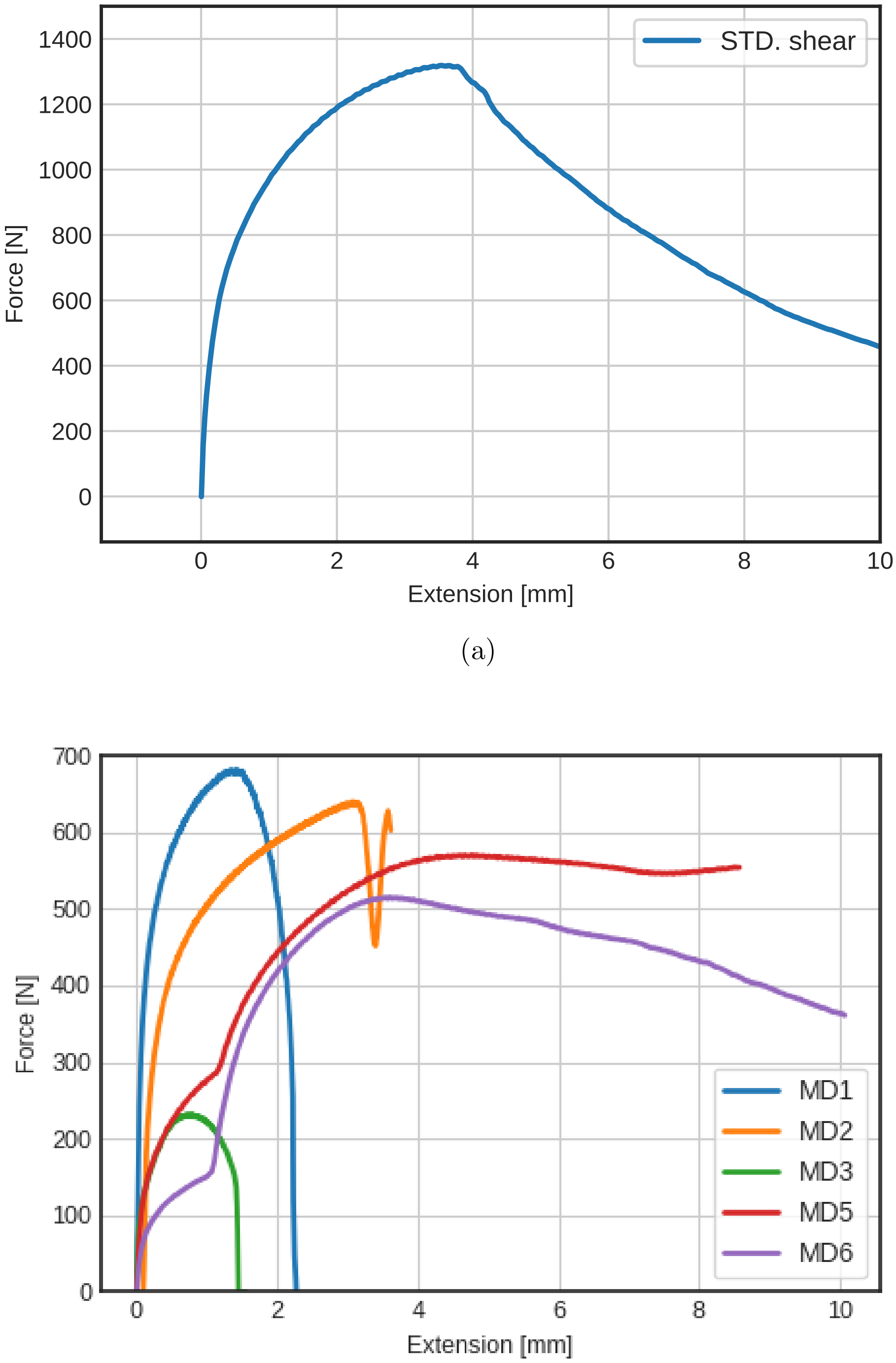

(a)

(b)

Figure 6.6: Shear load and extension

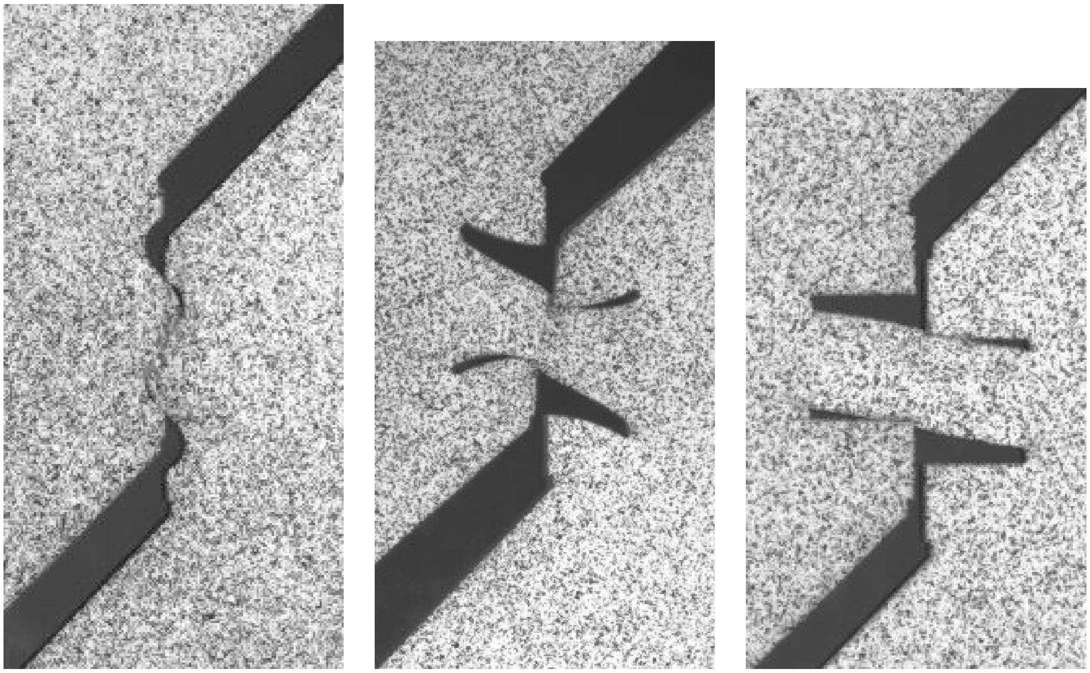
(a) (b) (c)

Figure 6.7: Self-contact happening under shear load, (a)MD-2; (b) MD-5; (c) MD-6.

didn't fracture in the direction of the shear load. It can be seen from Fig. 6.6 that the shear force has a fluctuation in MD-2, MD-5, and MD-6. The fluctuation in force is due to self-contact, shown in Fig. 6.7. Due to the topology of these MDs, parts of the MDs come in contact and the shear force increases consequently to overcome the increase in deformation resistance. In terms of the extension under the shear force, self-contact greatly influences the magnitude of extension. The magnitude of extension in MD-1 and MD-2 is expected to be close to each other. However, MD-2 has 127% more extension than MD-1 due to self-contact. The extension obtained at the maximum force in MD-2 is not a pure shear extension. Part of the extension at maximum shear force in MD-2 is attributed to the extension to overcome contact resistance once self-contact starts occurring. Similarly, part of extension at maximum shear load in MD-5, MD-6 is coming from the effort to overcome self-contact.

6.3.2.2 Maximum shear stress under shear

In the shear test, the maximum shear stress is determined using Eq. (6.1) [145],

$$\tau_{max} = \frac{F_{max}}{Lt} \tag{6.1}$$

Table 6.5: Maximum shear stress τ_{max} on the MDs

Cases	MD-1	MD-2	MD-3	MD-5	MD-6
τ_{max} [MPa]	92.9	91.1	30.1	80.1	70.69

where τ_{max} is the maximum shear stress, F_{max} is the maximum shear force, L is the length of the shear zone, t is the thickness of the sheet. The maximum shear stress for each MD is calculated in Table 6.5. These values are used as a benchmark to predict if fracture happens due to shear during OSM bending.

6.4 Failure prediction in OSM bending

The test results show stress concentrated around the MDs under both tension and shear load. Hence, failure is expected to occur on the MDs. The possibility of failure of the sample during OSM bending is evaluated using DFC.

6.4.1 Ductile fracture criteria (DFC)

Researchers proposed numerous DFC [146,147] up to date. Considering simplicity and practicality, in this study, two DFC are chosen to predict failure in OSM bending, namely constant equivalent plastic strain and maximum shear stress. Constant equivalent strain criterion states that fracture is assumed to occur when equivalent plastic strain reaches a critical value,

$$\bar{\epsilon} = \bar{\epsilon}_f \tag{6.2}$$

for incompressible plastic material the equivalent strain is defined as

$$\bar{\epsilon} = \sqrt{\frac{2}{3}(\epsilon_1^2 + \epsilon_3^2 + \epsilon_3^2)} \tag{6.3}$$

where $\epsilon_1, \epsilon_2, \epsilon_3$ are the principal strains.

Fracture also occurs due to shear and thus the maximum shear stress criteria state that fracture occurs when the maxim shear stress reaches a critical value.

$$\tau_{max} = (\tau_{max})_f, \tag{6.4}$$

where the maximum shear stress τ_{max} is defined as

$$\tau_{max} = max\left\{\frac{\sigma_1 - \sigma_2}{2}, \frac{\sigma_2 - \sigma_3}{2}, \frac{\sigma_3 - \sigma_1}{2}\right\}, \tag{6.5}$$

and $\sigma_1, \sigma_2, \sigma_3$ are the principal stresses.

6.4.2 Finite element simulation of OSM bending

The failure prediction using the two DFC is dependent on the magnitude of deformation generated during the OSM bending process. For the reasons mentioned in section 6.2.1, no available standard test method and equipment are available for evaluating the deformation happening during OSM bending. Therefore, FEA of OSM bending process are carried out to provide an evaluation model. The FEA is performed in accordance with the setup shown in Fig. 1.2 and the values of the parameters used in the simulations are g = 23 mm, s = 3 mm, R_p=3 mm, t = 1.6 mm, where g is the gap between the edge of support (blank holder) and punch, s is the offset distance, R_p is the punch radius, t is the sheet thickness. In this work, five simulations are carried out representing each of the MDs topology under study. The dimensions of MDs modeled in the FEA are identical to the dimension of MDs tested in the tension and shear samples.

In the FEA, material properties of the AA6061-O sheet are identified from the response of the standard tension sample and fed into a multilinear isotropic hardening plasticity material model in Ansys®2019 R1. The punch, die, and the blank holder are modeled as rigid bodies. The area around the MDs is discretized with fine mesh to ensure the accuracy of the simulation results. The simulation is performed with two steps. First, the pressure load is applied to the blank holder to hold the sheet firmly between the blank holder and the die. Then, the punch is displaced 18.4 mm along the X-axis, 20 mm along negative Y-axis to bend the sheet up to 90°.

6.4.3 FEA results and failure prediction

The results from FEA of OSM bending are analyzed in terms of equivalent plastic strain and shear stress to predict the possibility of occurring failure. The equivalent plastic strain distribution at 90° bend is shown for each of the MDs in Fig. 6.8 and the maximum shear stress distribution is presented in Fig. 6.9. The equivalent plastic strain field indicates that high deformation occurs at the edges at the end of MDs where the failure is expected to happen. The shear stress field shows a high magnitude of shear deformation is generated at the outer and inner surfaces of MDs.

The shear deformation in this area is caused by the tension and compression generated during bending. As the punch progresses to its final position, the tension force develops on the outer surface and the compression force develops on the inner surfaces of the MDs.

To predict the possibility of failure during OSM bending, the deformation field is benchmarked against the critical values of equivalent strain and shear stress identified in section 6.3.1.2, and section 6.3.2.2, respectively. The failure prediction results obtained using the two DFC are presented with a bar chart in Fig. 6.10.

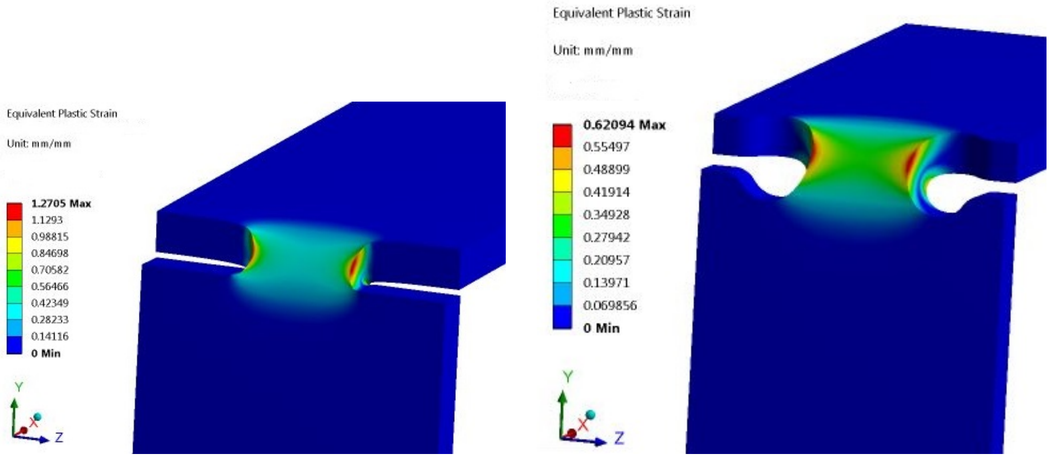

(a) MD-1

(b) MD-2

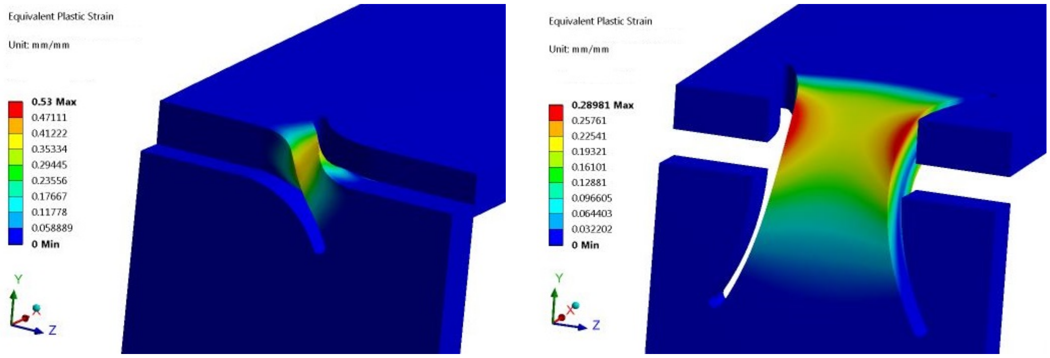

(c) MD-3

(d) MD-5

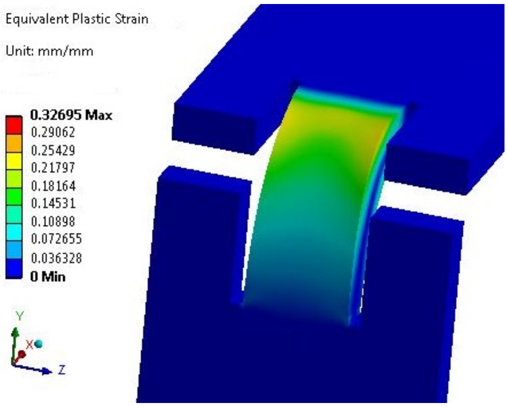

(e) MD-6

Figure 6.8: Distribution of equivalent plastic strain

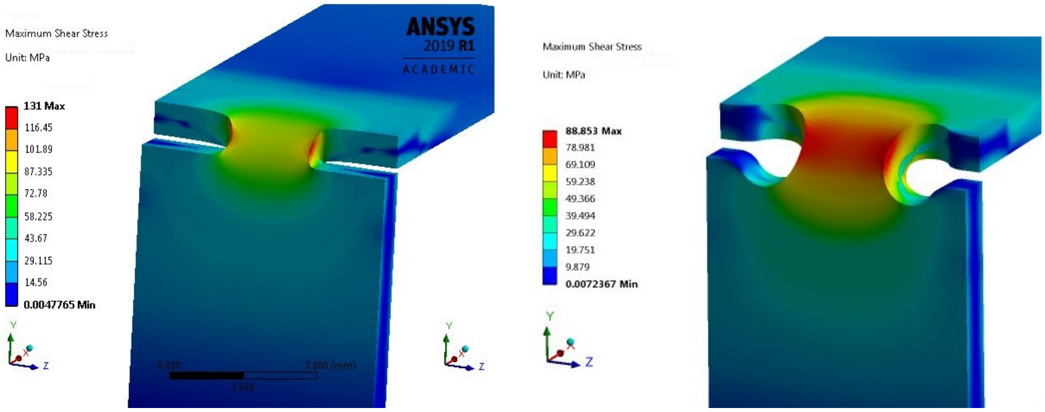

(a) MD-1 (b) MD-2

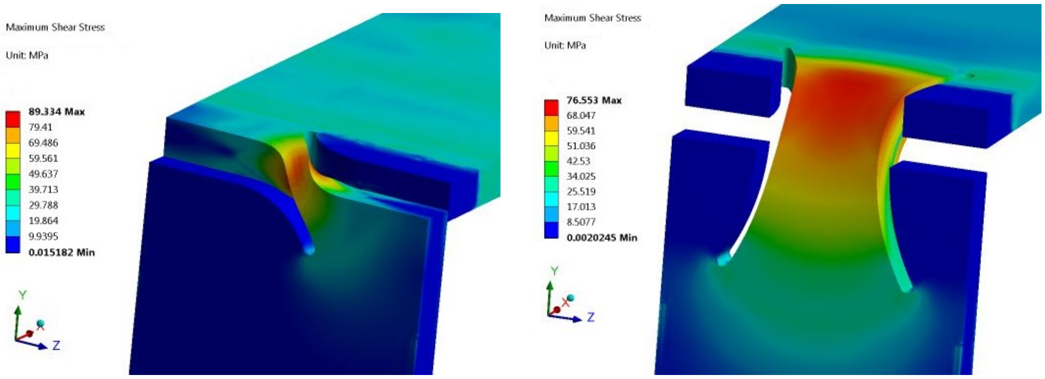

(c) MD-3 (d) MD-5

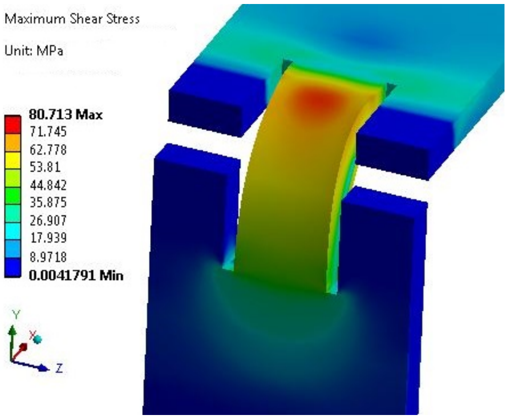

(e) MD-6

Figure 6.9: Distribution of maximum shear stress

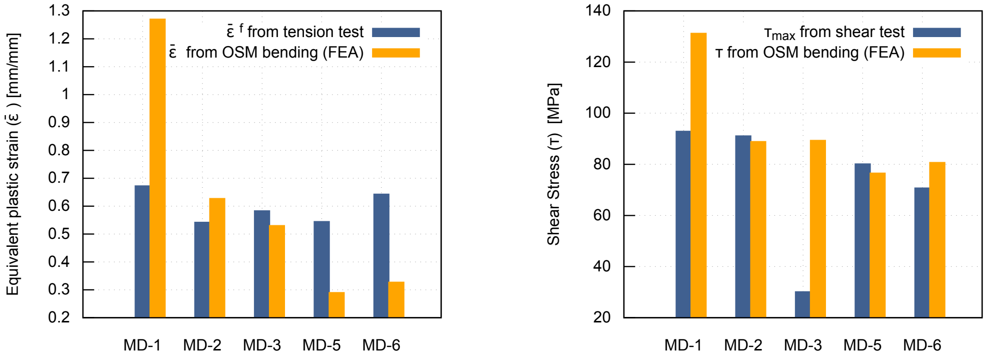

(a) Failure Prediction by Equivalent Plastic Strain

(b) Failure Prediction by Maximum Shear Stress

Figure 6.10: Failure prediction results using two DFC

According to constant equivalent strain criteria, a failure occurs on MD-1 and MD-2. On the other hand, a failure occurs on MD-1, MD-3, and MD-6 according to maximum shear stress criteria. This prediction shows, on one hand, that the failure can occur due to any of the tension or shear loads. And on the other hand, the results point towards the fact that each DFC has certain prediction accuracy limitations when applied to OSM. The discrepancy in prediction may also stem from how the critical values for each criterion are identified. For example, in constant equivalent strain criteria, the fracture strain is identified when the maximum force drops by 10%, which may not be accurate all the time. In maximum shear stress criteria, the maximum shear stress is determined from the maximum shear force, which might be overestimated because of self-contact in the MDs.

6.5 Summary

Tension and shear response of the MDs are investigated by adopting standard tension and shear testing methods. The deformation behavior of the MDs at maximum tension and shear forces are compared. A set of critical values for constant equivalent strain and maximum shear stress criteria are determined from tension and shear tests to predict the possibility of a failure in OSM bending. Results show an average extension of the entire specimen under tension reduced significantly due to the application of the MDs. The tension and shear load-bearing capability of a MD can be related to the change in the area of the effective cross-section. This can be clearly observed from the load magnitude range of MD-2, MD-5, MD-6. Extension under tension load depends on how uniformly a MD can transmit the load. This is noticeable when comparing MD-5 and MD6 under tension load. Shear behavior of MD is discovered to be affected by self-contact in MD-2, MD-5, and MD-6. Self-contact increased load-bearing capability of OSM sheet. In MD-5, MD-6 secondary shear zone occurred due to self-contact, as well. The modified tension and shear tests in a combination of FEA analyses of OSM bending can provide a simple approach to predict failure in OSM bending.

Chapter 7

INVESTIGATION OF FAILURE BY FRACTURE IN ORIGAMI-BASED SHEET METAL BENDING

7.1 Background

In this chapter, the term, scale, is defined as the ratio of kerf to the thickness of the sheet. The kerf is the width of the material being removal by the cutting tool along the MDs geometrical outline.

Chapter 4 implied that the scale of the MDs is crucial to achieving successful bending. On one hand, a small scale of the MDs results in a higher magnitude of stress on the MDs, which can cause fracture and tear during the OSM bending process. For instance, the smallest scale investigated in chapter 4 was 0.2, which is 0.32 mm on a 1.6 mm thick sheet. The stress magnitude generated on MD-2 due to a 0.2 scale is 12.4% higher than the stress level caused by a 0.3 scale on MD-2. On the other hand, a large scale of MD may defeat the purpose of OSM bending where the bending may not occur at the desired location. The chapter carried by Nikhare [148] shows a large scale of MD gives rise to a bending of the sheet along one edge of the MD, which is not desirable. These studies implicate that the proper selection of the MD scale is a critical factor that influences the success of OSM bending operation in terms of failure and accuracy. Hence, being able to predict the possibility of failure based on a given MD scale is an important step that needs to be investigated.

However, current literature shows no research on the proper selection of the MD scale has been carried out. Therefore, this study attempts to identify the impact of the MD scale on the fracture that occurred during the OSM bending. Particularly, this works is dedicated to predicting the possibility of a fracture during the OSM bending process using the DFC.

7.2 Methodology and scope

The failure in sheet metal forming has been assessed using the concept of formability [149] that has been developed from strain-based forming limit diagrams (FLD) [150, 151]. In FLD, the strain is measured until necking with a different strain path [152], and the strain magnitude causing failure is recorded. A diagram can be constructed by combining various strain paths. The diagram is then used as a tool to determine the failure of the material. The FLDs are widely used because it conveniently offered a way to evaluate the maximum amount of deformation that can take place during a sheet metal forming process before the material becomes plastically unstable. However, The FLDs are not suitable for the application where the material doesn't exhibit a clear necking before fracture [153] as presented in a biaxial test [154] and incremental sheet forming process [155].

As for bending dominated processes such as hemming and air bending, the failure mechanism is not controlled by a necking, because there is no thinning of material along the bending line. Rather, a fracture mechanism governs the failure in these processes. Therefore, ductile fracture is considered as the failure criteria. [147, 153, 156] and numerous DFC have been proposed [146].

In this context, OSM bending is also a process where the failure is governed by fracture. Hence, this study utilizes various DFC to predict the occurrence of a fracture during OSM bending. There are two general categories of ductile fracture criteria (DFC), which are coupled DFC and uncoupled DFC [147, 157]. The coupled DFC models focus on microscopic damage evolution to model fracture. The models are based on nucleation, growth, and coalescence of the crack until fracture.

The uncoupled DFC is phenomenological relation that models the fracture macroscopically. This approach gain popularity due to its simplicity and fewer number of coefficients that need to be determined compared to coupled DFC. Most of the uncouples DFC models use the function form of $\int_0^{\bar{\epsilon}_f} f(\sigma, \bar{\epsilon}) d\bar{\epsilon}$, which represents plastic work [158]. The function, f, involves various stress invariants. The uncoupled fracture criteria state that fracture occurs when accumulated plastic strain reached a critical value.

Based on these facts, uncoupled DFC is used in this study. Among the uncoupled DFC, Cockroft, and Latham [159], Brozzo et al [160], Ayada [161], and Rice and Tracy criteria [162] are chosen, because they need only one parameter to calibrate. The specific forms of these DFC are given in Eq. (7.1)-(7.4). This allows for a relatively easy calibration process.

$$d_1 = \int_0^{\bar{\epsilon}_p^f} \frac{\sigma_1}{\sigma_{eq}} d\bar{\epsilon}_p \tag{7.1}$$

$$d_2 = \int_0^{\bar{\epsilon}_p^f} \frac{2\sigma_1}{3(\sigma_1 - \sigma_{eq})} d\bar{\epsilon}_p \tag{7.2}$$

$$d_3 = \int_0^{\bar{\epsilon}_p^f} \frac{\sigma_h}{\sigma_{eq}} d\bar{\epsilon}_p \tag{7.3}$$

$$d_4 = \int_0^{\bar{\epsilon}_p^f} \exp(\frac{3\sigma_1}{2\sigma_{eq}}) d\bar{\epsilon}_p \tag{7.4}$$

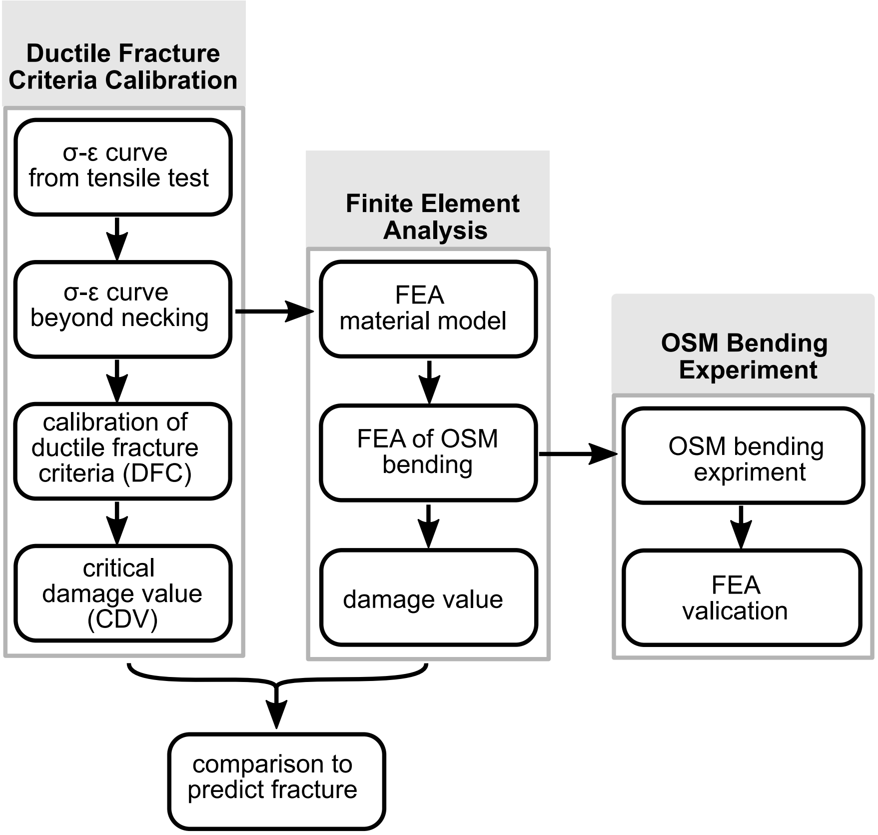

Figure 7.1: Workflow of fracture prediction in OSM bending

where $d_i(i = 1, 2, 3, 4)$) is damage value corresponding to each of these DFC. As can be seen from Eq. (7.1)-(7.4), Cockroft and Latham postulated that fracture is associated with maximum principal stress σ_1, and equivalent stress σ_{eq}. Brozzo and Ayda criterion depends on hydrostatic stress σ_h. Rice and Tracy's criterion has an exponential relation with hydrostatic stress σ_h. For all of these DFC, fracture happens when the parameters d_i reaches a critical damage value (CDV), which is identified from the experiment and FEA.

The complete workflow to predict the fracture in OSM bending is depicted in the flow diagram shown in Fig. 7.1. The workflow consists of three main procedures, which are ductile fracture criteria calibration, finite element analysis of OSM bending, and OSM bending experiment.

In the process of ductile fracture criteria calibration, the stress-strain characteristics of the material beyond necking are identified from a tensile test with help of an iterative finite element process. The calibration provides a CDV for each of the chosen DFC. The CDVs are used as a benchmark to predict fracture in OSM bending

Table 7.1: Scope of the study

MD Type	Scale	Thickness [mm]	Material
MD-1	0.3, 0.5, 1, 1.5, 2	1.6, 2.3, 3.2	Aluminum Alloy 6061-O
MD-2	0.3, 0.5, 0.7		
MD-3	0.2, 0.3, 0.4, 0.5		
MD-5	0.2, 0.3, 0.4, 0.5		

process. Then, finite element simulation of OSM bending is performed to calculate the damage values (DVs) for different types of MDs, different scales, and different thicknesses. Then, DVs are compared against CDVs to determine the possibility of fracture occurring. Lastly, the FEA of OSM bending is experimentally validated by comparing the strain results from FEA to experimental strain measurement at the outer surface of the sheet.

In this study, four different MDs are selected for investigation from the available MDs shown in Fig. 1.1. They are MD-1, MD-2, MD-3, and MD-5. Considering the fact that each MD may fracture at a different scale, a different set of scales is chosen for each MD as listed in Table 7.1. Three-level of thicknesses are taken into consideration to determine if the same scale causes fracture at a different thickness. The material used for the study is aluminum alloy 6061 temper O, denoted as AA-6061-O below.

7.3 Calibrating DFC

7.3.1 Determining the stress-strain curve beyond necking

Here the calibration process of DFC refers to the process of determining the two items. The first is the stress-strain curve of AA-6061-O prior to necking as well as post necking. The second is CDVs for the chosen DFC listed in Eq. (7.1)-(7.4). This procedure is completed with a tensile test and iterative FEA. The steps of calibrating DFC are outlined below:

1. A uniaxial tensile test is performed on AA-6061-O until fracture. During the test, force-displacement data was collected. The stress-strain characteristics until necking is obtained from the test.
2. The post necking stress-strain values are estimated based on the weighted average method [163]. The stress-strain values until fracture are fed into FEA to define the material model for AA-6061-O.

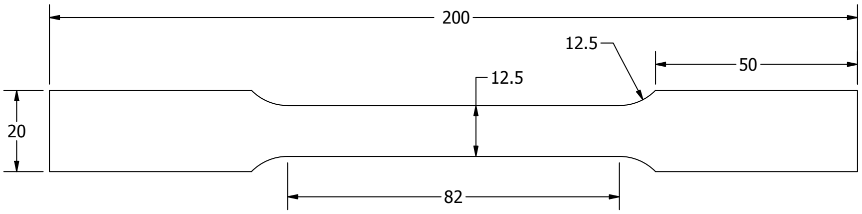

Figure 7.2: Tensile test specimen

3. FEA of the tensile test is performed iteratively until the force-displacement from FEA matches that of the uniaxial tension test in step 1.
4. The critical damage values are calculated for the chosen DFC.

During the uniaxial tensile test, the sheet type specimen along the rolling direction of the material is prepared according to the ASTM standard [139] with the dimension shown in Fig. 7.2. The specimen thickness is 14 gauge (1.6 mm). In the test, the elongation of the specimen is controlled by the speed of the loadcell motion. Prior to the yielding of the specimen, the speed of the loadcell is set to 1.23 mm/s. It is changed to 10 mm/s for post-yield. The tensile test is carried on Instron universal tensile testing machine 3369. Load, extension data is collected from the test.

FEA of the tensile test is performed using Ansys ®19 R1 implicit scheme. Since the bending happens along the rolling direction of sheet metal, anisotropy was not considered in the FEA. The material is assumed to obey Von Mises yield criteria and associated flow rule. The plasticity model for AA-6061-O is elastic-plastic with multi-linear isotropic hardening. Due to symmetry, one-fourth of the sample was stimulated by considering only half-width and thickness. The symmetry boundary condition was applied along the length and thickness of the specimen. One end of the sample is fixed, and a displacement load is applied on the other end. The magnitude of the displacement load is 20.8 mm, which is the same displacement measured from the tensile test at fracture. It was assumed that fracture happens in the simulation when the displacement reaches the same value, 20.8 mm. To ensure the necking happens at the center of the specimen, a tiny defect is introduced. The specimen geometry is discretized with linear 8-node Hexa-elements. Mesh size at the center was much finer and it is gradually coarsened towards two ends of the sample.

The stress-strain relationship prior to necking is obtained from the recorded load-displacement data in the tensile test. The stress-strain relationship beyond necking is estimated with a process, named the weighted average method [163]. The

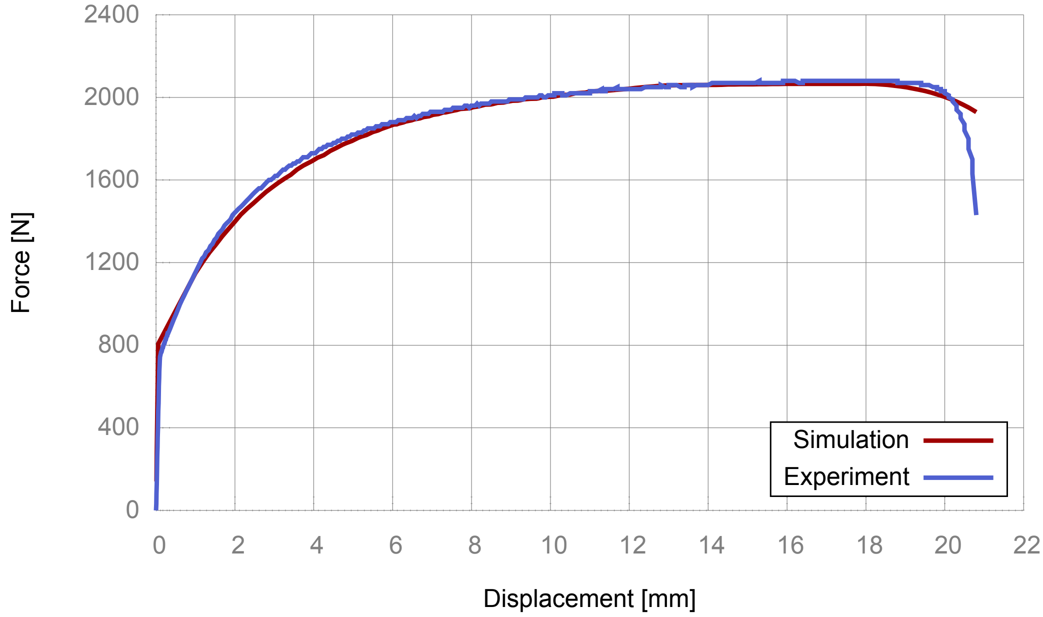

Figure 7.3: Force-displacement curve from tensile test and FE simulation

weighted average method uses Eq. (7.5) iteratively to determine the stress-strain relationship beyond necking.

$$\sigma = \sigma_u[w(1 + \epsilon - \epsilon_u) + (1 - w)(\frac{\epsilon}{\epsilon_u})^{\epsilon_u})] \tag{7.5}$$

where σ is true stress, σ_u is ultimate true stress, ϵ is the true strain, ϵ_u is the ultimate true strain, w is the weight factor.

As the stopping criteria for the iteration, the force-displacement data from the tensile test simulation is compared to experimental force-displacement data. The simulation is repeated until it matches the experimental force-displacement curve. After trial and error, w is identified to be 0.865. The final force-displacement curve matching the tensile test most closely is shown in Fig. 7.3. The identified stress-strain data in Fig. 7.4 is then provided as input for the multilinear isotropic hardening material model of AA-6061-O in the OSM bending simulations.

7.3.2 Calculating critical damage values for DFC

The CDVs for the four DFC are calculated from the tensile test FE simulation. The CDVs corresponds to the accumulated damage value of the material until fracture. For each increment of the load step in the simulation, the necessary fields such as the maximum principle stress, equivalent stress, hydrostatic stress, and equivalent plastic strain, are extracted using an Ansys APDL code. The extracted

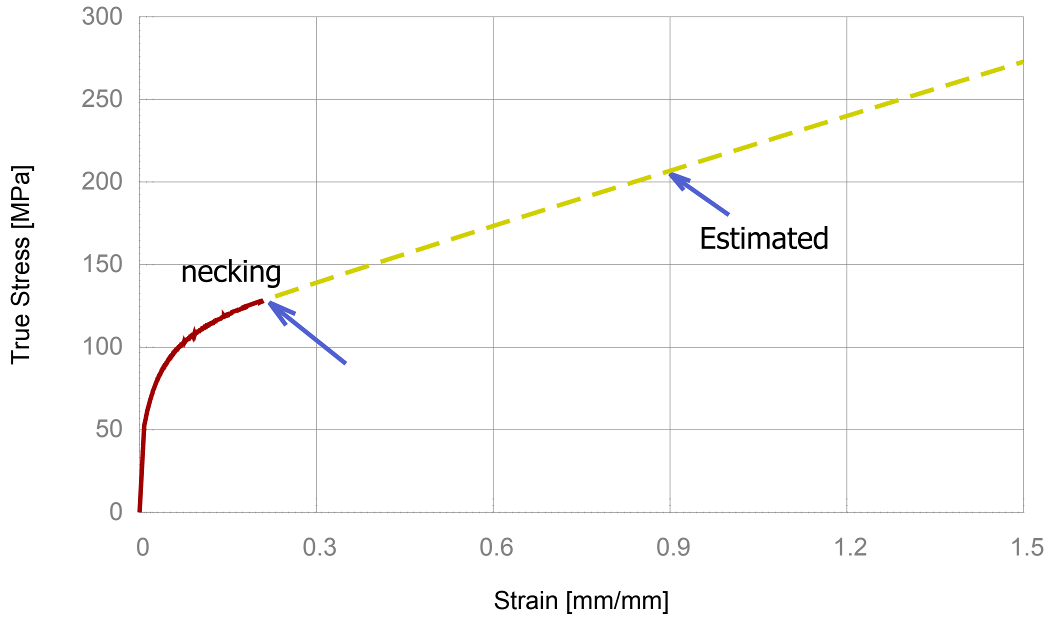

Figure 7.4: Stress-Strain curve extended by weighted average method. This curve is used as input to AA-6061-O material model definition in FEA

field data is then used to integrate according to Eq. (7.1)-(7.4). The integration is performed using the trapezoid integration rule in Matlab. The CDV at fracture from the Cockroft-Latham criterion is d_1=0.607. Similarly, the CDVs from Brozzo, Adaya, Rice-Tracy are d_2=0.6107, d_3=0.214, d_4=1.017, respectively.

7.4 FE simulation of OSM bending

Series of FE simulations are performed to calculate the damage values of MDs under different scale and thickness. The simulation is set up in the configuration identical to the setup shown in Fig. 1.2. Taking all MD types, scales, and sheet thickness listed in Table 7.1 into account, there are 48 cases in total as tabulated in Table 7.2. The case name in Table 7.2 starts with a MD type followed by the thickness of the sheet, then the scale of the MD is indicated by "k-t", and a number representing the scale. All OSM bending simulations uses the same configuration parameters, i.e., g=23 mm, s=3mm, R_p=3 mm, where g is the gap between the punch and edge of the support (blank holder), s is the offset distance, R_p is the punch radius.

The sheet size is 50 (mm) × 50 (mm). The MDs are applied in the middle of the sheet. As an example, the dimensions for the sheet and MDs are illustrated for the scale of 0.3 in Fig. 7.5.

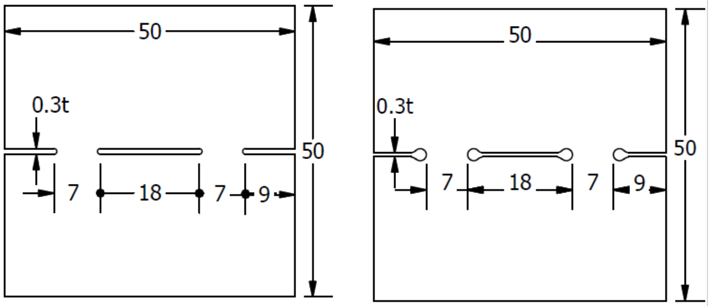

(a) MD-1 (b) MD-2

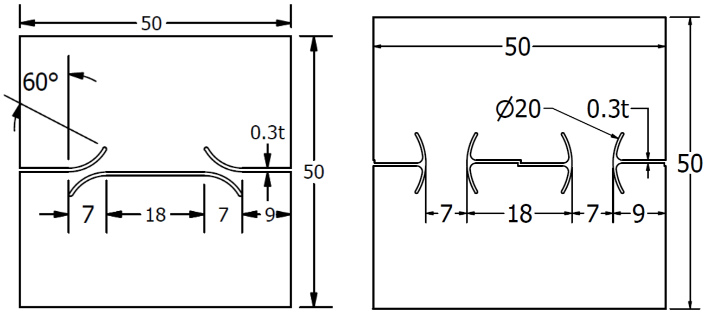

(c) MD-3 (d) MD-5

Figure 7.5: Dimensions of the sheet and MDs with scale of 0.3

In the simulation, the punch, the support, and the blank holder are modeled as rigid bodies. The sheet is modeled as a deformable flexible body. Four-node rectangular element is used for all rigid bodies in the FE model. The blank sheet is discretized with 20 node Hexa-dominant elements. The deformation of the sheet obeys von Mises yield criteria and associated flow rule. A multilinear hardening plasticity material model determined from the tensile test simulation is assigned to the sheet. A friction coefficient of 0.12 is considered between the sheet and all rigid bodies. The OSM bending process is simulated in two load steps. The first load step is to apply a pressure load on the blank holder to hold the sheet in the correct position during the bending process. The second load step is to apply a displacement load on the punch along with horizontal and vertical directions to bent it to 90°.

7.5 Experimental validation of finite element simulation

An OSM bending device as shown in Fig. 7.6 is designed in order to validate the simulation results. The bending device consists of a base, sheet holder, bending bar, mounting column, and a pair of rotating links. The base is connected to the mounting column, which is used to position the whole device in a fixture. On top of the base, there is a 1 mm deep slot that precisely matches the width of the sheet. The slot also ensures the sheet is placed with a 3 mm offset distance (s). The base

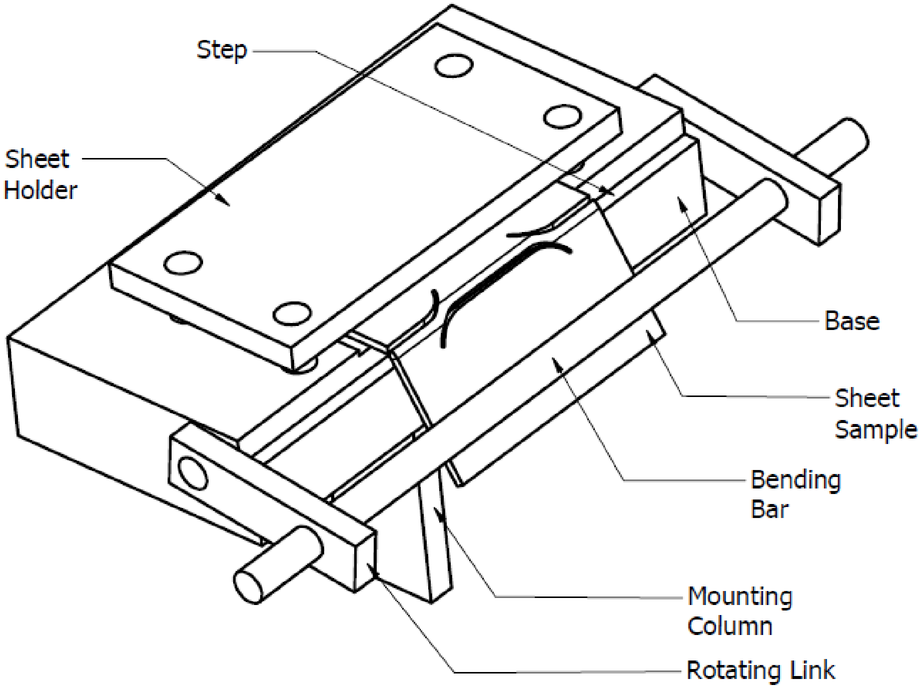

Figure 7.6: OSM bending device

also has a step at the front that guarantees the bending stops at 90°.The sheet holder is placed on top of the sheet sample. The sheet holder fixes the sheet sample through four screws connected to the base. A bending bar is transversely connecting a pair of rotating links that can rotate freely. The bending takes place with the guide of rotating links once the bending bar starts pressing the sheet.

In the OSM bending experiment, equivalent strain occurred on the surface of the OSM sample is analyzed. The trend of equivalent strain is evaluated over the entire duration of 90° bending. The trend of equivalent strain variation over the bending angle is then compared to the trend obtained from the FEA of OSM bending.

Six different cases are selected among the 48 cases listed in Table 7.2. They are case No. 5, 10, 18, 21, 36, and 40, respectively. These cases are chosen based on two rules. First, they cover different thicknesses. The second is to select the largest scale among all scales investigated for each MD in order to increase testing data acquisition accuracy. The reason for selecting the largest scale is that the DIC system computes the deformation on a surface component visible to its cameras. Hence, the creation of surface components in the DIC is of crucial importance to the accuracy of the analysis. Often the surface component is a continuous surface area on a test sample, and the DIC can analyze a continuous surface component quite accurately given all the other parameters are selected properly. However, the DIC lacks accuracy when the surface component is non-continuous. MDs profiles come under the non-continuous category. Therefore, we are faced with challenges in accurately capturing the MD profile as it is on the real test sample. When creating a surface component on the sheet that contains MDs, it is hard, if not possible, to ensure the identical profile is traced as the MDs profile on the real sample. Therefore, to minimize the data loss in the critical area of interest, the largest scale of MDs from the investigated scales is selected.

The OSM bending process is carried out manually. Images of the OSM sheet surface is captured by the DIC system with a frequency of four images per second. The equivalent strain field from the images is then computed on the surface of the samples. Then the maximum equivalent strain on the surface is evaluated with respect to the bending angle. A comparison is made between the experiment and FEA in terms of equivalent strain magnitude variation over the bending angle, as shown in Fig. 7.7 - Fig. 7.12 . The trend of maxim equivalent strain and bending angle appears to be a linear relationship. This is due to the assumption in the implicit scheme that a quasi-static state is assumed for the deformation. Thus, the strain and bending angle change uniformly with respect to time following the same trend. This leads to a linear relationship between the strain and the bending angle. The same linear relationship is also proved and captured in the experiment, where the curves are mostly linear except for some deviations due to noise and equipment error. Good repeatability is observed when the same case is tested twice. The results can be seen in Fig. 7.13 and Fig. 7.14.

The comparison revealed that FEA is in good agreement with the experiment in general. There are two sources of the discrepancy. Firstly, the noise in the DIC system caused fluctuation in the magnitude of the equivalent strain. The noise depends on stochastic paint quality on the sheet and ambient light. It also comes from the fact that the bending is manually performed, and the movement of the sheet is hard to avoid. Secondly, FEA overestimates the equivalent strain magnitude at a larger angle. The reason is due to the manual creation of surface comment, where the maximum equivalent strain occurs. The manual creation of the surface component is not the best representation of the MD profiles. Considering all these factors, FEA yields a very good agreement with the experiment.

7.6 Fracture prediction in OSM bending

The Possibility of fracture occurring is evaluated from the FE simulation of OSM bending. Related stress, strain fields are extracted, and DVs are calculated for all the cases following the same approach used to calculate CDVs for the tensile test. Table 7.2 tabulated the DVs for all 48 cases based on the selected four DFC. Fracture is predicted to occur when the DVs of an OSM bending case is equal to or greater than CDVs obtained from the tensile test. Bar charts in Fig. 7.18 - Fig. 7.15

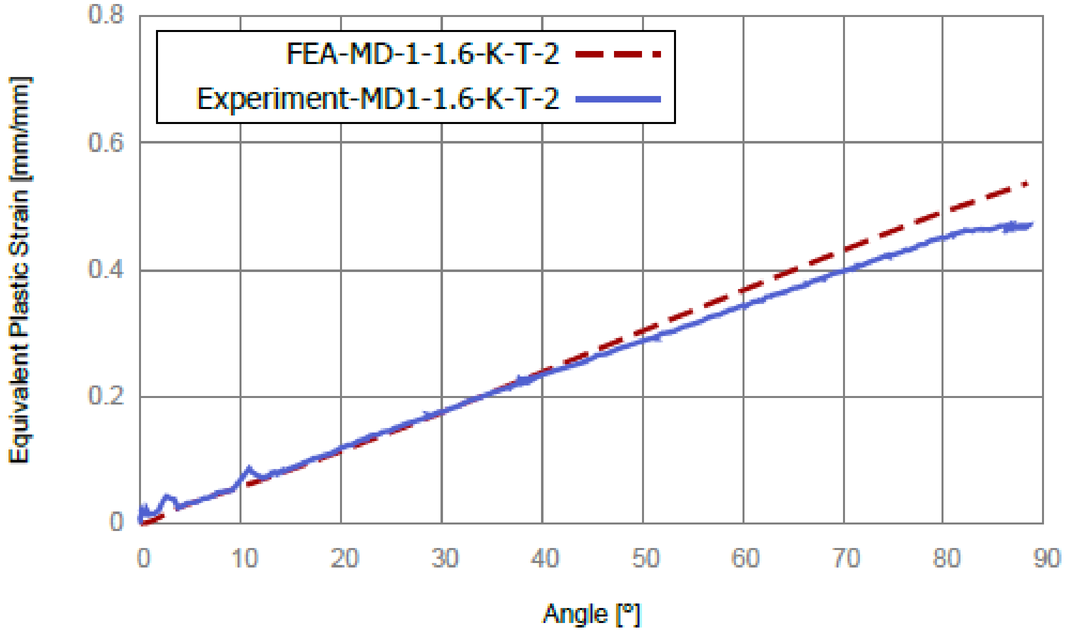

Figure 7.7: FEA validation for case No.5 (MD-1-1.6-K-T-2)

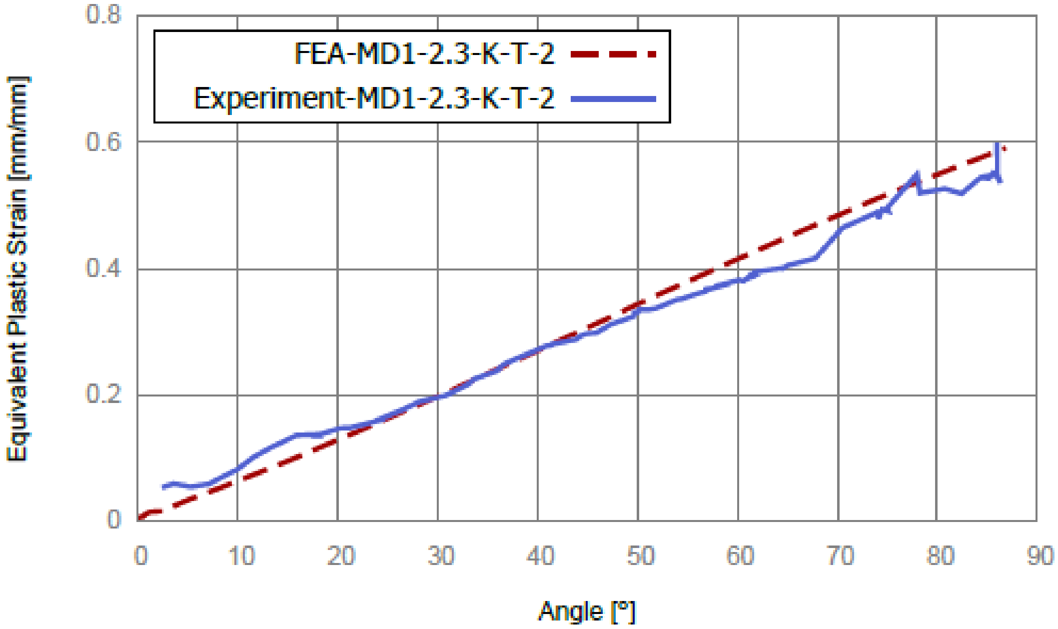

Figure 7.8: FEA validation for case No.10 (MD-1-2.3-K-T-2)

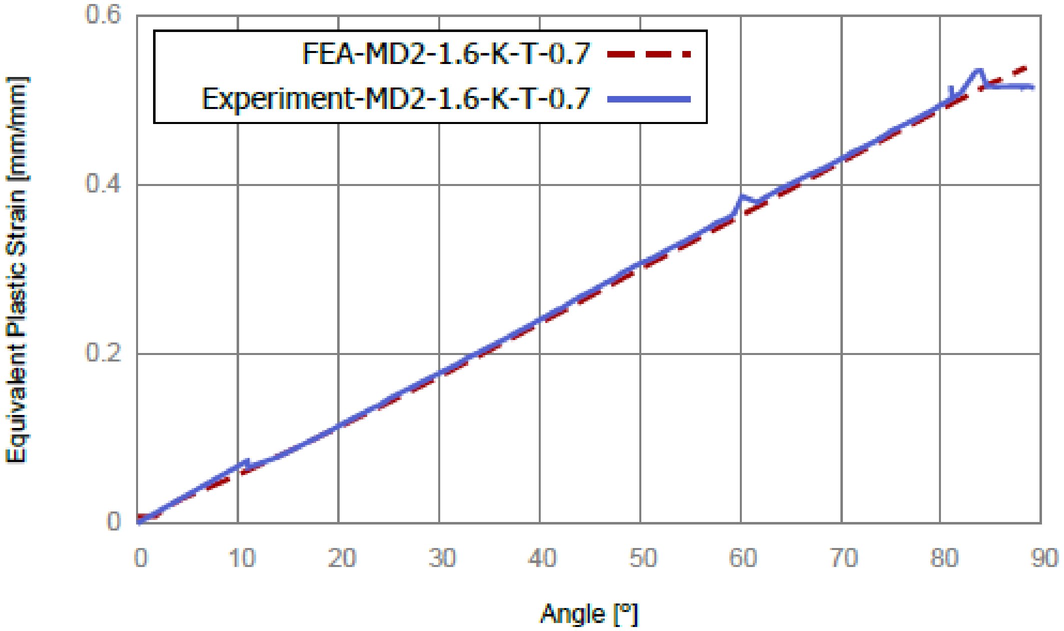

Figure 7.9: FEA validation for case No.18 (MD-2-1.6-K-T-0.7)

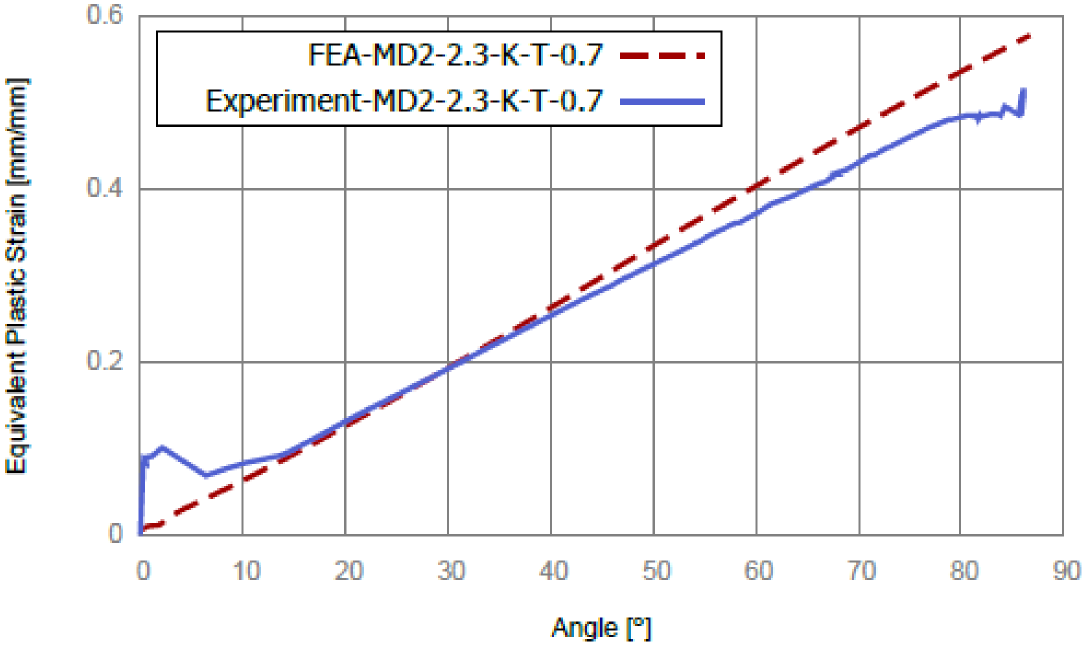

Figure 7.10: FEA validation for case No.21 (MD-2-2.3-K-T-0.7)

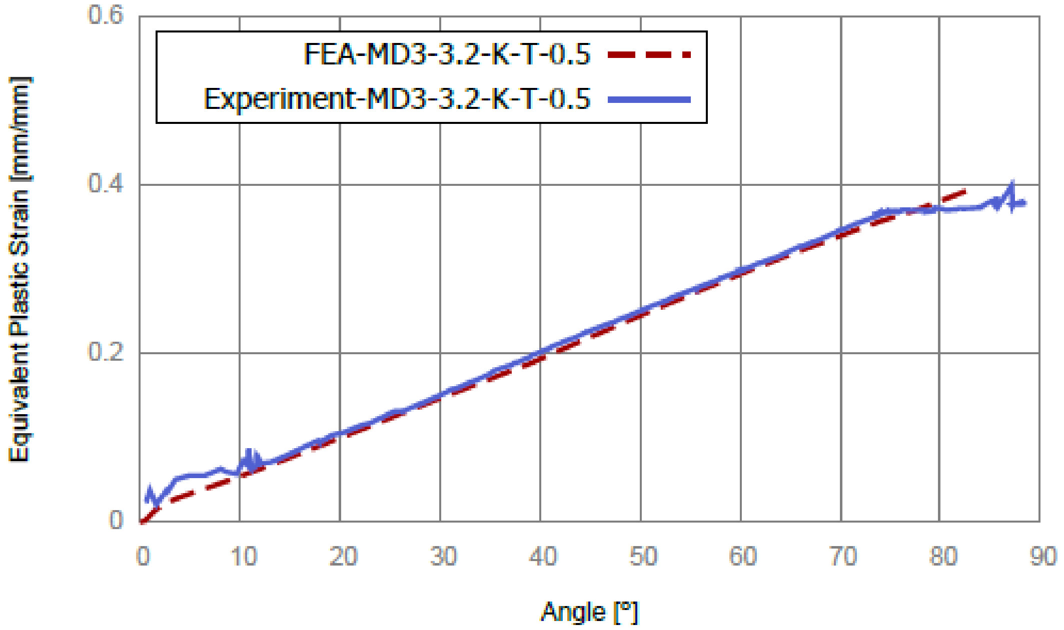

Figure 7.11: FEA validation for case No.36 (MD-3-3.2-K-T-0.5)

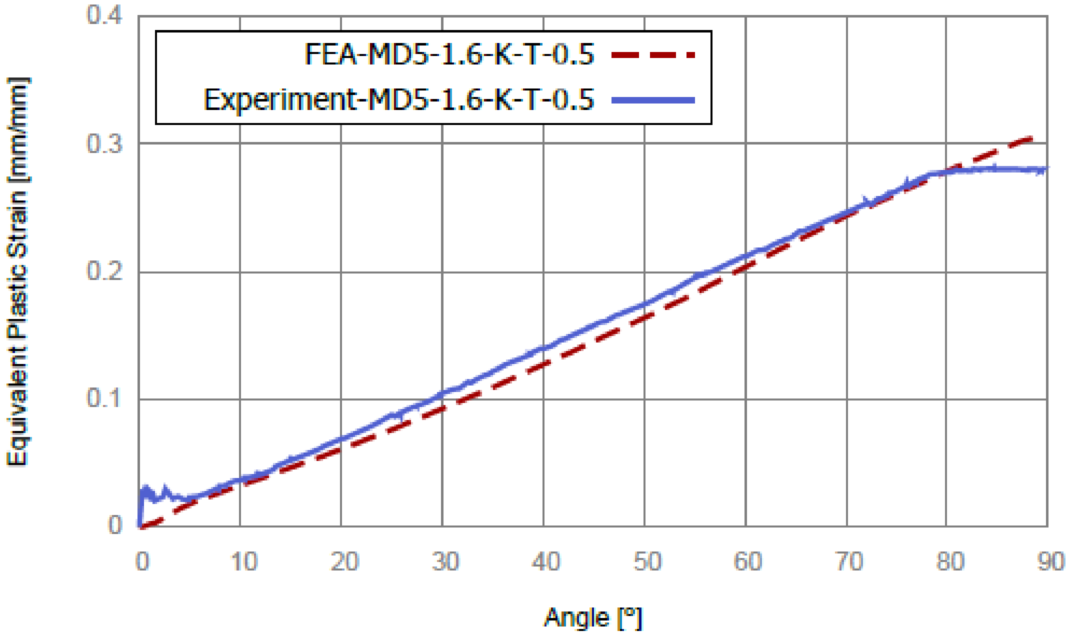

Figure 7.12: FEA validation for case No.40 (MD-5-1.6-K-T-0.5)

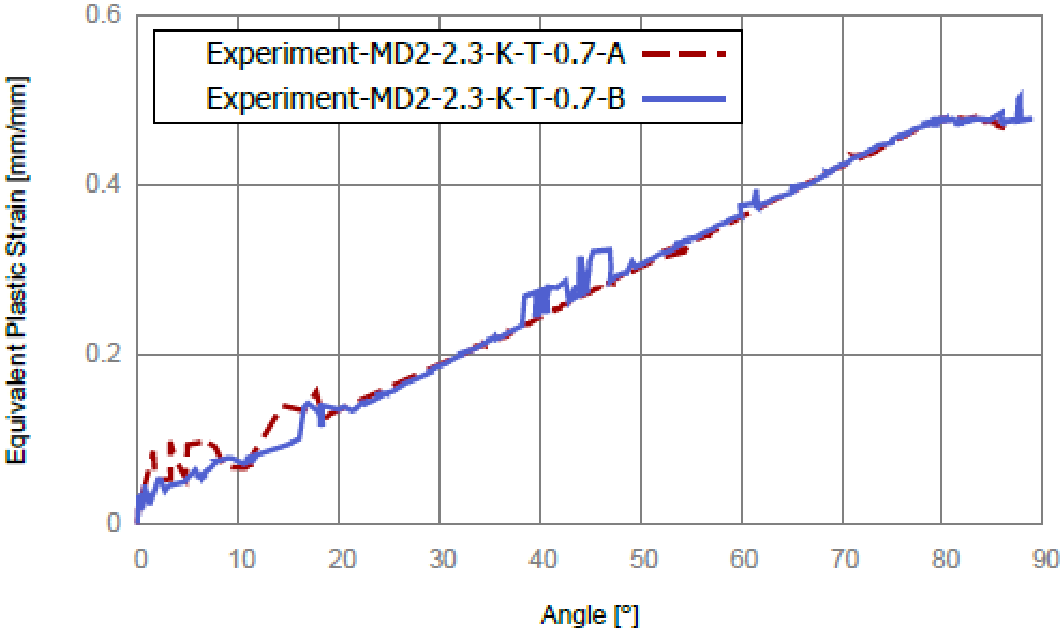

Figure 7.13: Repeatability of experiment case No.18 (MD-2-2.3-K-T-0.7)

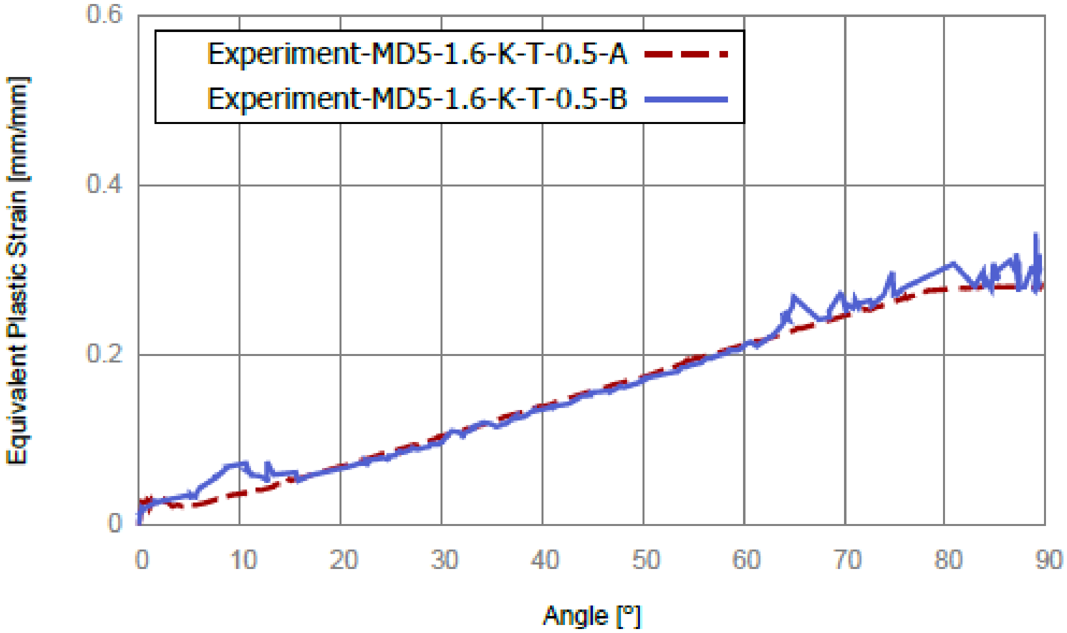

Figure 7.14: Repeatability of experiment case No.40 (MD-5-1.6-K-T-0.5)

show the prediction case by case. In the bar chart, a horizontal line representing the CDV based on a selected DFC is added to indicate the benchmark, which aids in identifying the fracture cases conveniently.

Table 7.2: Case studies and damage values

Case		Thickness [mm]	Scale	Damage Values			
No.	Name			Cockfront & Latham	Brozzo	Ayady	Rice &Tracy
1	MD1-1.6-k-t-0.3	1.6	0.3	1.3418	1.349	0.4898	2.2487
2	MD-1-1.6-k-t-0.5		0.5	1.0483	1.054	0.3635	1.7472
3	MD-1-1.6-k-t-1		1	0.7445	0.7484	0.2522	1.2326
4	MD-1-1.6-k-t-1.5		1.5	0.6142	0.6174	0.2061	1.0145
5	MD-1-1.6-k-t-2		2	0.537	0.5398	0.1795	0.8861
6	MD-1-2.3-k-t-0.3	2.3	0.3	1.3605	1.3676	0.486	2.2751
7	MD-1-2.3-k-t-0.5		0.5	1.0763	1.0819	0.3685	1.7873
8	MD-1-2.3-k-t-1		1	0.7775	0.7814	0.2608	1.284
9	MD-1-2.3-k-t-1.5		1.5	0.6558	0.6592	0.2191	1.082
10	MD-1-2.3-k-t-2		2	0.5909	0.5939	0.1971	0.9743
11	MD-1-3.2-k-t-0.3	3.2	0.3	1.3741	1.381	0.4804	2.2802
12	MD-1-3.2-k-t-0.5		0.5	1.1251	1.1308	0.3829	1.8651
13	MD-1-3.2-k-t-1		1	0.8376	0.8418	0.2801	1.3821
14	MD-1-3.2-k-t-1.5		1.5	0.7251	0.7287	0.2416	1.1953
15	MD-1-3.2-k-t-2		2	0.6416	0.6448	0.2134	1.0573
16	MD-2-1.6-k-t-0.3	1.6	0.3	0.7987	0.803	0.272	1.3244
17	MD-2-1.6-k-t-0.5		0.5	0.6282	0.6315	0.2115	1.0385
18	MD-2-1.6-k-t-0.7		0.7	0.5405	0.5433	0.1813	0.8926
19	MD-2-2.3-k-t-0.3	2.3	0.3	0.8169	0.8211	0.2667	1.3526
20	MD-2-2.3-k-t-0.5		0.5	0.661	0.6644	0.2217	1.0917
21	MD-2-2.3-k-t-0.7		0.7	0.5794	0.5823	0.1936	0.9559
22	MD-2-3.2-k-t-0.3	3.2	0.3	0.8656	0.8701	0.2936	1.4337
23	MD-2-3.2-k-t-0.5		0.5	0.7143	0.718	0.2401	1.1804
24	MD-2-3.2-k-t-0.7		0.7	0.6444	0.6477	0.2209	1.063

25	MD-3-1.6-k-t-0.2	1.6	0.2	0.2304	0.2316	0.0744	0.377
26	MD-3-1.6-k-t-0.3		0.3	0.2313	0.2325	0.075	0.3789
27	MD-3-1.6-k-t-0.4		0.4	0.2534	0.2548	0.0809	0.414
28	MD-3-1.6-k-t-0.5		0.5	0.2475	0.2489	0.078	0.403
29	MD-3-2.3-k-t-0.2	2.3	0.2	0.3443	0.3461	0.1127	0.5652
30	MD-3-2.3-k-t-0.3		0.3	0.3407	0.3424	0.1109	0.5585
31	MD-3-2.3-k-t-0.4		0.4	0.2886	0.2901	0.0935	0.4726
32	MD-3-2.3-k-t-0.5		0.5	0.3223	0.324	0.1043	0.5277
33	MD-3-3.2-k-t-0.2	3.2	0.2	0.4736	0.476	0.1566	0.78
34	MD-3-3.2-k-t-0.3		0.3	0.4649	0.4673	0.1533	0.7645
35	MD-3-3.2-k-t-0.4		0.4	0.4231	0.4252	0.1389	0.695
36	MD-3-3.2-k-t-0.5		0.5	0.3948	0.3968	0.1291	0.648
37	MD-5-1.6-k-t-0.2	1.6	0.2	0.3029	0.3044	0.1276	0.5291
38	MD-5-1.6-k-t-0.3		0.3	0.3034	0.305	0.127	0.5265
39	MD-5-1.6-k-t-0.4		0.4	0.3044	0.3059	0.1265	0.5251
40	MD-5-1.6-k-t-0.5		0.5	0.3035	0.305	0.1272	0.5272
41	MD-5-2.3-k-t-0.2	2.3	0.2	0.3911	0.3931	0.1621	0.676
42	MD-5-2.3-k-t-0.33.2		0.3	0.3914	0.3933	0.1623	0.6772
43	MD-5-2.3-k-t-0.4		0.4	0.3928	0.3948	0.162	0.6762
44	MD-5-2.3-k-t-0.5		0.5	0.3941	0.3961	0.1638	0.6835
45	MD-5-3.2-k-t-0.2	3.2	0.2	0.4883	0.4908	0.2002	0.8439
46	MD-5-3.2-k-t-0.3		0.3	0.4884	0.4908	0.1997	0.8428
47	MD-5-3.2-k-t-0.4		0.4	0.4885	0.491	0.2	0.8431
48	MD-5-3.2-k-t-0.5		0.5	0.4892	0.4916	0.2004	0.846

7.6.1 Effect of scale

Different numbers of scales are evaluated for each type of MD. The results exhibited two different trends. The first trend is that the larger the scale is, the less likely a fracture occurs. This can be clearly seen from the predictions for MD-1 and MD-2 shown in Fig. 7.15 and Fig. 7.16. All four DFC followed the same pattern on the change of Scale. It is clearly seen that the increase of the scale results in a

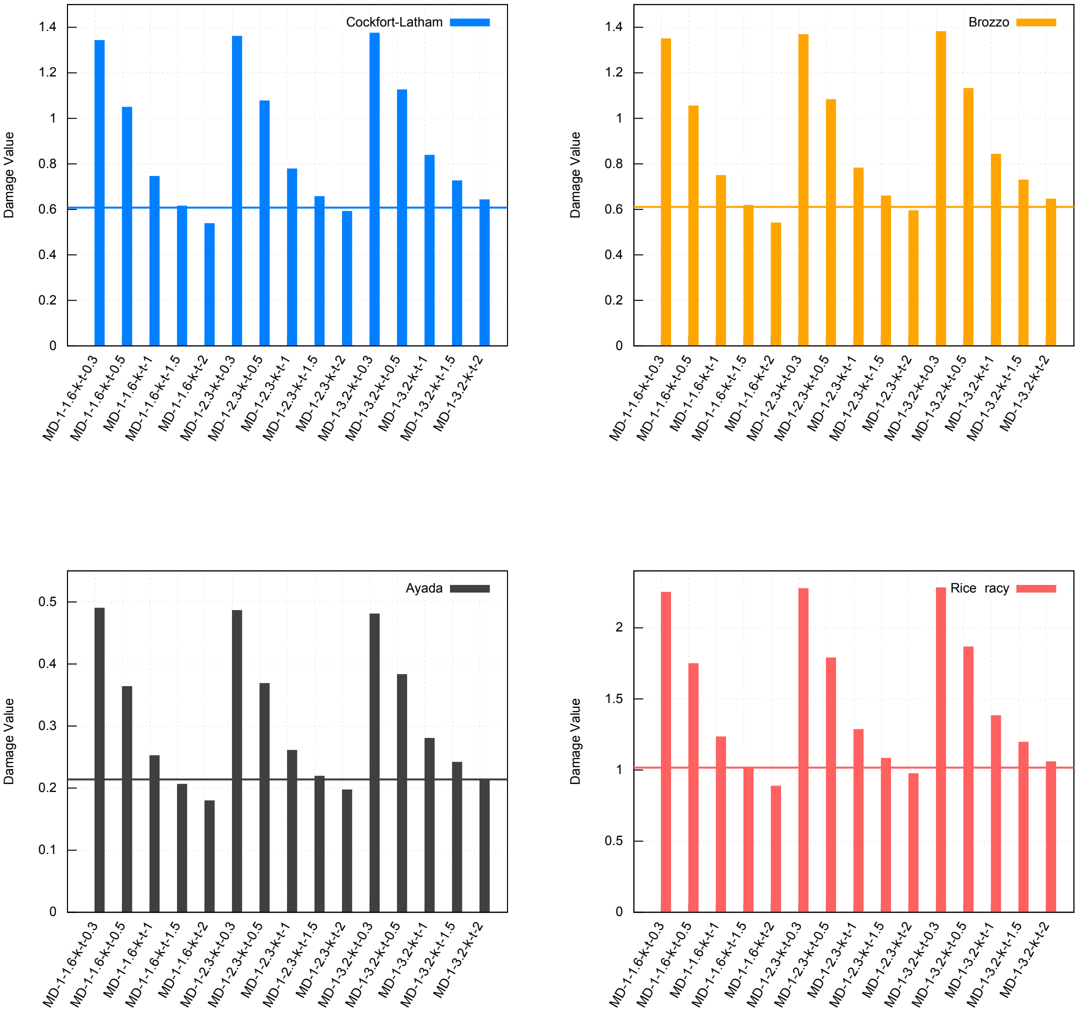

Figure 7.15: Fracture prediction on MD-1

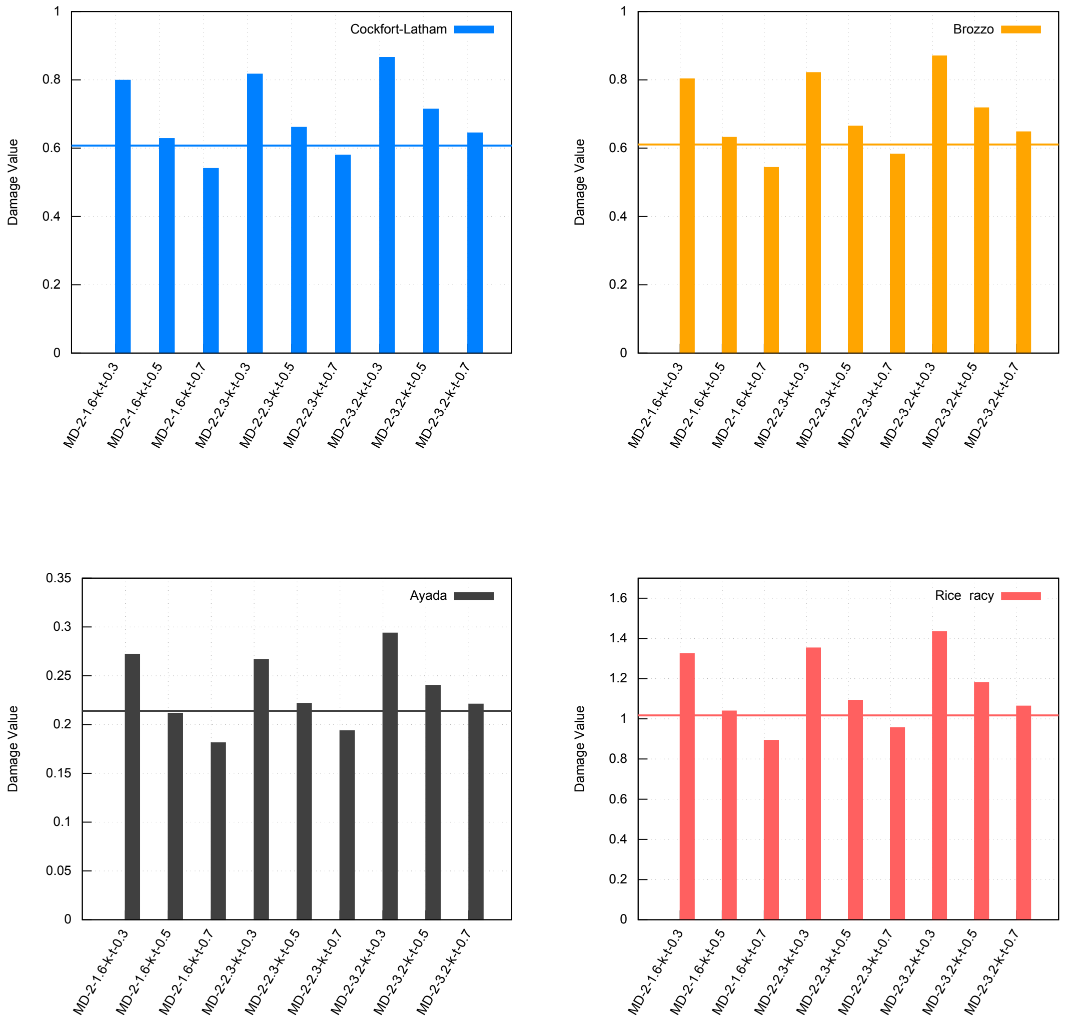

Figure 7.16: Fracture prediction on MD-2

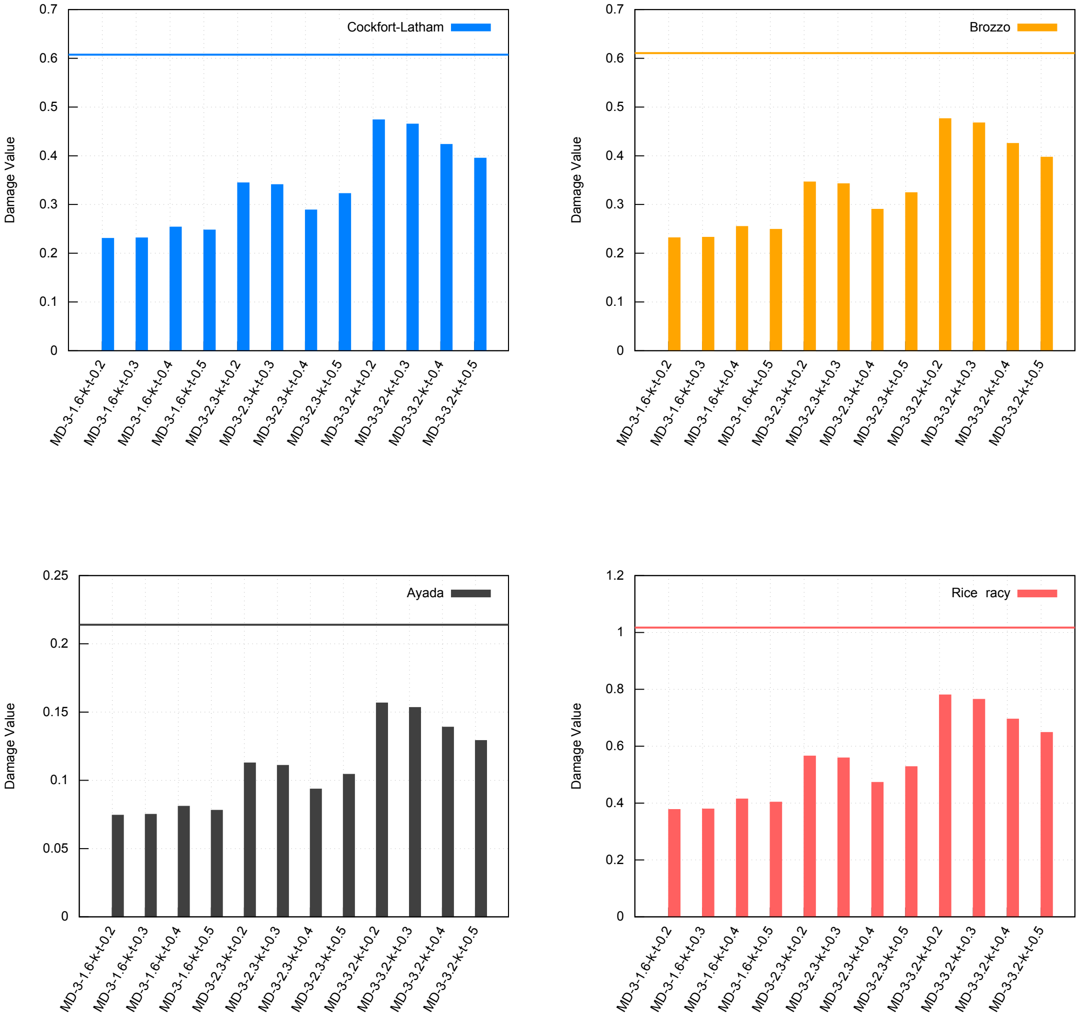

Figure 7.17: Fracture prediction on MD-3

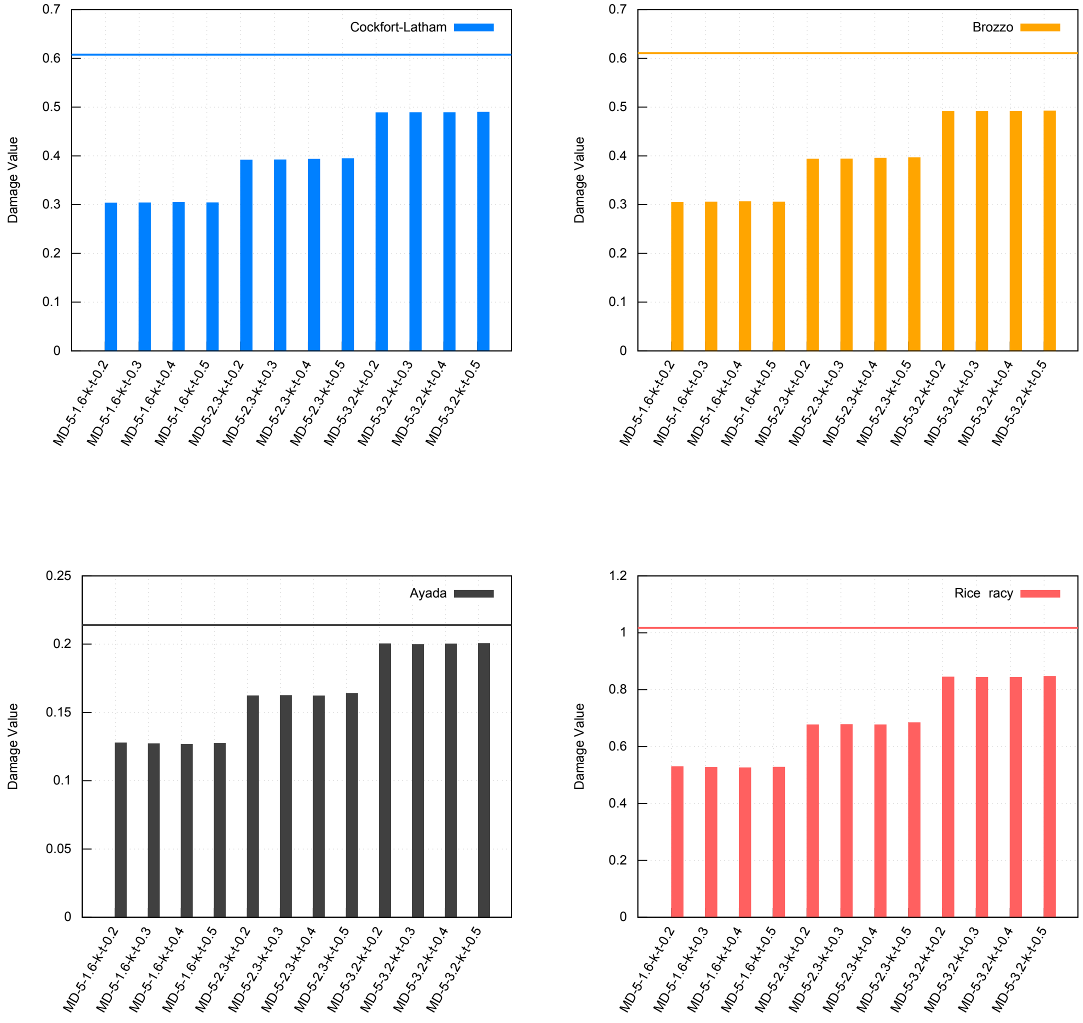

Figure 7.18: Fracture prediction on MD-5

drop in the DVs, and gradually the DVs go under the safe zone below the CDVs. The second trend is exhibited on MD-3 and MD-5 as shown in Fig. 7.17 and Fig. 7.18, where the DVs stay constant regardless of changes on the scale. Even though there is some fluctuation on MD-3, it is not as large as the fluctuation observed on MD-1, and MD-2.

The reason for the two different trends is related to the size of the curvature radius on MDs. On MD-1 and MD-2, the curvature radius is significantly smaller than that of MD-3, and MD-5. Small curvature radius can because of stress concentration leading to fracture. Hence, a change on the scale of MD-1, and MD-2 generate a large shift in DVs, whereas, in MD-3 and MD-5, the scale doesn't result in a change of DVs.

The results also yield the limit scale for the MDs, beyond which a fracture can occur. For sheets with a MD-1, a scale of 2 is the limit scale when the thickness is less than 2.3 mm because a fracture is predicted when the thickness is 3.2. For sheet with MD-2, a scale of 0.7 is the safe scale when the thickness is equal to or less than 2.3 mm. The reason for MD-2 can tolerate a much smaller scale is due to the opening at the end of the MD-2.

For MD-3, and MD-5, all scales investigated don't give rise to a fracture regardless of the thickness. MD-3 and MD-5 can be applied with a scale as small as 0.2. These two MDs are good choices for small scales.

7.6.2 Effect of sheet thickness

The thicker the sheet thickness, the more likely a fracture happens during the OSM bending. This trend is evident regardless of the MD type investigated in this study. This can be explained by the fact the DVs are plastic work done to the sheet [158]. The thicker the sheet, the more work it requires to be bent to the same extend. This implies that a smaller scale can be combined with a thinner thickness to obtain a balanced choice for the design.

7.7 Summary

The tensile test on the AA-6061-O sheet of 1.6 thickness is performed in order to calibrate four DFC. The calibration provided a set of benchmarks in terms of damage values to predict the possibility of fracture in OSM bending. The damage values are obtained from the FEA of OSM bending. The tensile test simulation is validated using the experimental force-displacement curve, whereas the OSM bending simulation is validated using strain measurement from OSM bending experiments. Four different MDs, three different thicknesses are investigated with the combination of numbers of scales. The results reveal that the higher the scale, the more fracture-proof the MD is, because a small scale is associated with a small radius of curvature on MDs. It is also observed that the MDs are more likely to fracture on a thicker sheet than it does on a thinner sheet. The investigation also provided a safe scale for the MD studied in this work. The investigation can be extended to different types of materials, MDs, and thicknesses in order to cover various design requirements.

Chapter 8

CONCLUSION

The research conducted in this dissertation expanded the origami concept from a manufacturing point of view, and from a mechanics point of view. Particularly, this research focused on various aspects of OSM bending in light of mechanics and sheet metal forming.

The following summarizes my contribution in the context of sheet metal forming:

- We showed that the OSM sheet can reduce bending force, increase bending accuracy in a conventional bending setup–wiping die bending.
- We conceptualized the OSM bending process by defining a set of parameters related to the OSM sheet and the bending process. OSM bending revealed the feasibility of a dieless bending, which is significant advantage of OSM bending over the conventional bending processes.
- We identified a set of design and process parameters in the OSM bending process. The design parameters are related to the design of OSM sheet, and MD. The process parameters are associated with the bending process itself. These parameters are kerf-to-thickness (k/t) ratio, web-to-width (w/b) ratio, sheet thickness (t), offset distance (s), punch placement (g), and punch radius (R_p).
- Impact of the identified parameters are evaluated. The results show that the stress generated along the bend line is caused by the size of the curvature radius at the end of a specific MD. A larger k/t ratio should be selected in order to have less stress concentration after bending. For achieving reduced bending force, a smaller web-to-width (w/b) ratio , a larger punch placement (g), and a thinner sheet is recommended. It is found that high accuracy of bending along the predetermined bending line can be guaranteed by selecting a smaller offset distance (s).
- We presented a bending force perdition model for OSM bending. This model takes mechanical property of the material, type of MDs, sheet thickness, and

bending angle as input. It revealed that each MD has a unique shape factor dictating the influence on the magnitude of the bending force. This model provides an easy tool to estimate OSM bending force.

- We identified behavior of MDs under tension and shear load. It shows that the behavior of MDs under these loads depend on how the effective cross section changes during the loading. The study also presented a simple approach to predict failure in the OSM bending process using simple testing methods such as tension test, and shear test.

- We discovered that success of an OSM bending operation is largely affected by the MDs applied on the sheet, particularly by the scale of MDs. Hence, a systematic approach to predict fracture occurrence caused by the scale of the MD during the OSM bending is presented. It showed a critical scale for MDs to avoid fracture. Interestingly, the critical scale depends on the MD profile, and curvature at the end of the MD. Considering the topological similarity between MD-1 and MD-2, It shows that MD-2 with a larger opening would help prevent the fracture. MD-3 and MD-5 are generally fracture-proof as they didn't exhibit any fracture for the range of scales and thickness investigated.

- This dissertation also showed that topology of MDs are critical aspect of the OSM bending process. The topology affects the stress concentration level, fracture occurrence, accuracy of bending. The MD topology is cause of failure, stress concentration. At the same time, improving the topology also brings the solution to the problems. Therefore, selecting a proper MD topology is important.

Future work

This research can be extended in the following areas/direction.

- The force prediction model proposed can be extended from the three MDs to other MD types and material types. A statistical or artificial intelligence based approach can be used to strengthen the accuracy of the model with more tests on variety of MDs and materials.

- Sheet metal bending occurs in many forms. In this dissertation, a bending form that bends along a straight line is considered. Therefore, a bending configuration along a curved bending line can be investigated based on what has been discovered in this work. The curved bending of sheet metal is can be categorized into flanging.

- This work considered only 90° bending angle for OSM bending. The study can be extended to larger angle of bending. For instance, when the bending angle reaches to 180° it becomes a hemming operation. In this case, the bending setup used in this work may not be suitable any more. Besides, additional parameters may impact the large angle bending with OSM. Hence, identification of these parameters and feasibility of large bending angle leading to a hemming operation can be investigated.

- This work can be extended to investigate performance of structures formed by OSM bending under various loading scenarios. For instance, adaptive structures, sandwich structure that are constructed or formed from OSM bending operation.

BIBLIOGRAPHY

[1] K. A. Tolman, E. G. Merriam, L. L. Howell, Compliant constant-force linear-motion mechanism, Mechanism and Machine Theory 106 (2016) 68–79. URL http://dx.doi.org/10.1016/j.mechmachtheory.2016.08.009

[2] N. De Temmerman, Design and analysis of deployable bar structures for mobile architectural applications, Ph.D. thesis, Vrije Universiteit Brussel (2007). URL http://www.vub.ac.be:8080/phd/verdedigingen2007/200706282a.pdf

[3] J. Morgan, S. P. Magleby, L. L. Howell, An Approach to Designing Origami-Adapted Aerospace Mechanisms, Journal of Mechanical Design 138 (5) (2016) 052301.

[4] Q. Shi, X. Shi, J. M. Gattas, S. Kitipornchai, Folded assembly methods for thin-walled steel structures, Journal of Constructional Steel Research 138 (2017) 235–245.

[5] K. C. Cheung, T. Tachi, S. Calisch, K. Miura, Origami interleaved tube cellular materials, Smart Materials and Structures 23 (2014) 1–10.

[6] J. L. Silverberg, A. A. Evans, L. McLeod, R. C. Hayward, T. Hull, C. D. Santangelo, I. Cohen, Using origami design principles to fold reprogrammable mechanical metamaterials, Science 345 (2014) 647—-650.

[7] R. J. Lang, T. Nelson, L. Howell, S. Magleby, Thick Rigidly Foldable Origami Mechanisms, in: ASME 2016 International Design Engineering Technical Conferences & Computers and Information in Engineering Conference, 2016, pp. 1–20.

[8] T. Hull, Project origami: activities for exploring mathematics, second edi Edition, CRC Press, 2012.

[9] E. D. Demaine, J. O. Rourke, Geometric Folding Algorithms: Linkages, Origami, Polyhedra, Cambridge University Press, Cambridge, 2007.

[10] S. A. Zirbel, R. J. Lang, M. W. Thomson, D. A. Sigel, P. E. Walkemeyer, B. P. Trease, S. P. Magleby, L. L. Howell, Accommodating Thickness in Origami-Based Deployable Arrays, Journal of Mechanical Design 135 (11) (2013) 111005.

[11] K. Kuribayashi, K. Tsuchiya, Z. You, D. Tomus, M. Umemoto, T. Ito, M. Sasaki, Self-deployable origami stent grafts as a biomedical application of Ni-rich TiNi shape memory alloy foil, Materials Science and Engineering A 419 (1-2) (2006) 131–137.

[12] A. P. Thrall, C. P. Quaglia, Accordion shelters: A historical review of origami-like deployable shelters developed by the US military, Engineering Structures 59 (2014) 686–692.
URL http://dx.doi.org/10.1016/j.engstruct.2013.11.009

[13] F. J. Martínez-Martín, A. P. Thrall, Honeycomb core sandwich panels for origami-inspired deployable shelters: Multi-objective optimization for minimum weight and maximum energy efficiency, Engineering Structures 69 (2014) 158–167.

[14] T. Tachi, Rigid-Foldable Thick Origami, Origami 5: Fifth International Meeting of Origami Science Mathematics and Education (2011) 253–264.

[15] Q. Shi, M. T. Heitzmann, J. M. Gattas, Analysis of steel origami tube with nonlinear rotational hinge stiffness, in: C. Wang, M. Ho, S. Kitipornchai (Eds.), 25th Australasian Conference on Mechanics of Structures and Materials (ACMSM25), Brisbane, 2018, pp. 1–7.

[16] C. P. Nikhare, Bending and springback analysis on sheet metal material discontinuity, in: ASME 2019 14th International Manufacturing Science and Engineering Conference, MSEC 2019, Vol. 2, 2019, pp. 1–7.

[17] Q. Shi, M. T. Heitzmann, J. M. Gattas, Nonlinear rotational stiffness and clash prevention in perforated steel fold lines, Engineering Structures 209 (2020) 110218.

[18] P. Venhovens, K. Bell, P. Marathe, A. Patkar, F. Lamance, D. Lind, C. D. Amico, Application of a novel metal folding technology for automotive BiW design, SAE Int. J. Passeng. Cars - Mech. Syst. 6 (2) (2013) 584–600.

[19] B. Gitlin, A. Kveton, J. Lalvani, Method of Bending Sheet Metal to Form Three-Dimensional Structures (2002).

[20] Max W.Durney, A. D. Pendley, Precision-folded, high strength, fatigue-resistant structures and sheet therefor (2013).

[21] European Aluminium Association, The Aluminum Automotive Manual_body-structures, Tech. rep., European Aluminum Association (2013).
URL http://www.alueurope.eu/wp-content/uploads/2011/12/1{_}AAM{_}Body-structures.pdf

[22] V. Boljanovic, Sheet metal forming processes and die design, Industrial Press, 2004.

[23] D. Zhang, Z. Cui, X. Ruan, Y. Li, An analytical model for predicting springback and side wall curl of sheet after U-bending, Computational Materials Science 38 (4) (2007) 707–715.

[24] E. C. Ã, T. Eisenhour, E. Corona, T. Eisenhour, E. C. Ã, T. Eisenhour, Wiping die bending of laminated steel, International Journal of Mechanical Sciences 49 (3) (2007) 392–403.
URL http://www.sciencedirect.com/science/article/pii/S0020740306001925

[25] Y. M. Huang, D. K. Leu, Effects of process variables on V-die bending process of steel sheet, International Journal of Mechanical Sciences 40 (7) (1998) 631–650.

[26] L. J. de Vin, A. H. Streppel, U. P. Singh, H. J. J. Kals, A process model for air bending, J. Mater. Process. Technol. 57 (1–2) (1996) 48–54.
URL http://www.sciencedirect.com/science/article/pii/0924013695020438

[27] Z. Fu, X. Tian, W. Chen, B. Hu, X. Yao, Analytical modeling and numerical simulation for three-roll bending forming of sheet metal, The International Journal of Advanced Manufacturing Technology 69 (5-8) (2013) 1639–1647.
URL http://link.springer.com/10.1007/s00170-013-5135-2

[28] V. Paunoiu, M. A. Saadatou, D. Nedelcu, M. Octavian, Experimental and numerical investigations of sheet metal circular bending, Indian Journal of Engineering and Materials Sciences 22 (5) (2015) 487–496.

[29] R. H. Wagoner, H. Lim, M. G. Lee, Advanced issues in springback, International Journal of Plasticity 45 (2013) 3–20.
URL http://dx.doi.org/10.1016/j.ijplas.2012.08.006

[30] W. Phanitwong, S. Thipprakmas, Development of anew spring-back factor for a wiping die bending process, JMADE 89 (2016) 749–758.
URL http://dx.doi.org/10.1016/j.matdes.2015.10.031

[31] D. Banabic, Sheet metal forming processes: constitutive modelling and numerical simulation, Springer Science & Business Media, 2010.

[32] A. Mkaddem, A. Potiron, Fold zone analysis in wiping die bending process by using experimental and numerical approaches, International Journal for Numerical Methods in Engineering 61 (December 2003) (2004) 303–315.

[33] R. Lingbeek, J. Huétink, S. Ohnimus, M. Petzoldt, J. Weiher, The development of a finite elements based springback compensation tool for sheet metal products, Journal of Materials Processing Technology 169 (1) (2005) 115–125.
URL http://linkinghub.elsevier.com/retrieve/pii/S0924013605004486

[34] E. Massoni, M. Bellet, J. L. Chenot, J. M. Detraux, C. De Baynast, A finite element modelling for deep drawing of thin sheet in automotive industry, Springer-Verlag, (1987) 719–725.

[35] M. A. Ablat, A. Qattawi, Numerical simulation of sheet metal forming: a review, International Journal of Advanced Manufacturing Technology 89 (1-4) (2017) 1235–1250.
URL http://dx.doi.org/10.1007/s00170-016-9103-5

[36] R. Bahloul, P. D. Santo, A. Potiron, Optimisation of the bending process of High Strength Low Alloy sheet metal: Numerical and experimental approach, International Journal of Material Forming 1 (SUPPL. 1) (2008) 113–116.

[37] J. Paralikas, K. Salonitis, G. Chryssolouris, Robust optimization of the energy efficiency of the cold roll forming process, International Journal of Advanced Manufacturing Technology 69 (1-4) (2013) 461–481.

[38] K. Lange, Handbook of Metal Forming, McGraw-Hill Book Company, 1985.
URL http://www.sme.org/ProductDetail.aspx?id=45822

[39] C. C. Kuo, M. R. Li, A cost-effective method for rapid manufacturing sheet metal forming dies, International Journal of Advanced Manufacturing Technology 85 (9-12) (2016) 2651–2656.
URL http://dx.doi.org/10.1007/s00170-015-8139-2

[40] C. S. Hoberman, Reversibly expandable three dimensional structure (1988).

[41] M. Trautz, A. Kunstler, Deployable folded plate structures - folding patterns based on 4-fold-mechanism using stiff plates, in: Proceedings of the International Association for Shell and Spatial Structures Symposium, Valencia, 2009, pp. 2306–2317.

[42] C. Hoberman, Folding structures made of thick hinged sheets (2010).

[43] Z. Abel, J. Cantarella, E. D. Demaine, D. Eppstein, T. C. Hull, J. S. Ku, R. J. Lang, T. Tachi, Rigid Origami Vertices: Conditions and Forcing Sets, J. Computational Geometry 7 (1) (2016) 171–184.

[44] Y. Chen, R. Peng, Z. You, Origami of thick panels, Science 349 (6246) (2015) 396–400.

[45] B. J. Edmondson, R. J. Lang, L. L. Howell, An Offset Panel Technique for Thick Rigidily Foldable Origami, in: ASME 2014 International Design Engineering Technical Conferences and Computers and Information in Engineering Conference, IDETC/CIE 2014, New York, 2014, pp. 1–8.

[46] Z. Xi, J.-m. Lien, Folding rigid origami with closure constraints, in: Proceedings of the ASME 2014 International Design Engineering Technical Conferences & Computers and Information in Engineering Conference IDETC/CIE 2014 August 17-20, 2014, Buffalo, New York, USA, 2016, pp. 2–11.

[47] R. J. Lang, K. Tolman, E. Crampton, S. P. Magleby, L. L. Howell, Accommodating Thickness in Origami-Inspired Engineered Systems, Applied Mechanics Reviews 70 (January) (2018) 1–20.

[48] E. B. Crampton, S. P. Magleby, L. L. Howell, Realizing Origami Mechanism From Metal Sheets, in: The ASME 2017 International Design Engineering Technical Conferences and Computers and Information in Engineering Conference IDETC/CIE 2017, Cleveland, USA, 2017, pp. 1–10.

[49] W. J. O'Donnell, B. F. Langer, Design of perforated plates, Journal of Engineering for Industry 84 (3) (1962) 307–319.
URL http://manufacturingscience.asmedigitalcollection.asme.org/article.aspx?articleid=1438262

[50] S. C. Baik, K. H. Oh, D. N. Lee, Forming limit diagram of perforated sheet, Scripta Metallurgica et Materiala 33 (8) (1995) 1201–1207.

[51] J. M. Davies, P. Leach, A. Taylor, J. Michael Davies, P. Leach, A. Taylor, The design of perforated cold-formed steel sections subject to axial load and bending, Thin-walled structures 29 (1-4) (1997) 141–157.
URL http://www.sciencedirect.com/science/article/pii/S0263823197000244

[52] Y. C. Wang, B. Salhab, Structural Behaviour and Design of Lightweight Structural Panels Using Perforated Cold-Formed Thin-Walled Sections under Compression, International Journal of Steel Structures 9 (1) (2009) 57–67.

[53] K.-d. Tsavdaridis, C. D. Mello, Vierendeel Bending Study of Perforated Steel Beams with Various Novel Web Opening Shapes , through Non-linear Finite Element Analyses ., Journal of Structural Engineering 138 (10) (2012) 1214–1230.
URL https://doi.org/10.1061/(ASCE)ST.1943-541X.0000562

[54] I. Boiko, Building constructions made of perforated metallic materials, in: 4th International Scientific Conference on Civil Engineering 13, Jelgava, LATVIA, 2013, pp. 53–59.

[55] S. K. C, P. M. V. Walame, Structural Analysis for Optimization of Stairs in off Road Agricultural Machinery, SSRG International Journal of Mechanical Engineering 3 (5) (2016) 35–38.

[56] M. A. Komur, Elasto-plastic buckling analysis for perforated steel plates subject to uniform compression, Mechanics Research Communications 38 (2) (2011) 117–122.
URL http://dx.doi.org/10.1016/j.mechrescom.2011.01.001

[57] J.-H. Woo, W.-B. Na, Effect of Cutout Orientation on Stress Concentration of Perforated Plates with Various Cutouts and Bluntness, International Journal of Ocean System Engineering 1 (2) (2011) 95–101.

[58] J. Rezaeepazhand, M. Jafari, Stress Analysis of Composite Plates with a Quasi-Square Cutout Subjected to Uniaxial Tension, Journal of Reinforced Plastics and Composites 29 (13) (2010) 2015–2026.
URL http://jrp.sagepub.com/cgi/doi/10.1177/0731684409341758

[59] A. Louhghalam, T. Igusa, C. Park, S. Choi, K. Kim, Analysis of stress concentrations in plates with rectangular openings by a combined conformal mapping - Finite element approach, International Journal of Solids and Structures 48 (13) (2011) 1991–2004.
URL http://dx.doi.org/10.1016/j.ijsolstr.2011.03.005

[60] S. S. Chakraborty, K. Maji, V. Racherla, A. K. Nath, Investigation on laser forming of stainless steel sheets under coupling mechanism, Optics & Laser Technology 71 (2015) 29–44.
URL http://linkinghub.elsevier.com/retrieve/pii/S0030399215000523

[61] O. R. Nandagopan, S. Ranjith Kumar, M. R. Rajesh, K. Manoharan, C. G. Nandakumar, Nonlinear behaviour of perforated plate with lining, Defence Science Journal 62 (4) (2012) 248–251.

[62] D. J. Bynum, M. M. Lemcoe, Birefringent-coating Analysis of Laterally Loaded Perforated Plates, Experimental Mechanics 3 (6) (1963) 140–147.

[63] M. M. Kumar, R. S, Y. H, Y. B. R, Study on Effect of Stress Concentration on Cutout Orientation of Plates with Various Cutouts and Bluntness, International Journal of Ocean System Engineering 3 (3) (2013) 295–1303.

[64] M. H. Saraçoğlu, U. Albayrak, Linear static analysis of perforated plates with round and staggered holes under their self-weights, Engineering Structure & Materials 2 (1) (2016) 39–47.

[65] L. A. Isoldi, M. V. De Real, J. Vaz, A. L. Correia, E. D. Dos Santos, L. A. Rocha, Numerical analysis of perforated thin plates subjected to tension or buckling, in: Proceedings - 2012 International Conference on Offshore and Marine Technology: Science and Innovation, NAVTEC 2012, 2012, pp. 46–49.

[66] H. Khatam, M. J. Pindera, Plastic deformation modes in perforated sheets and their relation to yield and limit surfaces, International Journal of Plasticity 27 (10) (2011) 1537–1559.
URL http://dx.doi.org/10.1016/j.ijplas.2010.10.004

[67] S. Jia, G. F. Raiser, G. L. Povirk, Modeling the effects of hole distribution in perforated aluminum sheets I: Representative unit cells, International Journal of Solids and Structures 39 (9) (2002) 2517–2532.

[68] Seung Chul Baik, Kyu Hwan Oh, Dong Nyung Lee, Analysis of the deformation of a perforated sheet under uniaxial tension, Journal of Materials Processing Technology 58 (2-3) (1996) 139–144.
URL http : / / www . sciencedirect . com / science / article / pii / 0924013695020969{% } 5Cnhttps : / / drive . google . com / open ? id = 0B{_} WiJDVReEdJRlRPRkdHSGFTb00{&}authuser=0

[69] E. Maiorana, C. Pellegrino, C. Modena, Elastic stability of plates with circular and rectangular holes subjected to axial compression and bending moment, Thin-Walled Structures 47 (3) (2009) 241–255.

[70] B. C. Patle, D. V. Bhope, Evaluation Of Stress Concentration Factors In Plate With Oblique Hole, IOSR Journal of Mechanical and Civil Engineering (IOSRJMCE) 2 (2) (2012) 28–32.

[71] C. D. Ajudia, R. Dangar, N. Jaykumar, D. K. D. Kothari, A review paper on forming process of a review paper on forming process of perforated sheet, International Journal of Education and Science Research Review 3 (3) (2016) 1–8.

[72] Y. Nakayama, A. Kodama, S. Nagaki, T. Abe, FEM analysis on elastic-plastic deformation of perforated sheets, Metals and Materials 4 (3) (1998) 319–321.
URL http://www.springerlink.com/index/T83Q1612V8KW57T6.pdf

[73] K. Elangovan, C. Sathiya Narayanan, R. Narayanasamy, Modelling of forming limit diagram of perforated commercial pure aluminium sheets using artificial neural network, Computational Materials Science 47 (4) (2010) 1072–1078.
URL http://dx.doi.org/10.1016/j.commatsci.2009.12.016

[74] K. Elangovan, C. S. Narayanan, R. Narayanasamy, Modelling the correlation between the geometrical features and the forming limit strains of perforated Al 8011 sheets using artificial neural network, International Journal of Material Forming 4 (4) (2011) 389–399.

[75] M. A. Farsi, B. Arezoo, Bending force and spring-back in v-die-bending of perforated sheet-metal components, Journal of the Brazilian Society of Mechanical Sciences and Engineering 33 (1) (2011) 45–51.
URL http://www.scielo.br/scielo.php?script=sci{_}arttext{&}pid=S1678-58782011000100007{&}lng=en{&}nrm=iso{&}tlng=en

[76] V. Nasrollahi, B. Arezoo, Prediction of springback in sheet metal components with holes on the bending area, using experiments, finite element and neural networks, Materials and Design 36 (2012) 331–336.
URL http://dx.doi.org/10.1016/j.matdes.2011.11.039

[77] N. Senthilnathan, G. Venkatachalam, N. N. Satonkar, A two stage finite element analysis of electromagnetic forming of perforated aluminium sheet metals, Procedia Engineering 97 (December) (2014) 1135–1144.
URL http://linkinghub.elsevier.com/retrieve/pii/S1877705814034602

[78] K. D. Kothari, R. Jhala, Investigation and Parametric Analysis of Steel Perforated Sheet Metal (PSM) for Optimum Forming Process, International Journal of Engineering Research in Africa 21 (2015) 118–123.
URL http://www.scientific.net/JERA.21.118

[79] G. Venkatachalam, V. Kumar, S. Narayanan, Finite element analysis of forming limits for stretch forming of perforated aluminium sheet metals, ARPN Journal of Engineering and Applied Sciences 8 (8) (2013) 652–655.

[80] R. Kazan, M. Firat, A. E. Tiryaki, Prediction of springback in wipe-bending process of sheet metal using neural network, Materials and Design 30 (2) (2009) 418–423.

[81] S. Salunkhe, S. Kumar, H. M. A. Hussein, AI Applications in Sheet Metal Forming, Springer, 2017.
URL http://link.springer.com/10.1007/978-981-10-2251-7

[82] A. S. Wifi, An incremental complete solution of the stretch-forming and deep-drawing of a circular blank using a hemispherical punch, International Journal of Mechanical Sciences 18 (c) (1976) 23–31.
URL http://www.sciencedirect.com/science/article/pii/0020740376900710

[83] M. Gotoh, F. Ishisé, A finite element analysis of rigid-plastic deformation of the flange in a deep-drawing process based on a fourth-degree yield function, International Journal of Mechanical Sciences 20 (7) (1978) 423–435.
URL http://linkinghub.elsevier.com/retrieve/pii/0020740378900322

[84] N. Wang, B. Budiansky, Analysis of sheet metal stamping by a finite-element method, J.Appl. Mech 45 (March 1978) (1978) 73–82.

[85] A. Makinouchi, Sheet metal forming simulation in industry, Journal of Materials Processing Technology 60 (1-4) (1996) 19–26.

[86] A. E. Tekkaya, State-of-the-art of simulation of sheet metal forming, Journal of Materials Processing Technology 103 (1) (2000) 14–22.

[87] M. L. Wenner, Overview - Simulation of sheet metal forming, AIP Conference Proceedings 778 A (August) (2005) 3–7.

[88] C. Kim, E. J. Pavlina, F. Barlat, Advances in sheet forming — materials modeling , numerical simulation , and press technologies, Journal of Manufacturing Science and Engineering 133 (December 2011) (2011) 1–12.

[89] P. Reddy, G. Reddy, P. Prasad, A review on finite element simulations in metal forming, International journal of Modern Engineering Research 2 (4) (2012) 2326–2330.
URL http://www.ijmer.com/papers/Vol2{_}Issue4/BX2423262330.pdf

[90] T. Kuwabara, Advanced material testing in support of accurate sheet metal forming simulations, AIP Conference Proceedings 1532 (2013) 69–80.

[91] A. Makinouchi, C. Teodosiu, T. Nakagawa, Advance in FEM simulation and its related technologies in sheet metal forming, CIRP Annals - Manufacturing Technology 47 (2) (1998) 641–649.

[92] E. Oniate, J. Rojek, C. Garino, NUMISTAMP : a research project for assessment of finite-element models for stamping processes, Journal of Materials Processing Tech. 50 (1995) 17–38.

[93] D. Yang, D. Jung, I. Song, D. Yoo, J. Lee, Comparative investigation into implicit, explicit, and iterative implicit/explicit schemes for the simulation of sheet-metal forming processes, Journal of Materials Processing Technology 50 (1-4) (1995) 39–53.
URL http://www.sciencedirect.com/science/article/pii/092401369401368B

[94] N. H. Kim, Introduction to nonlinear finite element analysis, Springer, 2015.

[95] K. Cheong, K. Omer, C. Butcher, R. George, J. Dykeman, Evaluation of the VDA 238-100 Tight Radius Bending Test using Digital Image Correlation Strain Measurement, Journal of Physics: Conference Series 896 (1) (2017) 0–8.

[96] W. H. Peters, W. F. Ranson, Digital Imaging Techniques In Experimental Stress Analysis, Optical Engineering 21 (3) (1982) 213427.

[97] B. Pan, Recent Progress in Digital Image Correlation, Experimental Mechanics 51 (7) (2011) 1223–1235.

[98] Y. L. Dong, B. Pan, A Review of Speckle Pattern Fabrication and Assessment for Digital Image Correlation, Experimental Mechanics 57 (8) (2017) 1161–1181.

[99] V. T. Nguyen, S. J. Kwon, O. H. Kwon, Y. S. Kim, Mechanical Properties Identification of Sheet Metals by 2D-Digital Image Correlation Method, Procedia Engineering 184 (Dic) (2017) 381–389.
URL http://dx.doi.org/10.1016/j.proeng.2017.04.108

[100] T. Brynk, B. R. Baishya, Residual stress estimation based on 3D DIC displacement filed measurement around drilled holes, Procedia Structural Integrity 13 (2018) 1267–1272.
URL https://doi.org/10.1016/j.prostr.2018.12.259

[101] J. Sullivan, A. Burnham, M. Wang, Energy-consumption and carbon-emission analysis of vehicle and component manufacturing., Tech. rep., Argonne National Laboratory, Argonne, IL USA (2010).
URL http://www.osti.gov/bridge/product.biblio.jsp?osti{_}id=993394

[102] R. WAGONER, M. LI, Simulation of springback: Through-thickness integration, International Journal of Plasticity 23 (3) (2007) 345–360.
URL http://linkinghub.elsevier.com/retrieve/pii/S0749641906001100

[103] A. Qattawi, A. Mayyas, M. A. Omar, An investigation of graph traversal algorithms in folded sheet metal parts design, The International Journal of Advanced Manufacturing Technology 69 (9-12) (2013) 2237–2246.
URL http://link.springer.com/10.1007/s00170-013-5181-9

[104] Z. Abel, R. Connelly, E. D. Demaine, M. L. Demaine, T. C. Hull, A. Lubiw, T. Tachi, Rigid Flattening of Polyhedra with Slits, in: Abstracts from the 6th International Meeting on Origami in Science, Mathematics and Education (OSME 2014), Tokyo, Japan, 2014, pp. 1–10.

[105] H. Lipson, M. Shpitalni, On the Topology of Sheet Metal Parts, Journal of Mechanical Design 120 (1998) 10–16.

[106] A. Qattawi, Optimizing Origami-Based Sheet Metal Parts Using Traversal Algorithms and Manufacturing Based Indices, in: Proceedings of the ASME 2016 International Manufacturing Science and Engineering Conference MSEC2016 June 27-July 1, 2016 Blacksburg, USA, Blacksburg, 2016, pp. 1–7.

[107] Z. Li, W. Chen, H. Hao, Q. Yang, R. Fang, Energy absorption of kirigami modified corrugated structure, Thin-Walled Structures 154 (February) (2020) 106829.
URL https://doi.org/10.1016/j.tws.2020.106829

[108] H. a. Akitaya, J. Mitani, Y. Kanamori, Y. Fukui, Generating folding sequences from crease patterns of flat-foldable origami, ACM SIGGRAPH 2013 Posters on - SIGGRAPH '13 (2013) 1.

[109] R. Lang, Origami Design Secrets: Mathematical Methods for an Ancient Art, Second Edition, Taylor & Francis, 2011.

[110] A. Qattawi, Extending origami technique to fold forming of sheet metal. PhD Dessertation, Ph.D. thesis, Clemson University (2012).

[111] M. Azimi, S. S. Mirjavadi, S. A. Asli, A. M. Hamouda, Fracture Analysis of a Special Cracked Lap Shear (CLS) Specimen with Utilization of Virtual Crack Closure Technique (VCCT) by Finite Element Methods, Journal of Failure Analysis and Prevention 17 (2) (2017) 304–314.

[112] M. Azimi, S. S. Mirjavadi, S. A. Asli, Investigation of Mesh Sensitivity Influence to Determine Crack Characteristic by Finite Element Methods, Journal of Failure Analysis and Prevention 16 (3) (2016) 506–512.

[113] H. Mirahmadi, M. Azimi, S. S. Mirjavadi, Calculation of stress intensity factor for functionally graded cylinders with two radial cracks using the weight function method, Theoretical and Applied Fracture Mechanics 85 (2016) 447–456.
URL http://dx.doi.org/10.1016/j.tafmec.2016.06.004

[114] H. Noori, R. Mahmudi, Prediction of forming limit diagrams in sheet metals using different yield criteria, Metallurgical and Materials Transactions A: Physical Metallurgy and Materials Science 38 A (9) (2007) 2040–2052.

[115] R. H. Wagoner, N. M. Wang, An experimental and analytical investigation of in-plane deformation of 2036-T4 aluminum sheet, International Journal of Mechanical Sciences 21 (5) (1979) 255–264.

[116] F. Pourboghrat, M. E. Karabin, R. C. Becker, K. Chung, Hybrid membrane/shell method for calculating springback of anisotropic sheet metals undergoing axisymmetric loading, International journal of plasticity 16 (6) (2000) 677–700.

[117] G. A. Nourollahi, M. Farahani, A. Babakhani, S. S. Mirjavadi, Compressive deformation behavior modeling of AZ31 magnesium alloy at elevated temperature considering the strain effect, Materials Research 16 (6) (2013) 1309–1314. URL http://www.scielo.br/scielo.php?script=sci{_}arttext{&}pid=S1516-14392013000600013{&}lng=en{&}tlng=en

[118] C. Wang, G. Kinzel, T. Altan, Mathematical modeling of plane-strain bending of sheet and plate, Journal of Materials Processing Tech. 39 (1993) 279–304.

[119] Z. T. Zhang, D. Lee, Development of a new model for plane strain bending and springback analysis, Journal of Materials Engineering and Performance 4 (3) (1995) 291–300.

[120] Z. Marciniak, J. Duncan, S. Hu, Mechanics of sheet metal forming, Mechanics of Sheet Metal Forming (2002) xiii–xx.
URL http://www.sciencedirect.com/science/article/pii/B9780750653008500030http://link.springer.com/10.1007/978-1-4613-2880-3

[121] U. P. Singh, S. K. Maiti, P. P. Date, K. Narasimhan, Numerical simulation of the influence of air bending tool geometry on product quality, Journal of Materials Processing Technology 145 (3) (2004) 269–275.

[122] R. Narayanasamy, P. Padmanabhan, Application of response surface methodology for predicting bend force during air bending process in interstitial free steel sheet, International Journal of Advanced Manufacturing Technology 44 (1-2) (2009) 38–48.

[123] V. Malikov, R. Ossenbrink, B. Viehmeger, V. Michailov, Experimental investigation and analytical calculation of the bending force for air bending of structured sheet metals, Advanced Materials Research 418-420 (2011) 1294–1300.

[124] R. Srinivasan, D. Vasudevan, P. Padmanabhan, Prediction of bend force and bend angle in air bending of electrogalvanized steel using response surface methodology, Journal of Mechanical Science and Technology 27 (7) (2013) 2093–2105.

[125] M. Chudasama, H. Raval, Development of analytical model of bending force during 3-roller conical bending process and its experimental verification, International Journal of Mechanical and Mechatronics Engineering 7 (11) (2013) 1292–1300.

[126] M. K. Chudasama, H. K. Raval, An approximate bending force prediction for 3-roller conical bending process, International Journal of Material Forming 6 (2) (2013) 303–314.

[127] M. K. Chudasama, H. K. Raval., Bending force prediction for dynamic roll-bending during 3-roller conical bending process, Journal of Manufacturing Processes 16 (2) (2014) 284–295.

[128] V. Vorkov, R. Aerens, D. Vandepitte, J. R. Duflou, Accurate prediction of large radius air bending using regression, Procedia Engineering 207 (2017) 1623–1628.
URL https://doi.org/10.1016/j.proeng.2017.10.1089

[129] V. Vorkov, R. Aerens, D. Vandepitte, J. R. Duflou, Analytical prediction of large radius bending by circular approximation, Journal of Manufacturing Science and Engineering 140 (12) (2018) 121010.

[130] V. Vorkov, R. Aerens, D. Vandepitte, J. R. Duflou, Experimental investigation of large radius air bending, International Journal of Advanced Manufacturing Technology 92 (9-12) (2017) 3553–3569.

[131] M. A. Ablat, A. Qattawi, Investigating the design and process parameters of folded perforated sheet metal, International Journal of Advanced Manufacturing Technology.

[132] W. D. Pilkey, D. F. Pilkey, R. E. Peterson, Peterson's stress concentration factors, 3rd Edition, John Wiley & Sons, Inc., Hoboken, NJ, 2008.
URL https : / / www . wiley . com / en - us / Peterson{% } 27s + Stress + Concentration+Factors{%}2C+3rd+Edition-p-9780470048245

[133] J. Kang, D. S. Wilkinson, P. D. Wu, M. Bruhis, M. Jain, J. D. Embury, R. K. Mishra, Constitutive Behavior of AA5754 Sheet Materials at Large Strains, Journal of Engineering Materials and Technology 130 (3) (2008) 031004.
URL http://materialstechnology.asmedigitalcollection.asme.org/article.aspx?articleid=1428218

[134] A. Codolini, Q. M. Li, A. Wilkinson, Mechanical characterization of thin injection-moulded polypropylene specimens under large in-plane shear deformations, Polymer Testing 69 (May) (2018) 485–489.

[135] L. C. Nunes, Modified slotted shear test for a thin sheet of solid polymer under large deformations, Polymer Testing 45 (2015) 20–30.
URL http://dx.doi.org/10.1016/j.polymertesting.2015.05.003

[136] Q. Yin, B. Zillmann, S. Suttner, G. Gerstein, M. Biasutti, A. E. Tekkaya, M. F. Wagner, M. Merklein, M. Schaper, T. Halle, A. Brosius, An experimental and numerical investigation of different shear test configurations for sheet metal characterization, International Journal of Solids and Structures 51 (5) (2014) 1066–1074.
URL http://dx.doi.org/10.1016/j.ijsolstr.2013.12.006

[137] J. Peirs, P. Verleysen, J. Degrieck, Novel Technique for Static and Dynamic Shear Testing of Ti6Al4V Sheet, Experimental Mechanics 52 (7) (2012) 729–741.

[138] A. R. Torabi, M. Alaei, Mixed-mode ductile failure analysis of V-notched Al 7075-T6 thin sheets, Engineering Fracture Mechanics 150 (2015) 70–95.
URL http://dx.doi.org/10.1016/j.engfracmech.2015.10.037

[139] ASTM International, ASTM E8/E8M-13 Standard Test Methods for Tension Testing of Metallic Materials (2009).
URL http://www.astm.org/Standards/E8.htm

[140] M. W. Durney, Precision-folded, high strength, fatigue-resistant structures and sheet therefor (2006).

[141] A.-a. Rivets, C.-h. Wire, M. Systems, Standard Test Method for Shear Testing of Thin Aluminum Alloy Products, Vol. 64, ASTM International, West Conshohocken, PA, 1964.

[142] W. Tong, Formulation of Lucas-Kanade digital image correlation algorithms for non-contact deformation measurements: A review, Strain 49 (4) (2013) 313–334.

[143] K. Wang, J. E. Carsley, B. He, J. Li, L. Zhang, Measuring forming limit strains with digital image correlation analysis, Journal of Materials Processing Technology 214 (5) (2014) 1120–1130.
URL http://dx.doi.org/10.1016/j.jmatprotec.2014.01.001

[144] S. K. Paul, S. Roy, S. Sivaprasad, H. N. Bar, S. Tarafder, Identification of Post-necking Tensile Stress–Strain Behavior of Steel Sheet: An Experimental Investigation Using Digital Image Correlation Technique, Journal of Materials Engineering and Performance 27 (11) (2018) 5736–5743.
URL https://doi.org/10.1007/s11665-018-3701-3

[145] ASTM Standard B565, Standard Test Method for Shear Testing of Aluminum and Aluminum-Alloy Rivets and, ASTM Book of Standards 64 (Reapproved 2015) (2004) 1–3.

[146] T. Wierzbicki, Y. Bao, Y. W. Lee, Y. Bai, Calibration and evaluation of seven fracture models, International Journal of Mechanical Sciences 47 (4-5 SPEC. ISS.) (2005) 719–743.

[147] Q. Hu, F. Zhang, X. Li, J. Chen, Overview on the Prediction Models for Sheet Metal Forming Failure: Necking and Ductile Fracture, Acta Mechanica Solida Sinica 31 (3) (2018) 259–289.

[148] C. P. Nikhare, Bending and springback analysis on sheet metal material discontinuity, ASME 2019 14th International Manufacturing Science and Engineering Conference, MSEC 2019 2 (2019) 1–7.

[149] W. C. Emmens, Formability: A Review of Parameters and Processes that Control, Limit or Enhance the Formability of Sheet Metal, Vol. 7, Springer Heidelberg Dordrecht London New York, 2011.

[150] S. P. Keeler, Circular grid system—a valuable aid for evaluating sheet metal formability, SAE Transactions 77 (1968) 371–379.

[151] G. M. Goodwin, Application of strain analysis to sheet metal forming problems in the press shop, SAE Transactions 77 (1968) 380–387.

[152] J. He, Z. Cedric Xia, D. Zeng, S. Li, Forming Limits of a Sheet Metal After Continuous-Bending-Under-Tension Loading, Journal of Engineering Materials and Technology 135 (3) (2013) 031009.

[153] K. Isik, M. B. Silva, A. E. Tekkaya, P. A. Martins, Formability limits by fracture in sheet metal forming, Journal of Materials Processing Technology 214 (8) (2014) 1557–1565.
URL http://dx.doi.org/10.1016/j.jmatprotec.2014.02.026

[154] J. Embury, J. Duncan, Formability maps, Annual Review of Materials Science 11 (1) (1981) 505–521.

[155] J. Jeswiet, F. Micari, G. Hirt, A. Bramley, J. Duflou, J. Allwood, Asymmetric Single Point Incremental Forming of Sheet Metal, CIRP Annals - Manufacturing Technology 54 (2) (2005) 88–114.
URL http://www.sciencedirect.com/science/article/pii/S0007850607600213

[156] A. Mishra, S. Thuillier, Investigation of the rupture in tension and bending of DP980 steel sheet, International Journal of Mechanical Sciences 84 (2014) 171–181.
URL http://dx.doi.org/10.1016/j.ijmecsci.2014.04.023

[157] S. A. Dizaji, H. Darendeliler, B. Kaftanoğlu, On the fracture prediction of 304L stainless steel sheets utilizing different hardening models, Journal of Physics: Conference Series 734 (3).

[158] A. M. Freudenthal, The inelastic behavior of engineering materials and structures, Wiley, 1950.

[159] M. G. Cockcroft, D. J. Latham, Ductility and the Workability of Metals (1968).

[160] P. B. Rozzo, B. Deluca, R. Rendina, A new method for the prediction of formability limits in metal sheets, Sheet Metal Forming and Formability, in: Proceedings of the 7th biennial Conference of the International Deep Drawing Research group, 1972.

[161] A. M, Central bursting in extrusion of inhomogeneous materials, in: Proceedings of 2nd International Conference on Technology for Plasticity,, Stuttgart, Germany, 1987.

[162] J. Rice, D. Tracey, On the ductile enlargement of voids in triaxial stress fields, Journal of the Mechanics and Physics of Solids 17 (3) (1969) 201–217.
URL http://linkinghub.elsevier.com/retrieve/pii/0022509669900337

[163] Y. Ling, Uniaxial True Stress-Strain after Necking, AMP Journal of Technology 5 (1) (2004) 37–48.